Study of Radiation Absorbance in Composite having Doped Hexaferrite and Barium Titanate Embedded in Conducting Polymer

Thesis submitted to the

LOVELY PROFESSIONAL UNIVERSITY

For the Award of degree of

DOCTOR OF PHILOSOPHY

IN PHYSICS

BY:

Talwinder Kaur

GUIDE:

Dr. A. K. Srivastava

SCHOOL OF PHYSICAL SCIENCES

LOVELY PROFESSIONAL UNIVERSITY, PHAGWARA

PUNJAB, INDIA-144411

May, 2016

DECLARATION

I declare that the thesis entitled "**Study of Radiation Absorbance in Composite having Doped Hexaferrite and Barium Titanate Embedded in Conducting Polymer"** has been prepared by me under the guidance of **Dr. A.K. Srivastava**, Associate Professor, Department of Physics, **Lovely Professional University.** No part of this thesis has formed the basis for the award of any degree or fellowship previously.

Talwinder Kaur

Department of Physics, School of Physical Sciences,

Lovely Professional University

Jalandhar-Delhi, G.T. Road (NH-1), Phagwara

Punjab (INDIA) -144411

Date:

CERTIFICATE

I certify that **Ms. Talwinder Kaur** has prepared her thesis entitled "**Study of Radiation Absorbance in Composite having Doped Hexaferrite and Barium Titanate Embedded in Conducting Polymer",** for the award of PhD degree in Physics of the **Lovely Professional University,** under my guidance. She has carried out the work at the Department of Physics, School of Physical Sciences, Lovely Professional University.

A. K. Srivastava

(Guide)

Department of Physics, School of Computer Science and Engineering

Lovely Professional University

Jalandhar-Delhi, G.T. Road (NH-1), Phagwara

Punjab (INDIA) -144411

Date:

ACKNOWLEDGEMENT

There are so many people to whom I would like to say thanks but first of all, I would like to say thanks to almighty God for giving me such opportunity. With immense pleasure, I wish to express sincere thanks and profound sense of gratitude to my PhD guide, **Dr. A. K. Srivastava**, for his guidance, support and inspiration during the course. His insight for sorting out problems leads to the progress of work. I am always grateful to him for providing me the research insights, inspiration and affectionate guidance, constructive criticism and calm endurance throughout the course.

I am thankful to Lovely Professional University for providing me the financial assistance. I extend my sincere thanks to faculty members of the Department of Physics for their guidance and encouragement during my research work. I am also thankful to Assistant Professor Sachin Kumar Godara, Department of Chemistry, Guru Nanak Dev University for his support. I express my deep sense of gratitude to Dr. Mahavir Singh, Dr. Jitender Kumar, Dr. Satinder Kumar Sharma, Dr. Pawan Kumar for their consistent support.

I would like to say thank to lab technicians for facilitation of work: Parminder Singh, Ramesh Kumar, Manoj Kumar, Harish Kumar, Varun Kumar, Sarbjit Singh, Harpinder Singh, and Parveen Kumar. I would like to thank Jyoti Sharma, Sarbjit Kaur, Bilal Hamid Bhat, Bashid, and Simran Singh for supporting me during this work.

I would like to express my deepest love to my parents and in-law family for supporting and keeping faith in me. Especially I would like to thank my husband to whom I am much indebted of his support during the course.

I would like to thank Cochin University of Science and Technology, Indian Institute of Technology Madras, IIT Mandi, University of Kashmir, Himachal Pradesh University, and IIT Guwahati for different characterization facilities. I appreciate their endeavour for providing me the results of testing in time.

Date: Talwinder Kaur

ABSTRACT

Conducting polymer nanocomposites have been in the focus of research mainly because of a number of attractive technological applications in the microwave region such as radar and radar absorbing materials, Wi-Fi systems and other communication systems, and microwave devices. They also have great potential for other applications such as rechargeable batteries. The extensive use of electrical equipment, producing microwave, has created a new problem named electromagnetic interference (EMI), which is not good for device health. So, an effective material is required to reduce the electromagnetic noise by using absorbing materials.

In the present research work, four different nanocomposites have been synthesized. The properties of barium hexaferrite which is an important component of the nanocomposites, have been optimized using annealing and substitution of rare earth elements like lanthanum, neodymium, and gadolinium and transition metal element cobalt. Followings compositions of barium hexaferrites have been prepared using sol gel auto combustion method:

- M-type barium hexaferrite $Ba_{0.7}La_{0.3}Fe_{11.7}Co_{0.3}O_{19}$, heat treated at 700 ˚C, 900 ˚C, 1100 ˚C and 1200 ˚C.
- M-type barium hexaferrite, $Ba_{1-x}La_xCo_xFe_{12-x}O_{19}$ (x = 0.0, 0.11, 0.21, 0.3, 0.41, 0.51, 0.61), heat treated at 900 °C.
- M-type barium hexaferrite with neodymium substitution, $Ba_{1-x}Nd_xCo_xFe_{12-x}O_{19}$ (x = 0.0 - 0.5), heat treated at 900 ˚C.
- M-type barium hexaferrite with Gd-Co substitution, $Ba_{1-x}Gd_xCo_xFe_{12-x}O_{19}$ ($0.0 \leq x \leq 0.6$), heat treated at 900 °C.

The various techniques like X-ray diffraction (XRD), Vector Network Analyser (VNA), Fourier Transform Infrared Spectroscopy (FT-IR), FT-Raman, UV-Vis-NIR spectrometer, I-V (Current-voltage) testing techniques, LCR meter, Vibrating Sample Magnetometer (VSM), Mossbauer spectroscopy, Thermo-gravimetric Analysis (TGA), SEM (Scanning electron microscopy), FE-SEM (Field Emission Scanning Electron Microscopy), TEM (Transmission Electron Microscope), AFM (Atomic Force Microscope), and PE loop tracer have been employed to investigate the structural, magnetic, dielectric, electrical, optical, multiferroic and surface morphological properties of these hexaferrites.

On the basis of the properties of different hexaferrites, the following nanocomposites have been synthesized and investigated:

- Nanocomposite of La-Co substituted barium hexaferrite, $Ba_{1-x}La_xCo_xFe_{12-x}O_{19}$ (x = 0.0, 0.1, 0.5, 0.6) and polyaniline
- Nanocomposite of Gd-Co substituted barium hexaferrite, $Ba_{1-x}Gd_xCo_xFe_{12-x}O_{19}$ (x=0.2, 0.5),barium titanate and polypyrrole
- Nanocomposite of Nd-Co substituted barium hexaferrite, $Ba_{1-y}Nd_yCo_yFe_{12-y}O_{19}$ (y=0.1, 0.25, 0.4) , barium titanate and polypyrrole
- Nanocomposites of $BaFe_{12}O_{19}$, $BaTiO_3$ and polypyrrole

Radiation loss study has been performed via Vector Network Analyzer (VNA). It is found that maximum loss occur at 17.9 GHz frequency (-23.10 dB, 99 % loss) in nanocomposite of La-Co substituted barium hexaferrite and polyaniline which is due to composition of conducting polymer and suitable magnetic material. A significant role of polyaniline has been observed in Electron Spin Resonance (ESR). Micro structural study reveals that prepared composite is in nano range. FT-IR spectra illustrate the presence of bonds relative to the expected phase like C-H bond in ring system at 1512 cm^{-1}.

The maximum radiation loss occur at 24.40 GHz (-14.66 dB) in nanocomposite of substituted barium hexaferrite, barium titanate and polypyrrole frequency owing to the composition of conducting polymer and suitable dielectric and magnetic material. Micro structural study reveals that prepared composite comprises of all the phases of present compound. Benzene ring absorption band (at 1183 cm^{-1}) in FT-IR spectra illustrate the presence of polymer in nanocomposite of substituted barium hexaferrite, barium titanate and polypyrrole.

PAPER PUBLISHED AND COMMUNICATED

1. **Talwinder Kaur**, Barjinder Kaur, Bilal H. Bhat, Sachin Kumar, A. K. Srivastava, Effect of calcination temperature on microstructure, dielectric, magnetic and optical properties of $Ba_{0.7}La_{0.3}Fe_{11.7}Co_{0.3}O_{19}$ hexaferrite, *Physica B* **456** (2015) 206-212 (DOI: 10.1016/j.physb.2014.09.003)
2. **Talwinder Kaur**, Sachin Kumar, Bilal Hamid Bhat, A. K. Srivastava, Effect on dielectric, magnetic, optical and structural properties of Nd-Co substituted barium hexaferrite nanoparticles, *Applied Physics A* 119 (4) (2015) 1531-1540 (DOI: 10.1007/s00339-015-9134-z)
3. **Talwinder Kaur**, Sachin Kumar, Jyoti Sharma, A. K. Srivastava, Radiation losses in microwave K_u band in magneto-electric nanocomposites. *Beilstein journal of Nanotechnology*, 6 (2015) 1700-1707 (DOI:10.3762/bjnano.6.173)
4. Sanjiw Kumar, **Talwinder Kaur**, Sachin Kumar, A. K. Srivastava, Effect of heat treatment on properties of $Sr_{0.7}Nd_{0.3}Co_{0.3}Fe_{11.7}O_{19}$, Journal of superconductivity and novel magnetism, 28 (2015) 2935-2940 (DOI: 10.1007/s10948-015-3105-7)
5. **Talwinder Kaur**, Bilal H Bhat, Sachin Kumar, A. K. Srivastava, Enhancement in physical properties of barium hexaferrite with substitution, *Journal of Materials Research*, 2015 (DOI: 10.1557/jmr.2015.244)
6. **Talwinder Kaur**, Bilal H Bhat, Sachin Kumar, A. K. Srivastava, Radiation losses in microwave region (K_u band = 12.4 – 18 GHz) by magneto-electric polypyrrole nano-composite, *Journal of Magnetism and Magnetic Material*, 2015 (Revised paper submitted).
7. **Talwinder Kaur**, Riti Sethi, Bilal H. Bhat, Sachin Kumar, A.K. Srivastava, Influence of La-Mg substitution and heat treatment on properties of Barium Hexaferrite, 2015 (To be communicated)
8. **Talwinder Kaur**, Sachin Kumar, Bilal H Bhat, A. K. Srivastava, Mossbauer, dielectric, optical, multiferroic and structural properties of substituted barium hexaferrite*, Advanced Material Letters* , 2015 (under revision)
9. Rajni Bala Pooni, **Talwinder Kaur** and A. K. Srivastava, High-Pressure Structural Phase Transition in Neptunium Compounds, Oriental Journal of Chemistry, 2015, 31 (3) (DOI: http://www.orientjchem.org/?p=10369)

Conference Proceedings

1. **Talwinder Kaur,** Noor Danish Ahrar Mundari and A. K. Srivastava, Structural properties of La-Mg Doped Barium Hexaferrites Nanoparticles, Journal of Engineering Science and Management. Vol-3, Page 79-81, **2013**, ISSN: 2250-3854.
2. **Talwinder Kaur** and A. K. Srivastava, Effect of pH on magnetic properties of doped barium hexaferrites, International Journal of research In Mechanical engineering & technology (IJRMET), Vol. 3, Issue-2 (May-Oct), Page 171-173, **2013**, ISSN : 2249-5762 (Online), ISSN : 2249-5770 (Print).
3. **Talwinder Kaur**, Jyoti Sharma, Rajneet Kaur, A.K. Srivastava, Structural and magnetic properties of Nickel nanoferrites, Elsevier Conference Proceedings on Exploring Basic & Applied Sciences for next Generation Frontiers Proceedings, Page-244-246, **2014**, ISBN: 978-93-5107-313-0
4. Jyoti Sharma, **Talwinder Kaur,** Rajneet Kaur, A.K. Srivastava, Structural and magnetic properties of Zinc nanoferrites, Elsevier Conference Proceedings on Exploring Basic & Applied Sciences for next Generation Frontiers, Page-258-260, **2014**, ISBN: 978-93-5107-313-0

Book Chapter

1. **Talwinder Kaur,** Barjinder Kaur and AK Srivastava, "Nanotechnology: Novel Prospective and prospects", Chapter 33, Page 224-228, 2014, McGraw Hill, USA.

Poster Presentation(s)

1. **Talwinder Kaur**, Barjinder Kaur and AK Srivastava, Effect of sintering temperature on magnetic properties of doped barium hexaferrite, International Conference on "Nanotechnology in the Service of Health, Environment and Society, NanoSciTech 2014, 13-15 Febraury 2014, Panjab University, Chandigarh, India.

Oral Presentaion(s)

1. **Talwinder Kaur**, Noor Danish Ahrar Mundari and A. K. Srivastava National conference on Recent Trends in Nanotechnology and its Applications (RTNA) March 23 2013 , Gulzar Group of Institutes, Khanna, Punjab.
2. **Talwinder Kaur** and A. K. Srivastava International Conference on Advances in Materials

and Manufacturing Technology, AMMT 2013, September 20-21, 2013, Chitkara University, Rajpura, Punjab.

3. **Talwinder Kaur**, Jyoti Sharma, Rajneet Kaur, A.K. Srivastava, Structural and magnetic properties of Nickel nanoferrites, Conference on Exploring Basic & Applied Sciences for next Generation Frontiers, November 14-15, 2014, Lovely Professional University, Phagwara, Punjab.

Workshop

1. TEQUIP sponsored Short Term Course on Advanced Materials and Characterization Techniques, Dr. B R Ambedkar Institute of Technology Jalandhar, June 01-07, 2015.

LIST OF SYMBOLS

Symbol	Description
β	Full width at half maxima
D	Crystallite size
D_x	X-ray density
D_b	Bulk density
P	Porosity
S	Surface area
σ_{AC}	AC conductivity
ω	Frequency
δ	Skin depth
α-Fe_2O_3	Hematite
T_C	Curie temperature
μ''	magnetic losses
ε''	dielectric losses
μ	Permeability
λ	X ray wavelength
θ	Bragg angle
ΔH	Line width
K	dielectric constant (In dielectric properties)
C	capacitance of the palette
d_{hkl}	d-spacing or interplanar between successive atomic planes (hkl)
η	Strain
H	Applied magnetic field
H_C	Coercivity
M_S	Saturation magnetization
K	Anisotropy constant
M_R	Remanent magnetization
SR	Squareness ratio
η_B	Magneton number

LIST OF ACRONYMS AND ABBREVIATIONS

$Ba_{1-y}Nd_yCo_yFe_{12-y}O_{19}/BaTiO_3$/Polypyrrole at y = 0.4	BNPY4
$Ba_{1-y}Nd_yCo_yFe_{12-y}O_{19}/BaTiO_3$/Polypyrrole at y = 0.25	BNPY25
$Ba_{1-y}Nd_yCo_yFe_{12-y}O_{19}/BaTiO_3$/Polypyrrole at y = 0.1	BNPY1
$Ba_{1-x}Gd_xCo_xFe_{12-x}O_{19}/BaTiO_3$/Polypyrrole at x = 0.5	BGPY5
$Ba_{1-x}Gd_xCo_xFe_{12-x}O_{19}/BaTiO_3$/Polypyrrole at x = 0.2	BGPY2
$BaFe_{12}O_{19}/BaTiO_3$/Polypyrrole	BBPY
$Ba_{1-x}La_xCo_xFe_{12-x}O_{19}$ /Polyaniline at x = 0.0	COP
$Ba_{1-x}La_xCo_xFe_{12-x}O_{19}$ /Polyaniline at x = 0.1	CL1P
$Ba_{1-x}La_xCo_xFe_{12-x}O_{19}$ /Polyaniline at x = 0.5	CL5P
$Ba_{1-x}La_xCo_xFe_{12-x}O_{19}$ /Polyaniline at x = 0.6	CL6P
$Ba_{1-x}La_xCo_xFe_{12-x}O_{19}$	BaLCM
$Ba_{1-x}Nd_xCo_xFe_{12-x}O_{19}$	BNCM
$Ba_{1-x}Gd_xCo_xFe_{12-x}O_{19}$	BGCM
$BaFe_{12}O_{19}$	BaM

LIST OF FIGURES

LIST OF TABLES

CONTENTS

CHAPTER-1

INTRODUCTION

1.1. INTRODUCTION

A huge development in the field of science and technology has affected the life of people in a positive and negative way. The extensive use of electronic circuits for communication, computation, automation, and other purposes makes it necessary for diverse circuits to operate in close proximity to each other. These circuits also affect each other adversely. Circuit designers are facing major challenges due to electromagnetic interference (EMI), and it is likely to become even more severe in the future. The use of integrated circuits and large scale integration has reduced the size of electronic equipment. As circuitry has become smaller and more sophisticated, more circuits are being crowded into less space, which increases the probability of interference. In addition, clock frequencies have increased dramatically over the years—in many cases to over a gigahertz. It is not uncommon today for personal computers used in the home to have clock speeds in excess of 1 GHz which may be affected due to electromagnetic interference. Radiation absorbers can also be used in aircraft to make it invisible from the enemy RADAR,

To provide a solution of radiation problems, the absorption of the electromagnetic field is required. The major advances in the field of nanotechnology are the development of composites in which the properties of two or more compounds have been utilized for radiation absorbance. The bad effects of electromagnetic (EM) radiation in the frequency range of 1–40 GHz has been a major concern for the society. Researchers, over a period of time, have been keenly interested in the sphere of polymer composites and many attempts have been made to synthesize such kind of composites which show improved EM absorption properties, saturation magnetization, anisotropy constants, conductivity and dielectric losses etc., for better use in applications. Efforts are being continuously made to produce materials and products that are superior, easy to use, and cost effective in nature and environment friendly. Hence, the EM wave absorbers with wide absorption bandwidth is the need of today. So, in this research, a plan has been employed to develop and investigate radiation absorbance of such kind of nanocomposites. The main components in the nanocomposites are substituted M-type barium hexaferrite, barium titanate, pyrrole and polyaniline.

1.2 FERRITE AND TYPES OF HEXAFERRITE

A ferrite is a member of a whole family of magnetic ceramic materials, including spinels, garnets, magnetoplumbites (hexaferrite), ortho-ferrites, or variation of these, such as γ -Fe_2O_3. It is also a member of the class of magnetic metallic oxides. Ferrites are solid solutions of metals containing ferric Fe^{3+} as the main element; furthermore, the name "Ferrite" deduces that iron oxide Fe_2O_3 is generally the common oxide to all ferrites. Ferrites are dark grey or black in appearance and fairly hard and brittle. Hexaferrites are the ceramic materials with iron (III) oxide (Fe_2O_3) as their principal component. Hexaferrite has 6 moles of hematite (Fe_2O_3) and has chemical formula $AO.6Fe_2O_3$ (where A = Ba or Sr). Hexaferrites have been categorized into following types (Table 1.1):

Table 1.1. Chemical composition of different hexagonal ferrites

Hexaferrites Type	Composition	Stacking order
S-spinel	$2MeO_2Fe_2O_3$	---
M	$BaO_6Fe_2O_3$	RSR*S*
W	$BaO_2MeO_8Fe_2O_3$	RSSR*S*S*
Y	$2BaO_2MeO_6Fe_2O_3$	TSTSTS
Z	$3BaO_2MeO_{12}Fe_2O_3$	RSTSR*S*T*S*
U	$4BaO_2MeO_{18}Fe_2O_3$	RSR*S*T*S*
X	$2BaO_2MeO_{14}Fe_2O_3$	RSR*S*S*

where Me = Fe, S = Fe_6O_8 (spinel), R = $BaFe_6O_{11}$ (hexagonal) and T = $Ba_2Fe_8O_{14}$ (hexagonal). The asterix(*) indicates that the corresponding sub unit is rotated 180˚ around the hexagonal axis.

1.3 STRUCTURE OF M-TYPE BARIUM HEXAFERRITE

Barium hexaferrite ($BaFe_{12}O_{19}$) has a mixed hexagonal and cubic close-packed structure (Fig. 1.1), with a barium atom substituting for an oxygen atom position, and iron atoms occupying interstices. It is one of the so-called hexagonal ferrites which have been extensively studied in recent years because of their high coercive force as compared with the well-known cubic ferrites.

The structure of barium ferrite can be derived from that of magnetite. It might be visualized as composed of four double layers of oxygen, plus two single layers, in which 1/4 of the oxygen are replaced by barium atoms. The latter two layers are interleaved between the first

and the second, and the third and fourth double layers, delineating the magnetite block (the second and the third). In hexagonal structure, two molecules of BaM having SRS*R* stacks. S* and R* are rotated sequences of S and R stacks. R and R* have hexagonal structure consists of having three oxygen ions in each of three layer, but in the center layer, one of the oxygen ion has been removed by the barium ion and the unit formula becomes $BaFe_6O_{11}$. The trigonal bipyramidal coordination of Fe^{3+}, present in R block, is a unique feature of the M phase which is not found in other hexagonal ferrites. S and S* have spinal structure with 2 oxygen layers having formula (Fe_6O_8). So, each layer contains three metal ions and four oxygen ions possessing two metal cation sites surrounded with six oxygen atoms (octahedral) and four oxygen anions (tetrahedral) in a block.

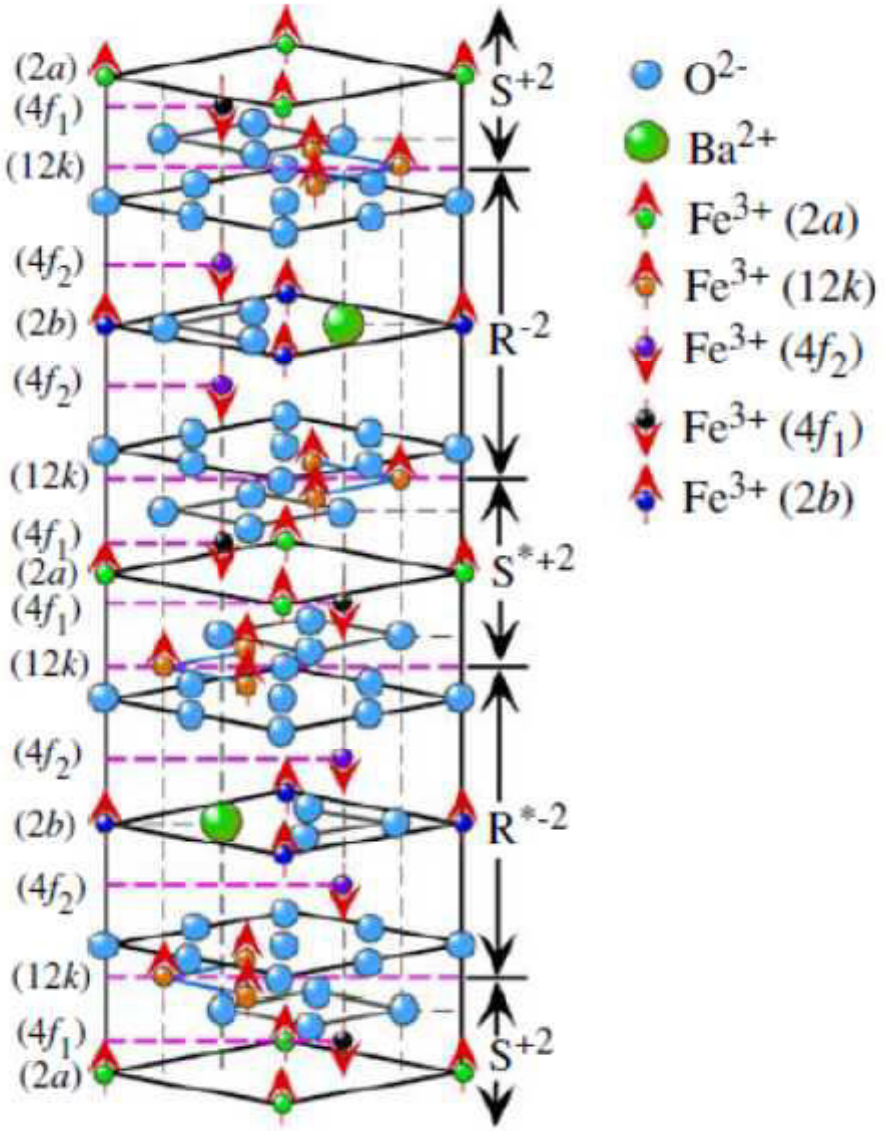

Fig.1.1. Spin arrangement in barium hexaferrite structure [1]

In total, there are 38 O^{2-} , 2 Ba^{2+} ions, 24 Fe^{3+} ions in a unit cell of hexagonal ferrite. Fe^{3+} ions are situated in trigonal bi-pyramidal site (2b), tetrahedral site ($4f_1$) and octahedral sites (12 k, 2a and $4f_2$). Due to presence of 24 Fe^{3+} ions, it shows good magnetic properties. There are 5 crystalline positions of Fe^{3+} ions in which three sites (2a, 2b and 12k) have spin up whereas two sites ($4f_1$ and $4f_2$) have spin antiparallel to crystallographic c axis [2, 3].
The iron atoms are in the octahedral and tetrahedral holes as in magnetites, except for one set of iron atoms which are coordinated to five oxygen. Thus the unit cell contains eighteen octahedral, two trigonal bipyramidal, and four tetrahedral iron atoms. Packing of the oxygen atoms in the middle two double layers is cubic, and in the plates above and below the magnetite block, starting from the barium-containing layers, it is hexagonal close packing.

M-type barium hexaferrites (BaM) having magneto-plumbite structure with space group P63/mmc exhibits high coercivity (6700 Oe) [4], high saturation magnetization (72 emu/g) [5], and high Curie temperature (T_C= 502˚C) [6]. This material has been widely investigated due to wide range of applications in electromagnetic wave absorber, microwave devices (mobile technology), perpendicular magnetic recording devices, magnetic hose (to transport magnetic field due to magnetic nature), super capacitors, self-biased and millimetre devices, sound devices and fridge magnets [7-12].

Substitution is a versatile tool for enhancement in the properties of a material. So an extensive study, carried out by several authors, can be found out in literature on basis of substitution of single element like Eu [13], Bi [14], Al [15], Ga [16], Pr, La [17], Er [18], La [19, 20], Ca[21] or different cationic combinations like Nd-Ni[22], Mg-Mn-Co-Ti [23], Co-Ti, La-Na [24], La-Co [25], Bi-Co-Ti [26], RE-Na [27], Ni-Zr [28]. Due to small ionic radii, rare earth metal and transition metal may replace the barium ions and ferric ions, respectively to enhance the magnetic properties and enhance the radiation absorbance. So many methods are available in literature to synthesize the hexaferrite like sol gel method [29], micro wave induction method [30], micro emulsion method [31], molten salt, citrate precursor method [32], sputtering and pulsed laser deposition [28].

1.4 STRUCTURE AND PROPERTIES OF BARIUM TITANATE

Barium titanate having formula $BaTiO_3$, white in colour, is the inorganic ceramic compound with excellent dielectric properties (100<dielectric constant<1200). Piezoelectric properties has been exhibited by barium titanate. This ferroelectric material also shows photorefractive effects. The structural properties of barium titanate are influenced by the heat

treatment. While going from high to low temperature, its phase changes from hexagonal to rhombohedrally crystal structure after attaining cubic, orthorhombic and tetragonal phase. Cubic phase is consisting of Ti-O-Ti edges with titanium ion at vertices with presence of barium ion at centre. Movements of barium ion to off-centre positions produces some interesting phenomena by enhancing crystal structure distortion. It has the perovskite structure (Fig. 1.2):

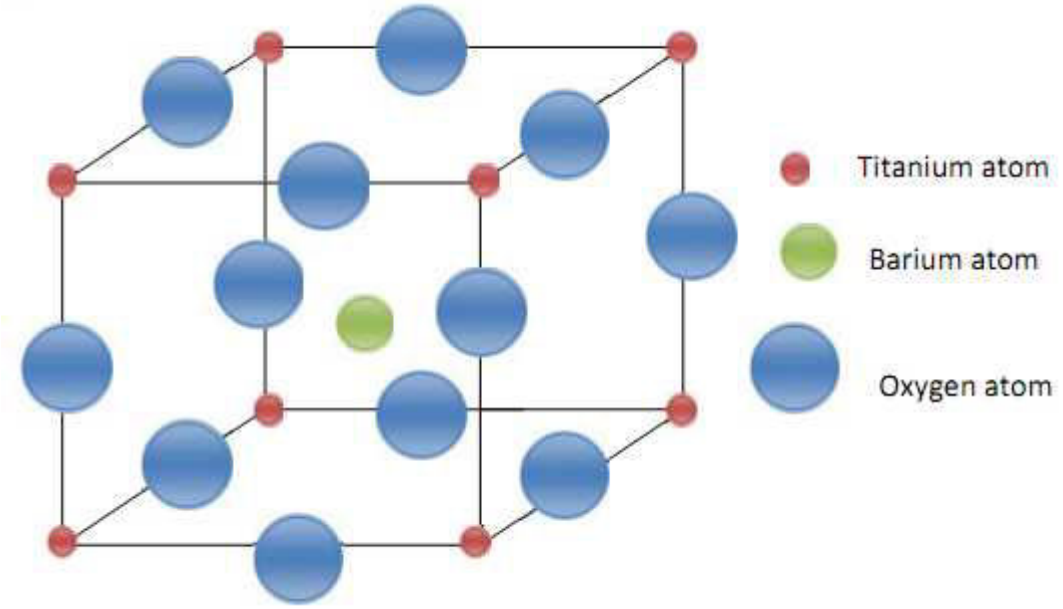

Fig: 1.2. Structure of Barium titanate ($BaTiO_3$)
[http://www.doitpoms.ac.uk/tlplib/ferroelectrics/barium_titanate.php]

1.5 POLYPYRROLE AND POLYANILINE

Since 1976, a number of conducting polymers, namely polypyrrole, polythiophene and polyaniline have become the focus of much study. MacDiarmid, Shirakawa and Heeger were awarded the 2000 Nobel Prize in Chemistry for the discovery and development of conducting polymers. This was particularly exciting because it created a new field of research on the boundary between chemistry and condensed matter physics. Since, these commonly known polymers are saturated and insulators so these were viewed as uninteresting from the point of view of electronic materials. Conducting polymers are polymers containing an extended p-conjugated system, made up of overlap of singly occupied p-orbitals in the backbone of the polymer chain. In conjugated polymers, bonds between the carbon atoms are alternating single and double (Fig 1.3 and 1.4). Every bond contains a localized sigma bond, which is responsible for holding the polymer together, in addition to less strongly localized p-bond which is weaker. These p-bonded unsaturated polymers have small ionization potentials and high electron

affinities which provides the ease of oxidation-reduction reactions. The electronic configuration of conjugated polymer is thus fundamentally different, where the chemical bonding leads to one unpaired electron (the p-electron) per carbon atom. Overlapping of p-orbitals of successive carbon atoms along the backbone leads to electron delocalization along the backbone of the polymer. This electronic delocalization provides the highway for charge mobility along the backbone of the polymer chain. Therefore, the electronic structure in conducting polymers is determined by the chain symmetry, i.e. the number and kind of atoms within the repeated unit. Such polymers can exhibit semiconducting or even metallic properties.

Intrinsically conducting polymers (ICPs) are inherently conducting in nature due to the presence of a conjugated p electron system in their structure. ICPs have a low energy optical transition, low ionization potential and a high electron affinity. The first discovered ICP was polyacetylene. Following the study on polyacetylene, other polymers such as polypyrrole (PPy), polythiophene, polyaniline, poly (p-phenylenevinylene), and poly (p-phenylene), as well as their derivatives, have been synthesized and reported as a new group of polymers known as ICPs. The conductivity of doped polyacetylene is comparable with that of metallic copper but its stability and processability are very poor compared to normal polymer. The conductivity of polyphenylene is quite high but its environmental stability is poor. Conversely, the conductivities of polypyrrole, polythiophene or polyaniline are comparatively less but these polymers have better stability and processability compared to those of polyacetylene and polyphenylene. Among all the conducting polymers, polyaniline (PANI) and polypyrrole (PPY) are best known for their ease of synthesis, environmental stability, ease of doping by protonic acids and highly tunable conducting polymer, which can be produced as bulk powder, cast films, or fibers. This, in conjunction with the feasibility of low-cost, large-scale production, makes it an ideal candidate for various applications. The overall conductivity of PANI/PPY depends on bridging among conductive regions. The electrically conducting polymers are capable of electrical charge transfer to the same extent as an electrical conductor or a semiconductor. Unlike other conjugated polymers, polyaniline and polypyrrole (PANI/PPY) have a good properties like free volume, solubility, electrical conductivity and optical activity. Undoped polyaniline has a conductivity of 6.28×10^{-9} S/m. These polymers are as noble as copper which is the basis for their broad use in printed circuit board manufacturing (as a final finish) and in corrosion protection. [33, 34, 35, 36]. Due to their fascinating electrical and optical properties, conducting polymers have played indispensable roles in specialized industrial applications in spite of their short history. However, the major aspects useful for most

applications are not the metal or semiconductor like electrical properties alone, but the combination of electrical conductivity and polymeric properties such as flexibility, low density and ease of structural modification that suffice for many commercial applications. PANI/PPY and the other conducting polymers such as polythiophene, are potential for applications due to their light weight, conductivity, mechanical flexibility and low cost [37]. Moreover these polymers have relaxation time corresponds to the Giga hertz frequency range. PANI/PPY are suitable for manufacture of electrically conducting yarns, antistatic coatings, electromagnetic shielding, and flexible electrodes. Attractive fields for current and potential utilization of PANI/PPY are in antistatic, charge dissipation or electrostatic dispersive (ESD) coatings and blends, electromagnetic interference shielding (EMI), anticorrosive coatings, hole injection layers, transparent conductors, indium tin oxide replacements, actuators, chemical vapor and solution based sensors, electrochromic coatings (for color change windows, mirrors etc.), toxic metal recovery, catalysis, fuel cells and active electronic components such as for non-volatile memory. Currently, the major applications are printed circuit board manufacturing (final finishes, used in millions of m² every year), antistatic and ESD coatings, and corrosion protection [38].

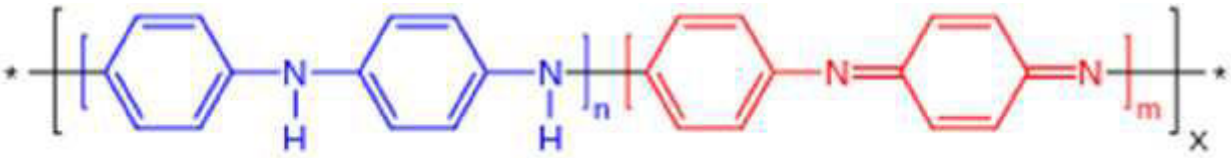

Fig 1.3: Structure of Polyaniline

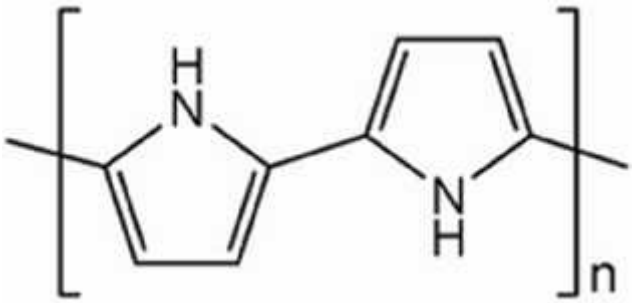

Fig 1.4: Structure of Polypyrrole

.

1.6 THEORY OF RADIATION ABSORBANCE

To block magnetic field in radiation absorbance material, a material having good magnetic properties is required. Rare earth substituted barium nano hexaferrite is better candidate for this

purpose. Further, at nano scale, properties of bulk hexaferrite are also enhanced. Properties of nano size ferromagnetic particles vary with size.

For radiation absorber, a conducting polymer is required for impedance matching and according to equation (1) for small skin depth (δ), a highly conducting material is needed, otherwise a thick sample is needed for higher absorbance. Absorption properties depends on permeability of magnetic material, permittivity of dielectric material and conductivity of conducting material. So, to block electric and magnetic field for better absorbance, a composite comprises of magnetic, dielectric and conducting material is needed. Here, contribution to absorption values would come due to magnetic losses (μ'') in barium hexaferrite and dielectric losses (ε'') in barium titanate and polymer. It can be seen from equation (2) that conductivity depends on imaginary part of complex permittivity (ε'') [39, 40].

$$\delta = \sqrt{2/\omega\mu\sigma_{AC}}$$

$$\delta = \sqrt{2/\omega\mu\sigma_{AC}} \qquad (1)$$

$$\sigma_{AC} = \omega\varepsilon_0\varepsilon'' \qquad (2)$$

$$SE(dB) = SE_A(dB) + SE_R(dB) \qquad (3)$$

Where σ_{AC} is the conductivity of the conducting polymer, δ is the skin depth and SE (dB) is the shielding effectiveness.

The shielding effectiveness i.e. the capability of a material to screen out electromagnetic radiation, is the resultant of absorption (SE_A) and reflection (SE_R) (equation 3). But in case of conducting polymer, shielding efficiency is mainly due to absorption (SE_A). SE_A depends on conductivity and permeability and is given by:

$$SE_A(dB) = 20\frac{d}{\delta}\log e \quad or \quad 20d\left(\sqrt{\frac{\omega\mu\sigma_{AC}}{2}}\right)\log e \qquad (4)$$

Where d is the sample thickness. So, the research on magnetic materials and dielectric material mixed with polypyrrole and polyaniline (conducting polymer) can be helpful to achieve effective absorbance bandwidth, high efficiency, small thickness, safe, durable, better performing, and low material manufacturing costs devices. The nano-hexaferrite material

(substituted barium hexaferrite) and barium titanate can be used with polypyrrole and polyaniline for radiation absorbance. The nano-sized hexaferrite has large magneto-crystalline anisotropy and coercivity which absorbs radiations at different frequencies (in 1-40 GHz) due to various interactive loss mechanisms, mainly related to magnetization and dielectric properties. A large magnetization is required for absorption. So, the doping of rare earth elements which have spin aligned as other iron atoms may increase the magnetization and coercivity.

Lanthanum, neodymium and gadolinium along with transition metals like cobalt have been used as substituents in the barium hexaferrite in the present work. These elements have configuration related to iron and barium so these can replace them to enhance properties [20]. The properties of hard magnetic material (doped barium hexaferrite) embedded polymer (polypyrrole/polyaniline) depend on the process and the technique of synthesization and amount of nano-hexaferrite. This can be achieved by changing the concentration of dopants, pH of the mixture solution, sintering temperature, dielectric material and conducting polymers.

1.7 APPLICATIONS OF NANOCOMPOSITES

The possibility of preparing nanocomposites embedded with nanoparticles has opened a new and exciting research field, with revolutionary applications not only in the electronic technology but also in the field of biotechnology. Main applications where polymer embedded composite used are:

(i) RAM (Radiation absorbing material) and microwave/EM wave absorption: The constantly increasing use of devices operating at MW (microwave) frequencies in our immediate environment such as radar, wireless and mobile communications has resulted in a great increase in EM interference. This has led to a growing requirement for EM absorbing materials to reduce interference, shield equipment, shield rooms and chambers for EM compatibility (EMC) testing, and to minimize the harmful effects of EM waves on biological tissues.

(ii) Magnetoelectric (ME) and multiferroic (MF) applications: Composite materials made of phases with excellent electrical (ferroelectric) and magnetic (ferro-/ferrimagnetic) properties can exhibit much stronger ME interactions, and show great promise.

(iii) Electrical and microwave devices: In world, there is constantly an increasing demand for signal processing devices in mobile communications, radar detection and instrumentation, satellites and *global positioning system* (GPS), wireless communications, security and defence,

aerospace, automotive and anti-collision applications. Furthermore, the operating frequencies are always moving progressively higher, from MW to millimetre wave, requiring the use of ferrites composites.

1.8 OBJECTIVES OF THE PRESENT WORK

The objective of present work is to synthesize nanocomposites for radiation absorbance. At first substituted (La, Nd, Gd, Co) barium hexaferrite has been synthesized and investigated for their structural, magnetic, dielectric, electric properties. Then, in second step $BaTiO_3$ has been synthesized and analysis performed for phase and present impurities. The last step will be to synthesize nanocomposites containing substituted hexaferrite, barium titanate and conducting polymer (polypyrole and polyaniline) and investigate their radiation absorbance properties in 1-40 GHz.

Although, a lot of research work were performed by researchers on electromagnetic properties of composites [39, 40, 41, 42] but because of small absorption bandwidth [39, 40, 43, 44], low reflection loss (1-5 dB) and ineffective high temperature performance, research has been set on emerging trends in this field. To achieve the desired properties, research will be focused on addition on new substituents in hexaferrite materials and then incorporated in polymer for electromagnetic absorber.

The efforts will be made to develop composite of hexaferrite having high anisotropy (> 50 emu/g) and coercivity (> 5 kOe) and barium titanate embedded in polypyrrole/ polyaniline (conducting polymer) in nano-range for effective electromagnetic radiation absorbance. Effort will also be made to develop such a composite which has high dielectric loss (> 10 dB) and wide absorption bandwidth required for excellent radiation absorbance. So, a composite with desired properties is the need of today. By selecting suitable magnetic material and polymer, the problem of inefficiency of absorbance can be tackled.

CHAPTER-3

METHOD OF SYNTHESIS

An important point about the properties of nanohexaferrites is that their properties depend on the grain size and phase purity which are extensively affected by the synthesis techniques. Various routes can be found in literature to synthesize hexaferrite and barium titanate which include salt-melt technique, the ceramic sintering process mainly carried above 1200 ˚C, sol-gel technique, mechanical grinding, microemulsion technique, hydrothermal reaction, glass crystallization technique, microwave-plasma technique and many more. Among so many methods, an ideal synthesis route must outcome a homogeneous, fine granular material. Classical ceramic as well as ball milling method are used for technical and commercial applications, produces inhomogeneous particles at microscopic level. Whereas glass crystallization left impurities and even, this process is time consuming. Very high temperature routes results in aggregation of particles and loss of volatile components. Substituted barium hexaferrite (BaM) has been synthesized via sol gel route in the present work.

Among the various methods, a modified Pechini sol gel method [45] meets the requirement for the preparation of nano grained hexaferrites. Advantages of this method include: less time consuming, highly efficient with high productive rate and low processing cost. In addition to the mentioned advantages, sol gel technique additionally gain the advantages for ultrafine resultant particles and can provide a multi component oxide having fine grain with homogenous composition as the amount of reactants can be facilely controlled.

So, for the synthesis of barium hexaferrite, sol–gel combustion technique is utilized. This is an innovative way with a peculiar mixing of the initial chemical in solution form and then gelation of solution and the subsequent combustion process of an aqueous solution containing preferred metal nitrate salts with organic fuel, resulting in less dense product with immensely colossal surface area. In the present study, a metal nitrates and citric acid solution have been used to prepare barium hexaferrite as a magnetic material. The effect of amount of dopants and temperature on the hexaferrite have been studied at initial stage. Comparison study has also been conducted between strontium and barium hexaferrite. After analysing the results, the composites having suitable pH value, amount of dopants at effective temperature have been prepared.

3.1. STEPS OF SYNTHESIZATIONS

Nanosized $Ba_{1-x}RE_xFe_{12-x}Co_xO_{19}$ (x= 0.0-0.61, RE = La, Gd, Nd) samples are synthesized using modified Pechini sol gel method with different compositions to study the effect of rare earth and Co elements on the structural, magnetic and thermal properties of the as-prepared samples. Chemicals required for the synthesis of substituted barium hexaferrite are:

- Barium nitrate AR grade [$Ba(NO_3)_2$] : 261.37 g/mol
- Lanthanum Nitrate AR grade [$La(NO_3)_3 \cdot 6H_2O$] : 433.02 g/mol
- Gadolinium Nitate AR grade [$Gd(NO_3)_3 \cdot 6H_2O$] : 451.36 g/mol
- Neodymium nitrate AR grade [$Nd(NO_3)_3 . 6H_2O$] : 438.35 g/mol
- Ferric nitrate AR grade [$Fe(NO_3)_3.9H_2O$] : 404 g/mol
- Cobalt Nitrate AR grade [$Co(NO_3)_2 \cdot 6H_2O$] : 291.03 g/mol
- Citric acid anhydrous [$C_6H_8O_7$] : 192.13 g/mol
- Aqueous ammonia AR grade [NH_4OH] to control the pH of the initial solution at 6.8

3.2 SYNTHESIS OF SUBSTITUTED BARIUM HEXAFERRITE ($Ba_{1-x}RE_xFe_{12-x}Co_xO_{19}$, RE=La, Nd and Gd)

Following steps are involved in the synthesis of substituted barium hexaferrite:

- Aqueous solutions of metal nitrates are prepared in stiochiometric amounts according to molar ratio separately by dissolving the metal salts in distilled water.
- Aqueous solution of citric acid added to the salt solution with cation to citric acid in a specific molar ratio (metal: citric acid- 1:1.5).
- Aqueous ammonia is added to the solution to adjust the pH of the solution at 6.8.
- The solution is then heated at 80 ˚C with continuous stirring for about 7-8 h with a help of a magnetic stirrer until a viscous gel is formed.
- The viscous gel is dried over a hot plate at 300 ˚C to form the precursor material for 2-3 h.
- The precursor get pre-sintered in a muffle furnace at 500 ˚C for 2 hours.
- The same procedure has been repeated to obtain samples with different compositions i.e. for different values of x and y (x = 0.1 - 0.61).
- The precursor material prepared for different x has been sintered at 900 ˚C in a muffle furnace (as illustrated in Fig 3.1)

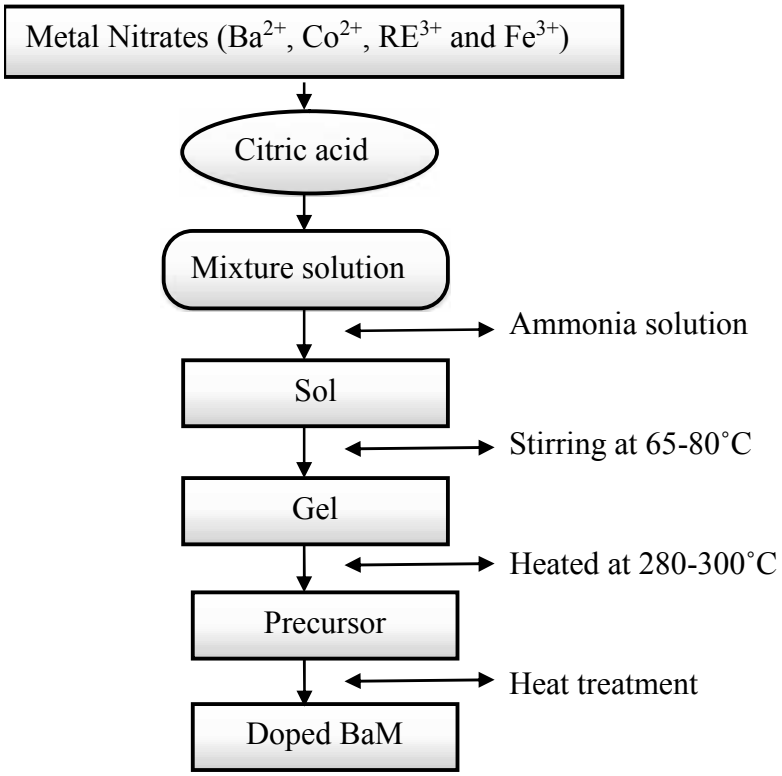

Fig 3.1: Flow Chart for the synthesis of $Ba_{1-x}RE_xCo_xFe_{12-x}O_{19}$ (x = 0-0.61) powders

3.3 SYNTHESIS OF BARIUM TITANATE

The starting materials used for the synthesis of barium titanate are: barium nitrate, TiO_2 and oxalic acid (oxalate process). An aqueous solution of barium nitrate (0.12 M) was taken using distilled water. Required amount (Ba/Ti = 1:1) of TiO_2 powder was poured to the aqueous solution of barium nitrate with constant stirring. To avoid the agglomeration of titanium oxide particle, the mixture is ultrasonicated for 10 minutes. Oxalic acid (0.4 M) was added to the mixture drop wise with vigorous stirring. Ammonia solution is added to maintain the pH at 6.8. Then, precipitates are formed and which has been washed repeatedly with distilled water, followed by drying at 40 ˚C for 2 days. The precursor was calcined at 900 ˚C.

3.4 EMULSION POLYMERIZATION FOR SYNTHESIS OF COMPOSITES

Following steps are involved in the synthesis of composites:

- Doped barium hexaferrite and barium titanate in ratio 1:1 has been grinded for 3 hours.
- The resulting barium hexaferrite and barium titanate get homogenized with emulsion solution formed with 0.3 M dodecyl benzene sulphonic acid (DBSA).

- Then, monomer is added in 0.1 M content to this solution and homogenized for 4-5 hours to form micelle of monomer with barium hexaferrite. For polypyrrole composite, barium titanate and barium hexaferrite and pyrrole monomer were added and ultrasonicate for 30 minutes before and after adding monomer.
- To polymerize the prepared solution via emulsion polymerization, oxidant is used. Ammonium persulphate ($(NH_4)_2S_2O_8$-0.1M) has been used as an oxidant at 0-2°C (as shown in Fig 3.2).
- Demulsification procedure has been carried out with isopropyl alcohol. Further, for washing, ethyl alcohol is used and the resultant precipitates are dried in oven at 65 ˚C for 48 h.

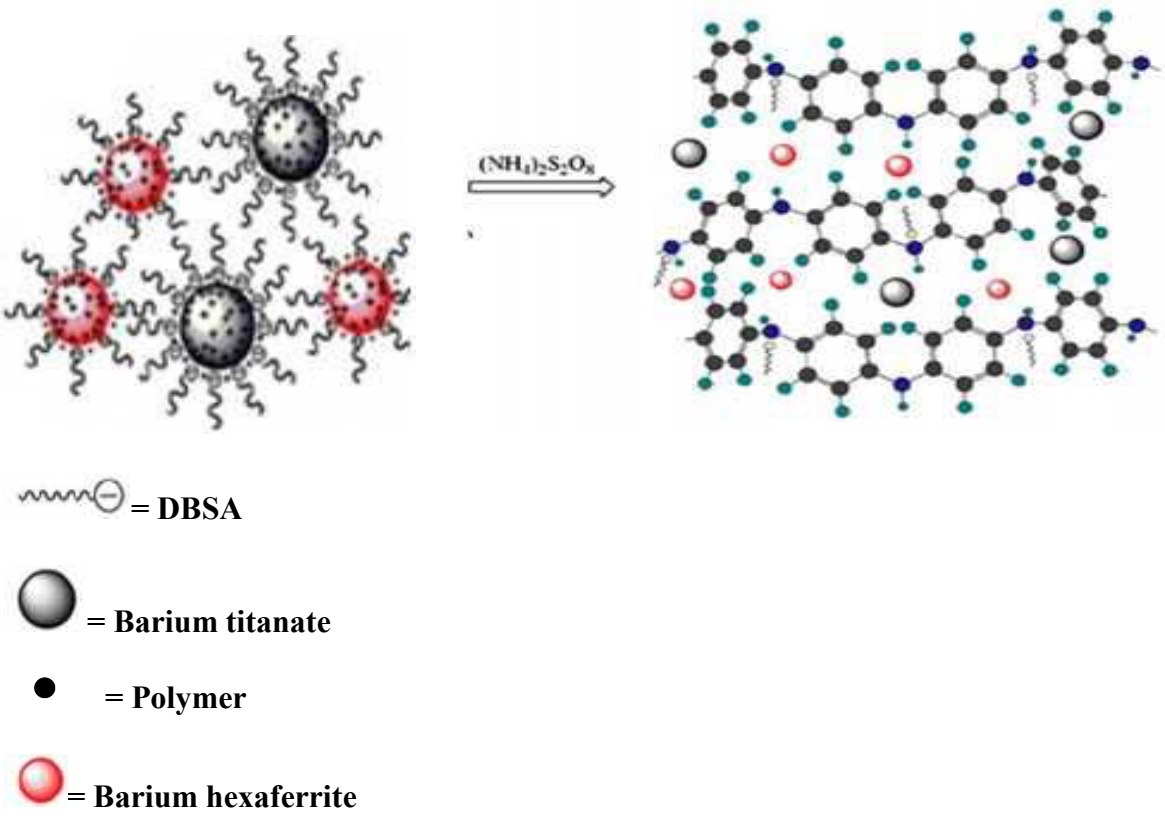

Fig. 3.2: Polymerization of DBSA solution containing doped hexaferrite and barium titanate [Anil Ohlan et al.]

CHAPTER-4

CHARACTERIZATION TECHNIQUES

Following characterization methods have been used to investigate the properties of prepared samples.

4.1 **X-Ray Diffraction**

X-ray diffraction methods are the most effective methods for determining the crystal structure of materials. Diffraction methods can identify chemical compounds from their crystalline structure, not from their compositions of chemical elements. It means that the different compounds (or phases) that have the same composition can be identified.

4.2 **Electron Microscopes (SEM/FE-SEM/TEM)**

The scanning electron microscope (SEM) is the most widely used type of electron microscope. It examines microscopic structure by scanning the surface of materials similar to scanning confocal microscopes but with much higher resolution and much greater depth of field. A SEM image is formed by a focused electron beam that scans over the surface area of a specimen; it is not formed by instantaneous illumination of a whole field as for a TEM. Whereas in Field emission Scanning electron microscope (FESEM), the electrons are ejected by the field emission gun rather than thermally heated tubes (SEM). Perhaps the most important feature of an SEM is the three-dimensional appearance of its images because of its large depth of field. Transmission electron microscope is based on the beam of the electrons, transmitted through the samples. For TEM analysis, the sample preparation is a tough part. A very thin sample should be taken on the grid for analysis.

4.3 **Thermo-Gravimetric Analysis (TGA)**

Thermo-gravimetric analysis is the most widely used thermal method. It is based on the mass loss of a material as a function of temperature. In thermo gravimetric analysis, a continuous graph of mass change against temperature is obtained when a substance is heated at a uniform rate or at a constant temperature. A plot of mass change versus temperature (T) is known as thermogravimetric curve, better known as TG curve

The TG curve is generally plotted with the mass (m) decreasing downwards on the y-axis (ordinate) and the temperature (T) increasing towards the right on the x-axis (abscissa). TG curves help in revealing the extent of purity of analytical samples and in determining the mode of their transformations within specified range of temperature.

4.4 Differential Thermal Analysis (DTA) and Differential Scanning Calorimetry (DSC):

(a) Differential Thermal Analysis (DTA) and Differential Scanning Calorimetry (DSC) are the most widely used thermal analysis techniques. Both techniques have the same objectives: to examine thermal events in a sample by heating or cooling without mass exchange with its surroundings. The thermal events examined by DTA and DSC include solid phase transformation, glass transition, crystallization and melting. 'Differential' emphasizes that analysis is based on differences between sample material and a reference material in which the examined thermal events do not occur.

(b) Differential Scanning Calorimetry (DSC): A DSC instrument is designed to measure the heat flow difference between sample and reference. There are two widely used DSC systems: the *heat flux DSC* and the *power-compensated DSC*. The heat flux DSC is also called 'quantitative DTA' because it measures the temperature difference directly and then converts it to heat flow difference.

4.5 Vibrating Sample Magnetometer: A vibrating sample magnetometer (VSM) operates on Faraday's law of induction, which tells us that a changing magnetic field produces an electric field. This electric field can be measured and can tell us information about the changing magnetic field. A VSM is used to measure the magnetic behaviour of magnetic materials.

A VSM operates by first placing the sample to be studied in a constant magnetic field. If the sample is magnetic, this constant magnetic field magnetize the sample by aligning the magnetic domains, or the individual magnetic spins, with the field. The stronger the constant field, the larger the magnetization.

4.6 Fourier Transform Infrared Spectroscopy (FTIR): One of the most basic tasks in spectroscopy is to characterize the spectrum of a light source: how much light is emitted at each different wavelength. The most straightforward way to measure a spectrum is to pass the light through a monochromatic, an instrument that blocks all of the light *except* the light at a certain wavelength (the un-blocked wavelength is set by a knob on the monochromatic). Then, the intensity of this remaining (single-wavelength) light is measured. The measured intensity

directly indicates how much light is emitted at that wavelength. By varying the monochromator's wavelength setting, the full spectrum can be measured.

4.7 LCR meter: An LCR meter is a piece of electronic test equipment used to measure the inductance (L), capacitance (C), and resistance (R) of a component. Usually the device under test (DUT) is subjected to an ac voltage source. The meter measures the voltage across and the current through the DUT. From the ratio of these, the meter can determine the magnitude of the impedance. Effect of temperature can also been studied.

4.8 Vector Network Analyser: Network analysers are used at wide range of frequencies; operating frequencies can range from 5 Hz to 1.05 THz. A network analyser is an instrument that measures the network parameters of electrical networks. Today, network analyzers commonly measure S–parameters because reflection and transmission of electrical networks are easy to measure at high frequencies.

S-parameters extraction from VNA is a straightforward process. At first, connect the source to port 1 by terminating port 2 that allows the instrument to measure wave ratios b_1/a_1, b_2/a_1 and a_2/a_1 with respect to frequency. The same procedure is applicable for the second port i.e the VNA switches the source to the output by terminating the input port of the device under test (DUT) (equations 4.1 and 4.2). With these parameters, it is possible to calculate the S-parameters as a function of frequency. In VNA instrument the incident and reflected waves are separated by the directional couplers. Vector network analyzers normally uses heterodyne receivers to measure both the phase and magnitude of signals. The receiver removes the noises and unwanted tones in the signals that can be originated by the instrument. VNA instrument can measure the travelling waves at all ports of the network terminated with specific load impedance, typically 50 Ohms. A typical but simplified VNA architecture is illustrated in Figure 4.1 and can be decomposed into different elementary blocks. Every test port has signal processor hardware to split out the incident and reflected travelling waves. S parameters can be calculated from b_1 and b_2. Here b_1 and b_2 is given by

$$b_1 = S_{11}a_1 + S_{12}a_2 \qquad \text{..... (4.1 a)}$$

$$b_2 = S_{21}a_1 + S_{22}a_2 \qquad \text{..... (4.1 b)}$$

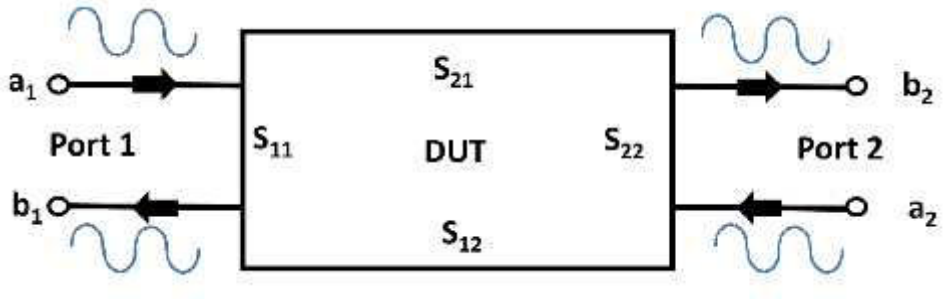

Figure 4.1: Shows a two-port device under test (DUT) along with the corresponding four S-parameters and the four waves.

$$S_{11} = \left.\frac{b_1}{a_1}\right|_{a_2=0} \qquad S_{12} = \left.\frac{b_1}{a_2}\right|_{a_1=0} \qquad \text{……..(4.2a)}$$

$$S_{21} = \left.\frac{b_2}{a_1}\right|_{a_2=0} \qquad S_{22} = \left.\frac{b_2}{a_2}\right|_{a_1=0} \qquad \text{…….(4.2b)}$$

4.9 UV-Vis-NIR- The incident electromagnetic radiations in UV-Vis-NIR spectrometer interacts with the molecules of the material. The absorbed molecule after gaining energy undergoes vibrational, rotational and translational motion. If energy is sufficiently high then molecule can get ionized. The excited molecules likely to come back at rest motion by releasing the energy and some energy get consumed in above said motions. This absorption and desorption energy value encloses the properties of the material and can be used for analysis purpose. The absorbed and emitted frequency and wavelength can be recorded at spectrum. Spectral analysis yields qualitative information about the material under study.

4.10 Electron Spin Resonance (ESR)- Material that contains an unpaired electron kept in a static magnetic field. The magnetic field interacts with the magnetic moment of electron and causes splitting of spin energy levels (Zeeman splitting). The neighbourhood also effects this interaction. The first derivative of the absorption has been plotted with magnetic field

4.11 Mossbauer Spectrometer: Nuclei in a solid crystal, however, are not free to recoil because they are bound in place in the crystal lattice. When a nucleus in a solid emits or absorbs

a gamma ray, some energy can still be lost as recoil energy, but in this case it always occurs in discrete packets called phonons (quantized vibrations of the crystal lattice). Any whole number of phonons can be emitted, including zero, which is known as a "recoil-free" event. In this case conservation of momentum is satisfied by the momentum of the crystal as a whole, so practically no energy is lost. Mössbauer found that a significant fraction of emission and absorption events will be recoil-free, which is quantified using the Lamb–Mössbauer factor. This fact is what makes Mössbauer spectroscopy possible, because it means gamma rays emitted by one nucleus can be resonantly absorbed by a sample containing nuclei of the same isotope, and this absorption can be measured with Mossbauer spectrometer.

4.12 PE loop tracer: Two metal plates are mounted on either side of the gap whose separation is to be measured. The plates act as a capacitor whose capacitance is inversely proportional to the gap between the plates according to the normal relationship. The probe plates are normally fitted with guard rings to eliminate errors from edge effects. If a constant alternating current is passed through the capacitance probe, then the amplitude of the voltage generated is proportional to the gap distance.

CHAPTER-7

EFFECT ON DIELECTRIC, MAGNETIC, OPTICAL AND STRUCTURAL PROPERTIES OF Nd-Co SUBSTITUTED BARIUM HEXAFERRITE NANOPARTICLES

Abstract

M-type barium hexaferrite [$Ba_{1-x}Nd_xCo_xFe_{12-x}O_{19}$ (x = 0.0 - 0.5) (BNCM)] powders, synthesized using citrate precursor method, were heat treated at 900 ˚C for 5 h. The pattern of powders, when subjected to X-ray diffraction (XRD), shows the formation of M-type hexaferrite phase. The formation of BNCM, from thermogravimetric analysis (TGA)/ differential thermal analysis (DTA)/ differential thermal gravimetry (DTG), is observed to be at 440 ˚C. The presence of two prominent peaks near 430 cm^{-1} and 580 cm^{-1} in Fourier Transform Infrared Spectroscopy (FT-IR) spectra indicate the formation of M-type hexaferrites. The M-H curves obtained from Vibrating Sample Magnetometer (VSM) were used to calculate saturation magnetization (M_S), retentivity (M_R), squareness ratio (SR) and coercivity (H_C). UV-Vis NIR spectroscopy reveals that band gap depends on size of the crystallites. The dielectric constant is found to be high at low frequency and decreases with increase in frequency. This kind of behaviour is explained on the basis of Koop's phenomenological theory and Maxwell Wagner theory.

7.1. Introduction

M-type hexaferrites ($BaFe_{12}O_{19}$, abbreviated as BaM), a hard magnetic material, is best known representative among the hexaferrite family and holds technological interest because of their magnetic, chemical, corrosion resistive and dielectric properties. On account of these properties, these materials can be used in super-capacitors, microwave devices (mobile technology), magnetic hose, perpendicular magnetic recording devices, self-biased and millimetre devices, electromagnetic wave absorber, sound devices and fridge magnets [7-11, 41]. The family of hexaferrites consisting of M ($BaFe_{12}O_{19}$), U ($Ba_4Me_2Fe_{36}O_{60}$), W ($BaMe_2Fe_{16}O_{27}$), X ($Ba_2Me_2Fe_{28}O_{46}$), Y ($Ba_2Me_2Fe_{12}O_{22}$) and Z ($Ba_3Me_2Fe_{24}O_{41}$) type, is well known for its magnetic properties. Of all hexaferrites, M-type barium hexaferrites having magneto-plumbite structure with space group P63/mmc exhibits better properties than others. Magneto-plumbite structure of BaM

has dual layer containing sequence of basic RR*SS* stacks. R and R* have hexagonal structure, consist of three oxygen layers with general formula ($BaFe_6O_{11}$) and S and S* have spinal structure with 2 oxygen layers with formula (Fe_6O_8). The asterisk signifies the stack rotation at 180°. There are 38 O^{2-} , 2 Ba^{2+} ions, 24 Fe^{3+} ions in a unit cell of hexagonal ferrite. Fe^{3+} ions are situated in trigonal bi-pyramidal site (2b), tetrahedral site ($4f_1$) and octahedral sites (12 k, 2a and $4f_2$). The presence of 24 ferric ions makes BaM, a good magnetic material. Of these 24 ferric ions, distributed in 5 crystalline positions, two positions ($4f_1$ and $4f_2$) have spin down ferric ions which cause reduction in average magnetic moment of the molecule [2, 78]. The magnetic properties of the BaM can be enhanced by substituting the cations with spin up (like transition metals) at spin down site.

Efforts have been made to enhance the properties of hexaferrite using single cations like Bi [14], Eu [13], La [79, 20], Ga [16], Al [15], Pr, La [17], Er [18], and combination of different cations like Co-Ti, La-Co [24], Mg-Mn-Co-Ti [22], Ca-Cr [21], Co-Ti, La-Na [23], Bi-Ti [25], Mg-Ti [28], Co-Zn-Sn [26], La-Na [80], Mg-Sc [81], Mg-Co [82], La-Zn [27].

Routes available to synthesize BaM are many e.g. glass crystallization method, micro wave induction method [30], sol gel method [32], micro emulsion method [31], sputtering, pulsed laser deposition [32], aerosol pyrolysis technique [50], citrate precursor method [48], and milling method [49]. The optimal technique, sol gel method offers low temperature, procedural simplicity, uniform crystallite size and low operational cost.

BaM, by substituting cations, can be made suitable for various applications. Due to their small ionic radii, rare earth metals and transition metals may replace the barium ions and ferric ions, respectively. This study addresses the synthesis of substituted M-type barium hexaferrite $Ba_{1-x}Nd_xCo_xFe_{12-x}O_{19}$ (x = 0-0.5) (BNCM) via sol-gel auto combustion method using single phase crystallization reaction mechanism, and making detail study of its optical, magnetic, dielectric and structural properties.

7.2. Experimental Procedure

M-type barium hexaferrites $Ba_{1-x}Nd_xCo_xFe_{12-x}O_{19}$ (x = 0-0.5) powders are synthesized via sol gel auto combustion method using analytical grade chemicals such as $Nd(NO_3)_3.\ 6H_2O$ (LOBA Chemie., 99% purity), $Fe(NO_3)_3.9H_2O$ (LOBA Chemie., 98% purity), $Ba(NO_3)_2$ (LOBA Chemie.,

99% purity), $Co(NO_3)_2 \cdot 6H_2O$ (LOBA Chemie., 99% purity), and citric acid ($C_6H_8O_7$) (LOBA Chemie., 99.5% purity). Metal salts and citric acid are dissolved in distilled water in stoichiometric proportions separately and then mixed together at ambient temperature with constant magnetic stirring. Here, citric acid acts as fuel and facilitates the reaction. The molar ratio of cations to citric acid is taken as 1:1.5. Ammonium hydroxide (NH_4OH) solution was added drop wise to maintain the pH of the solution 6.8. After that solution was heated at 80 ˚C – 85 ˚C for 4 - 6 h with continuous stirring using magnetic stirrer. This reaction shows the formation of BNCM:

$$Solution \quad (Ba + Nd + Co + Fe) + C_6H_7O_8 \xrightarrow[Heat]{NH_4OH} precursor \quad (Ba + Nd + Co + Fe)$$

$$\xrightarrow[Heat]{900\,^{\circ}C} Ba_{1-x}Nd_xCo_xFe_{12-x}O_{19}$$

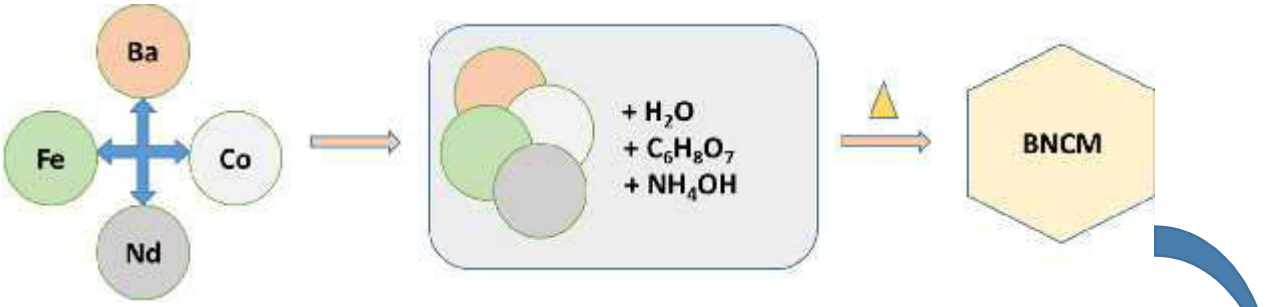

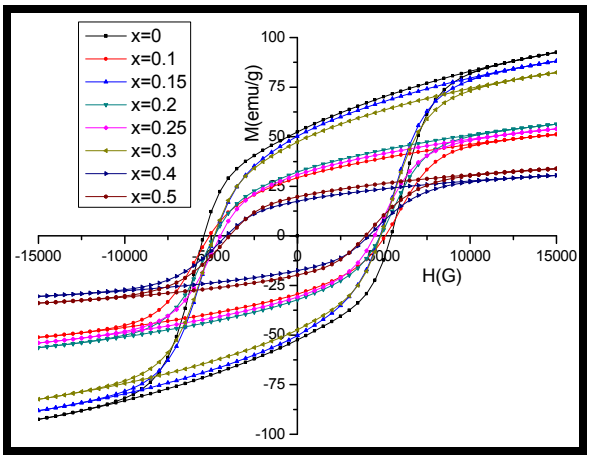

Fig 7.1: Synthesis of BNCM powders

With heat treatment, a homogenous brown coloured gel was formed due to evaporation of water. The viscous solution was dried over hot plate at 280-300 ˚C for 3 h to form the precursor material. The resultant precursor is heat treated at 500 ˚C for 2 h to remove impurities before calcination. The heat treated precursor material is calcined at 900 ºC for 5 h at the rate of 23 ˚C /min (fig. 7.1).

7.3. Characterization techniques

Structural properties have been investigated using X-ray powder diffraction patterns obtained from Bruker AXS D8 Advance X-ray diffractometer in the range 20˚-80˚ using Cu-k_α radiation operating at 40 kV and 35 mA having step size of 0.02˚. Attached functional groups with samples have been analysed with Fourier transform infrared spectra (FT-IR interferometer IR prestige-21 FT-IR (model-8400S)) in the range of 400-4000 cm^{-1}. Thermo gravimetric analyser (TGA) (Perkin Elmer Diamond TG/DTA) is used for thermal analysis under N_2 atmosphere with a heating rate of 10 °C/min from 0 to 850°C. Magnetic properties have been studied with vibrating sample magnetometer (Lakeshore 7410) at room temperature. Dielectric analysis has been performed with LCR meter (Model: 6440B) from 20 Hz to 3MHz. Surface features have been analysed from SEM (Jeol 6390LV) at an operating voltage of 20 kV. The band gap study has been carried out using UV-Vis-NIR (Model: Varian Carry 5000 at room temperature with 0.2 nm resolution).

7.4. Results and discussions

7.4.1. Microstructural properties

BNCM have been investigated by widely-known non-destructive X-ray powder diffractometer technique and presented in Fig.7.2.

Synthesized samples show crystalline phase and absence of impurities (except samples having $x > 0.25$). The presence of apparent peaks having hkl values 110, 008, 107, 114, 203, 205, 217, 2011 and 220 confirms the formation of hexagonal structure of BNCM powders and is similar to peaks in standard pattern (JCPDS-391433). This proves that the substituted ions have occupied the crystal position. Peak of α-Fe_2O_3 appears in samples having $x \geq 0.30$ (shown as * between 107 and 114 peak) and concentration of Fe_2O_3 increases with increase in content of substituents.

Other impurities such as cobalt nitrate (shown with #) and iron nitride (shown with $) are present in the sample that remain unreacted which causes deterioration of the properties. The decrease in peak intensity and reduction of FWHM of fundamental peaks indicate the degradation of crystallization degree as substitution increases. The formation of impure phase is hard to stop after

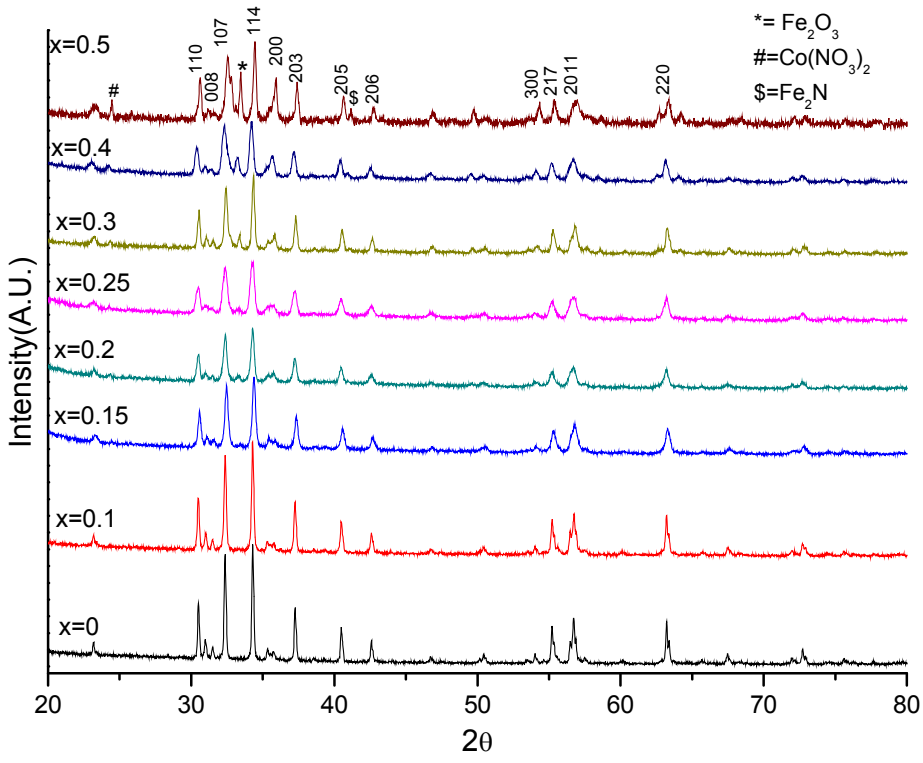

Fig 7.2: X-ray diffraction powder pattern for BNCM for x=0, 0.1, 0.15, 0.2, 0.25, 0.30, 0.4 and 0.5 at 900 ˚C.

x > 0.25. This affirms the occurrence of incomplete crystallisation reaction at atomic level, formation of inhomogeneous mixture of starting compound solutions and synthesis of substituted BaM with hematite phase presence. Lattice constants (a and c) have been obtained (tabulated in table 7.1(a)) from X-ray data using equation [2]:

$$\frac{1}{d_{hkl}^2} = \frac{4}{3}\left[\frac{h^2 + hk + k^2}{a^2}\right] + \frac{l^2}{c^2}$$

where d_{hkl} is d spacing value, *hkl* are miller indices for peaks in XRD powder patterns. It has been found that at x = 0.25, 0.3 and 0.5, lattice constant 'a' has highest value (5.903 Å). There is no significant variation in lattice constant values. Volume of cell has been calculated from [49]: $V_{cell} = 0.8666\ a^2c$. It can be seen that the sample, having x=0.3, has attained the highest volume (701.91 $Å^3$). X ray density has been calculated from following expression [51]:

$$D_x = \frac{ZM}{N_A V_{cell}}$$

where Z is number of molecule per unit cell, M is molecular weight, N_A is Avogadro's number (6.023×10^{23}), and V_{cell} is cell volume.

Table 7.1 (a) Diffraction angle (2θ), d spacing (d), full width at half maxima (β), lattice constants (a and c) and volume of cell (V_{cell}) for BNCM.

x	**2θ(°)**	**d(Å)**	**β (°)**	**Lattice constants**		**V_{cell}(Å^3)**
				a(Å)	c(Å)	
0.00	34.115	2.626	0.14	5.891	23.224	698.46
0.10	34.070	2.629	0.198	5.893	23.205	698.70
0.15	34.071	2.629	0.288	5.892	23.164	696.88
0.20	34.070	2.629	0.341	5.882	23.204	695.71
0.25	34.071	2.629	0.453	5.903	23.164	699.48
0.30	34.126	2.625	0.239	5.903	23.244	701.90
0.40	34.017	2.633	0.380	5.892	23.164	696.88
0.50	34.126	2.625	0.207	5.903	23.164	699.48

Crystallite size (D) has been estimated from Scherer formula [52]:-

$$D = \frac{k\lambda}{\beta \cos\theta}$$

where λ is X-ray wavelength (1.54056 Å), β is full width at half maxima (in radian) and θ is the Bragg angle and k is the shape factor having unit value for hexagonal structure. Crystallite size ranges between 65.95 to 20.32 nm (table 7.1(b)). With increase in concentration of substituents, the crystallite size up to x = 0.25 decreases. This may be due to small ionic radii of Nd (0.905 Å) and Co (0.625 Å) than Fe (0.63 Å) and Ba (1.11 Å) [53].

Table 7.1 (b). X-ray density (Dx), crystallite size (D), phase present and surface area (S) with substitution for BNCM.

x	D_X (g/cm^3)	D(nm)	Phase	$S*10^3$ (m^2/g)
0.00	5.29	65.95	Hexa	17.20
0.10	5.28	46.50	Hexa	24.44
0.15	5.30	31.96	Hexa	35.42
0.20	5.31	27	Hexa	41.85
0.25	5.29	20.32	Hexa	55.82
0.30	5.27	38.53	Hexa-Fe_2O_3	29.55
0.40	5.31	24.22	Hexa-Fe_2O_3	46.65
0.50	5.30	44.48	Hexa-Fe_2O_3	25.45

Surface area has been calculated (shown in table 7.1(b)) from the expression [2]:

$S = \frac{6000}{DD_x}$, where D is crystallite size and D_x is X-ray density. The specific surface area shows an increase in its value from 17.20 to 55.82 m^2/g. Crystallite size is the dominant factor for variation in surface area. As the crystallite size decreases, the more number of atoms appear at the surface.

7.4.2 FT-IR

Fourier transform infrared spectra in the range 400-4000 cm^{-1} have been obtained for BNCM samples calcined at 900 ˚C. The pallets of samples have been prepared with sample to anhydrous KBr in the ratio 1:10 to take the FT-IR spectra. The information regarding attached molecular bands or presence of functional groups, which are remains of chemicals used in synthesis process, can be obtained from FT-IR spectra analysis (Fig 7.3). Two prominent peaks, arise near 430 and 580 cm^{-1}, indicate the formation of hexaferrite. The stretching vibrations of metal-oxygen bond are the reason for these characteristic peaks. A small peak near 855 cm^{-1} indicates the presence of carbonate at x=0.5. The bands near 420-480 cm^{-1} and 550-590 cm^{-1} attribute to the vibration of ferric crystallographic site [$4f_2$ and $4f_1$ with vibrational mode A_{2u} and E_{1u} (octahedral and

tetrahedral)] [55]. Relatively more prominent peaks in FT-IR spectrum of x = 0.15 show that the cations have been substituted at the ferric sites accompanying strong interaction than other samples. Nitrates ions (near 1300 cm^{-1}) [56] and moisture absorbed (2900 cm^{-1}) [58] have not been found in the samples. Peak at 2400cm^{-1} shows the presence of CO_2.

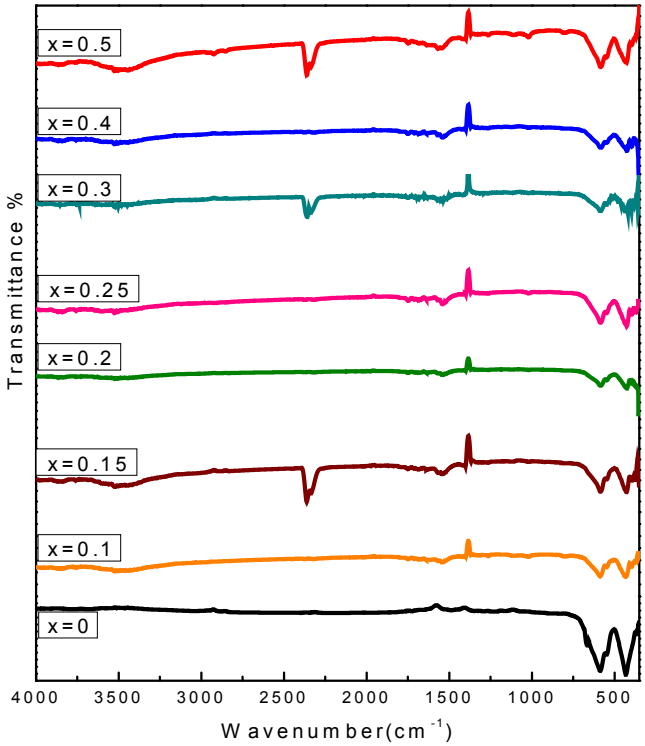

Fig 7.3. Fourier Transform infrared spectra of the samples of BNCM for x=0, 0.1, 0.15, 0.2, 0.25, 0.30, 0.4 and 0.5 at 900 ˚C.

7.**4.3. Thermal analysis**

Thermal gravimetric analysis/ differential thermogravimetric analysis / derivative thermogravimetry (TGA/DTA/DTG) have been performed to investigate the effect of heat on sample. The resultant TGA/DTA/DTG plots of M-type hexaferrite $Ba_{1-x}Nd_xCo_xFe_{12-x}O_{19}$ (x = 0.30)

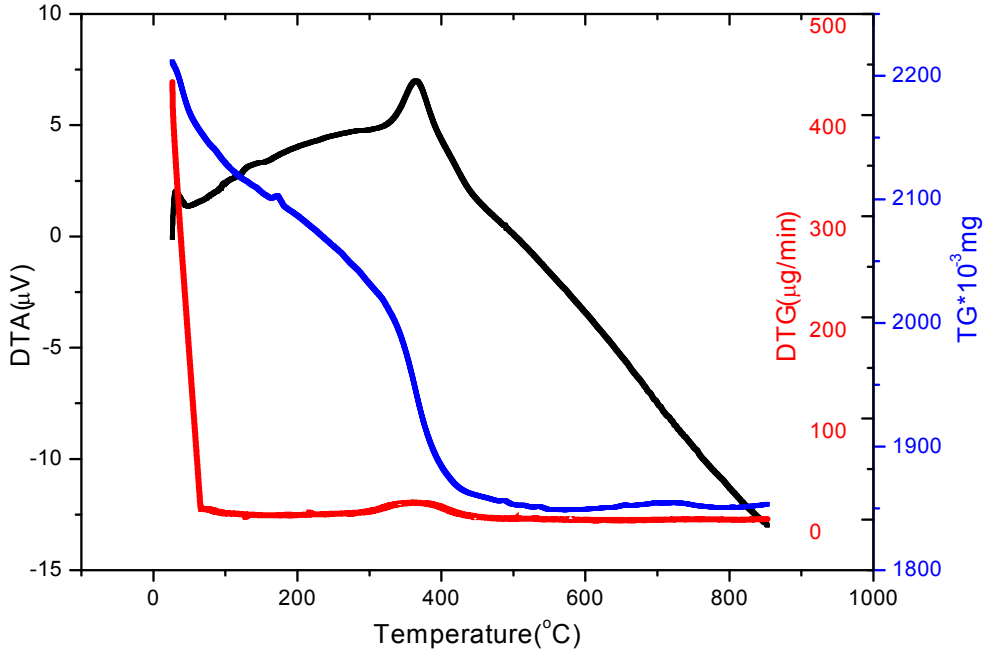

Fig 7.4. TGA/DTA/DTG diagram for $Ba_{0.7}Nd_{0.3}Fe_{11.7}Co_{0.3}O_{19}$ precursor.

(BNCM) powder have been shown in Fig 7.4. The reduction of weight between 0 ˚C to 440 ˚C is due to decomposition of remaining organic matter, decomposition of precursor and conversion of haematite into hexaferrite phase. Oxidation reduction reaction between the metal nitrates and citric acid is the reason for decomposition [59]. After 440 ˚C weight loss becomes approximately constant which indicates the formation of BNCM. The reaction interval for the BNCM is 340 ˚C. In DTA curve, the first variation in peak is near about 100 ˚C associated with endothermic peak on account of loss of water. The prominent effect shown by TGA/DTA/DTG is at 363 ˚C. DTA gives exothermic peak and DTG (Differential thermogravimetry) gives slight peak because of recrystallization of sample.

7.4.4 Morphology

SEM micrographs of BNCM at room temperature with Nd-Co substitution are shown in Fig 7.5. It is observed from the micrographs that the samples have uneven distribution of crystallites, randomly packed crystals and irregular shape. The presence of clusters in some parts can be seen.

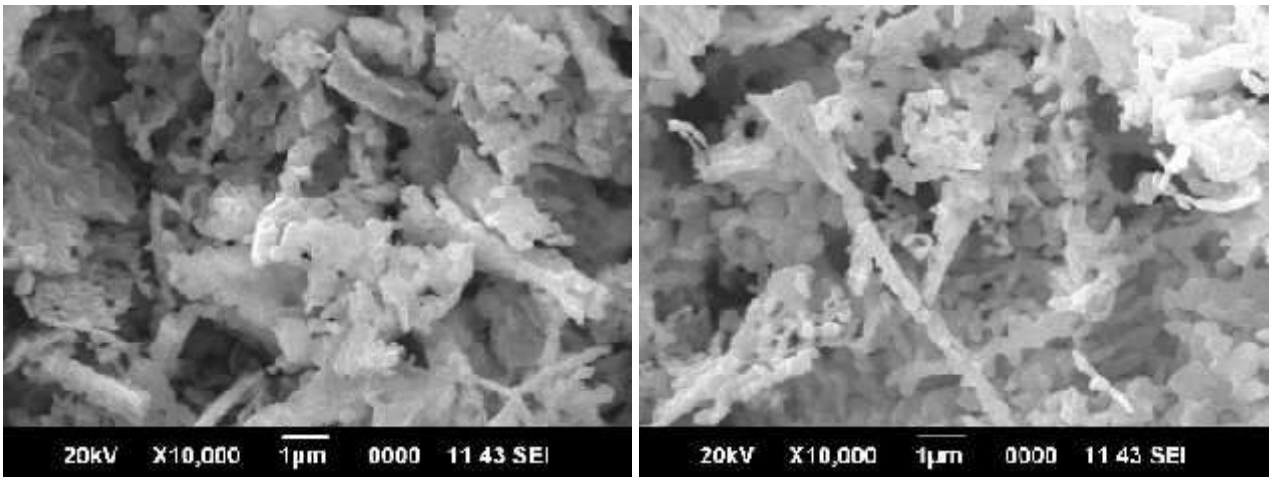
20kV X10,000 1µm 0000 11 43 SEI
20kV X10,000 1µm 0000 11 43 SEI

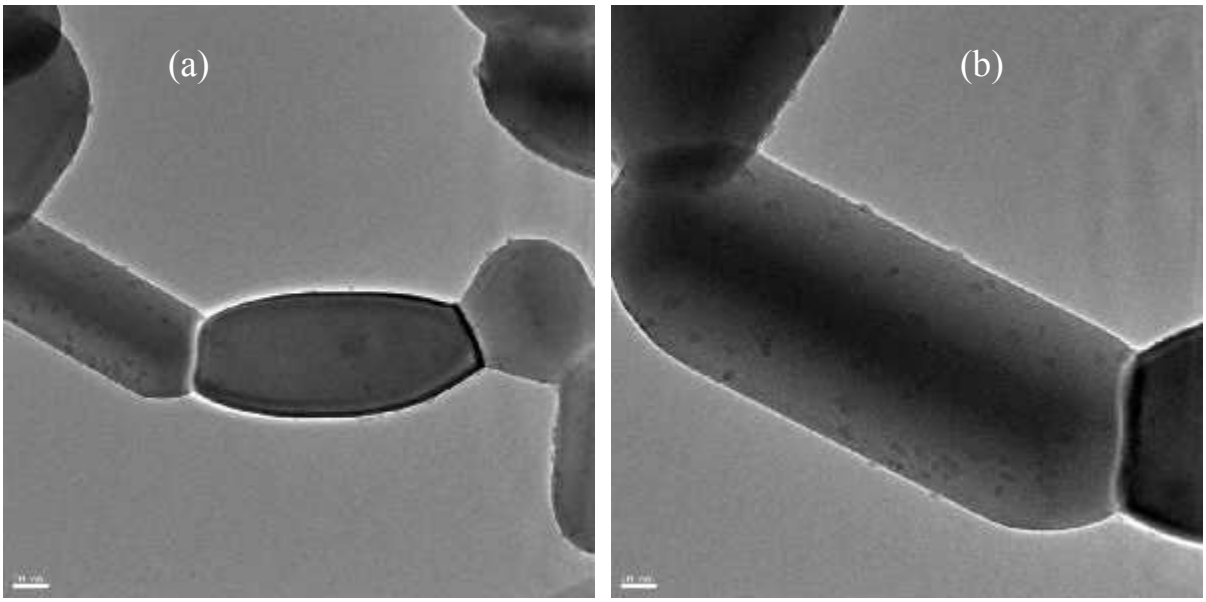
(a)
(b)

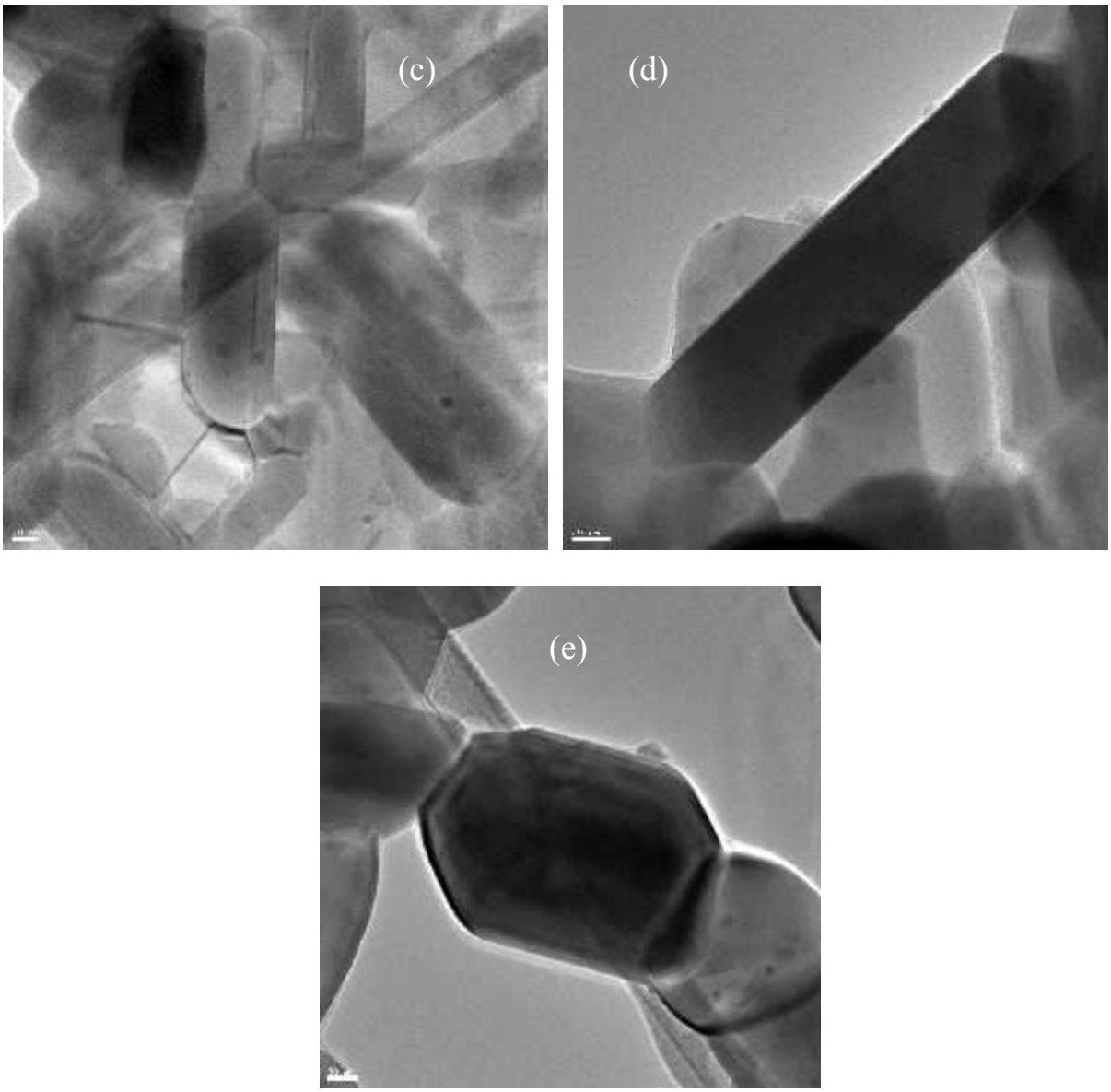

Fig 7.5: SEM micrographs for BNCM (x=0.30), TEM images for BNCM (a and b) x=0.1 and (c, d and e) x= 0.25

TEM images reveals that the particle size is in nano range. Hexagonal shape can be clearly seen in the images.

7.4.5. **LCR**

Capacitance has been recorded on LCR meter in a range 20 Hz to 3 MHz using a pellet (with 8 tonne pressure) of calcined sample of BNCM coated with silver metal powder.

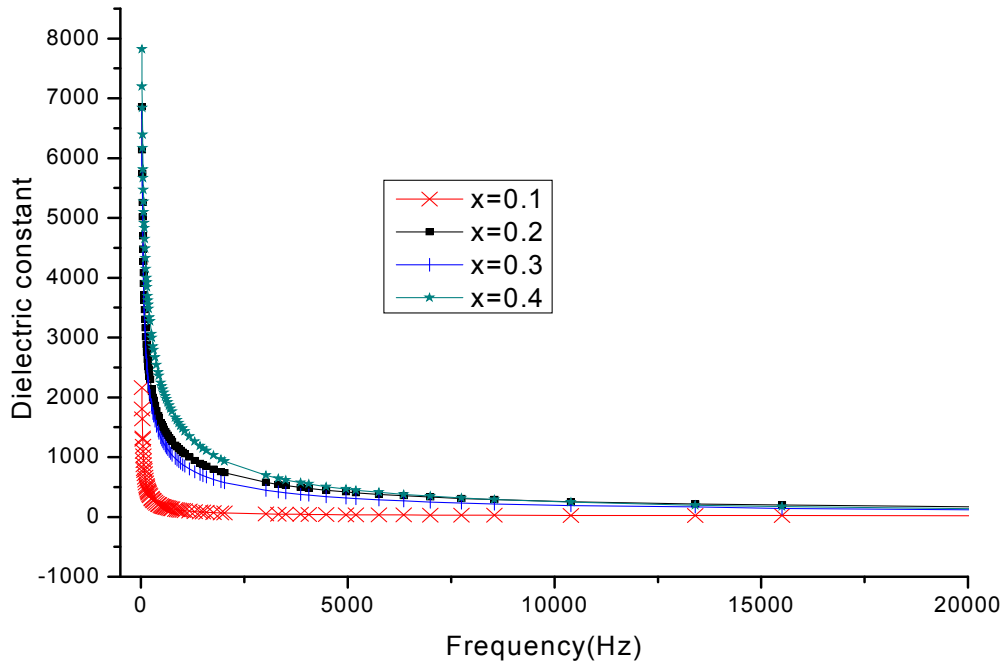

Fig. 7.6: Variation of dielectric constant with frequency

Dielectric constant has been calculated from parallel plate capacitor equation [60]:

$$K = \frac{Cd}{\varepsilon_0 A}$$

Where K is dielectric constant, C is capacitance of the palette, d is thickness of sample palette and A is cross section area and ε_o is the permittivity of free space (8.85 x 10^{-12} F/m). A very high dielectric constant has been shown by the BNCM. The sample with x = 0.4 shows the highest dielectric constant among the samples. It is due to the nano-size level. As from XRD data, x = 0.4 has the smaller size than the sample having x = 0.1, 0.2 and 0.3. The crystallites at nano-level possess very high surface area. Due to large surface area, the space charge polarization will be high that results in high dielectric constant. Moreover the samples contains impurity, so increase of ferrous ions coming from impurity also increases the dielectric constant. Because ferrous ions are more likely to get polarized. The substitution can distort the structure and can make ions by creating surface defects that can leads to the increase in number of ions and causing high dielectric constant.

A normal behaviour of ferrite has been shown by BNCM (Fig 7.6) towards frequency that is dielectric constant is high for low frequency but decreases at high frequency. Koop's

phenomenological theory and Maxwell Wagner theory can be used to explain such nature of BNCM. According to their theory there may be an electron exchange between Fe^{3+} and Fe^{2+} which is responsible for polarization and results in the displacement of the ionic charges and causes polarization. At low frequencies, the presence of grain boundaries also effectively contributes in polarization. The structure of material is supposed to be made of conducting grains separated by less conducting grain boundaries [61]. They may be created during heat treatment. The hopping of electrons between Fe^{2+} and Fe^{3+} causes dispersion at low frequency. The electrons have been displaced by applied field and causes polarization but when half of alternating field becomes more than hopping time, the displacement does not happens [62]. Because of low eddy currents and high dielectric constant, prepared material can play a significant role in electronics market as an application point of view in as radiation absorber or high frequency component.

7.4.6 UV-VIS spectroscopy

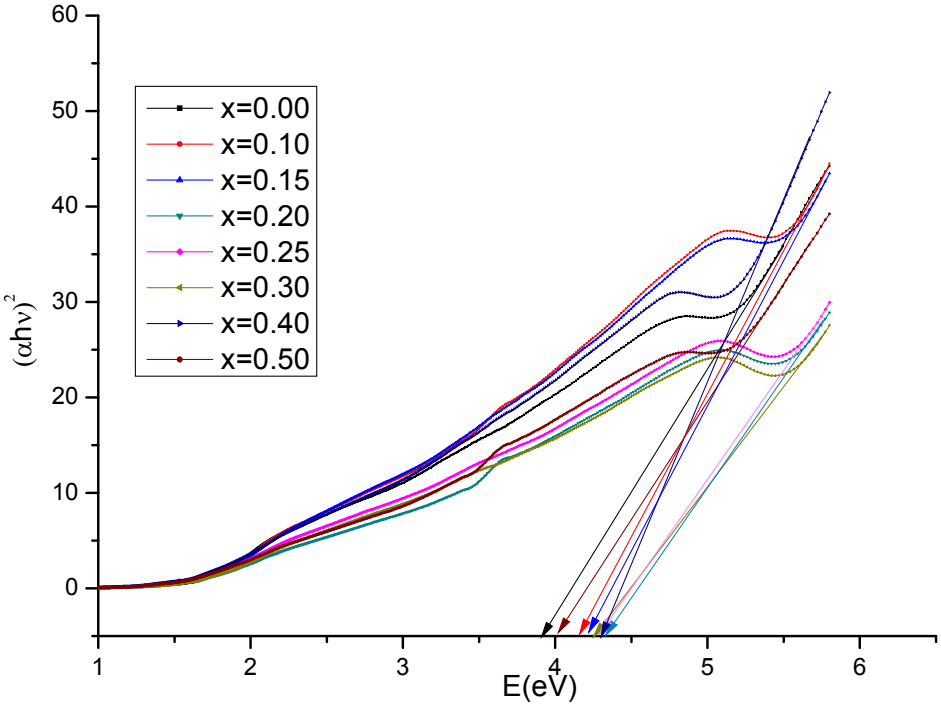

Fig. 7.7: Graph between Optical energy and absorption for BNCM (x = 0 - 0.5) at 900 ˚C

Table 7.2 Band gap values with substitution for BNCM.

S. No	x	Band gap (eV)
0	0.00	3.91
1	0.10	4.16
2	0.15	4.21
3	0.20	4.33
4	0.25	4.30
5	0.30	4.25
6	0.40	4.31
7	0.50	4.00

The optical properties of BNCM in optical region (200-800 nm) has been studied by using UV–Vis-NIR absorption spectra. The absorbed band gap energy has been calculated from the spectrum using following relation [64]:

$$\alpha = \frac{A(h\nu - E_g)^{1/2}}{h\nu}$$

Where E is energy band gap and A is a constant. Fundamental absorbance edges in plotted graph are used to calculate the band gap in electron volt. Figure 7.7 and 7.8 show the spectra for energy band gap and the absorbance spectra. The band gap of pure barium hexaferrite has been obtained 3.91 eV (table 7.2). It is observed that the band gap energy increases with increase in substitution concentration from x = 0 to x = 0.20 and shows maximum value 4.33 eV at x = 0.20 and after x =0.20, band gap energy do not follows a regular energy value variation. Quantum confinement is the dimensional effect that depends on the particle size, all the samples are in nano size so causing quantum confinement but after x=0.20, the size shows irregular pattern as fig 7.9. So the band gap also varies in that trend. BaM shows low value of band gap than BNCM. Band gap of BNCM is higher than barium hexaferrite (3.18eV) and barium hexaferrite thin films (2.32eV) as reported by others [64, 65]. The increase in band gap may be due to the occurrence of quantum confinement. From UV-NIR absorption spectra (Fig 7.8), it has been concluded that the absorption region for hexaferrites is ~ 200 - 600 nm. It has been observed that band gap strongly depends on the size of the nano-crystallites and varies inversely with crystallite size (Fig. 7.9). Discrete electronic energy

levels result in the materials due to quantum confinement. The energy separation between adjacent energy levels increases with decreasing dimensions just like a particle in a box problem in quantum mechanics.

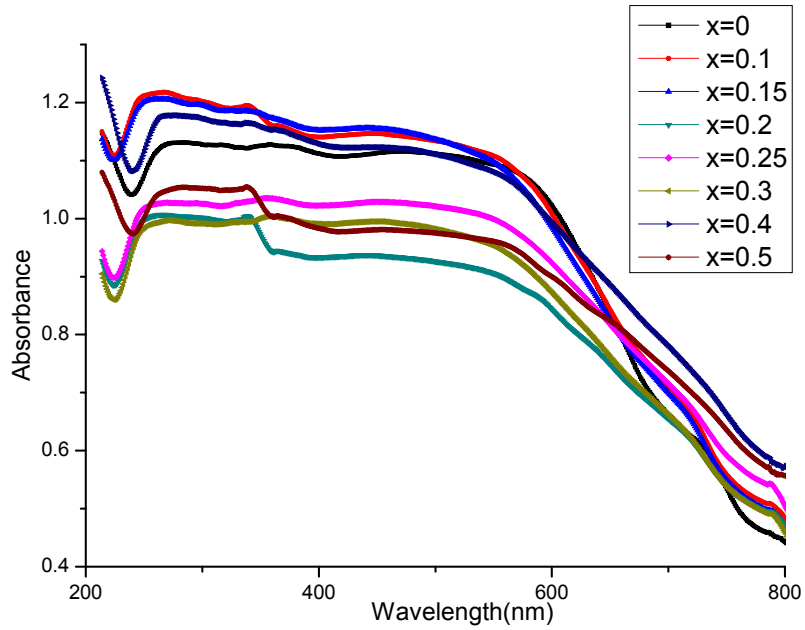

Fig 7.8. Absorption spectra for BNCM (x=0-0.5) at 900˚C

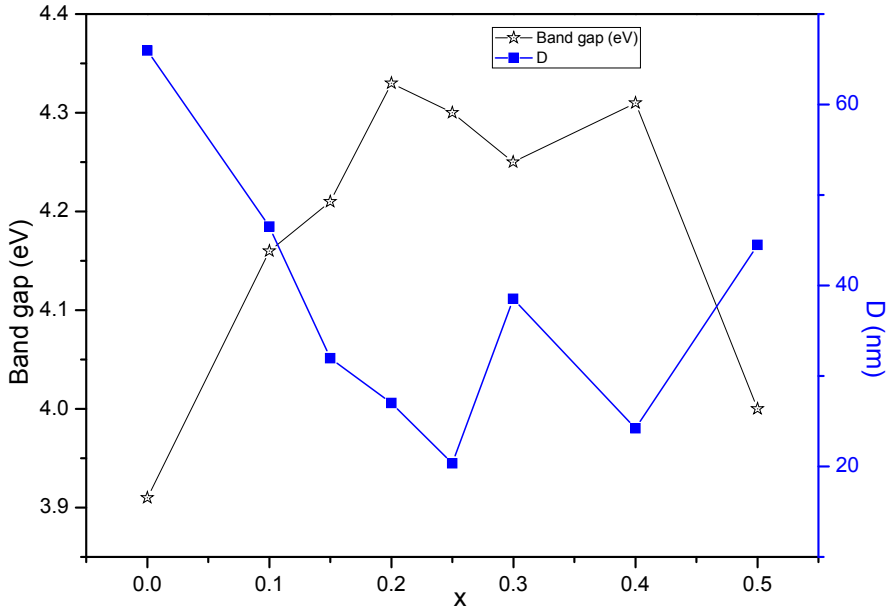

Fig 7.9: Variation of crystallite size and band gap with substituent concentration n BNCM.

7.4.7. Magnetic properties:

The magnetic properties has been evaluated from hysteresis curve (Fig 7.10) and summarize in table 7.3. Effect of substitution of Nd^{3+} and Co^{2+} has been seen on coercivity (Fig 7.11) and saturation magnetization. It is interesting to get a patterned structure of M–H curves, e.g. samples x = 0.0, 0.15, 0.3, x = 0.2, 0.25, 0.1 and x = 0.4, 0.5 have almost similar variation. Saturation magnetization (M_S) value for pure barium hexaferrite is 92.53 emu/g and M_S value for BaM is more than substituted samples. Saturation magnetization (M_S) of samples depends on magnetic moment of ions at different sites of hexaferrite. In pure hexaferrite (BaM), the increase in M_S may attribute to the site occupying by the Fe ions with spin up rather than spin down. The lowest value for M_S is 29.57 emu/g for x=0.40 which may be due to presence of impurities in the samples as discussed in XRD analysis.

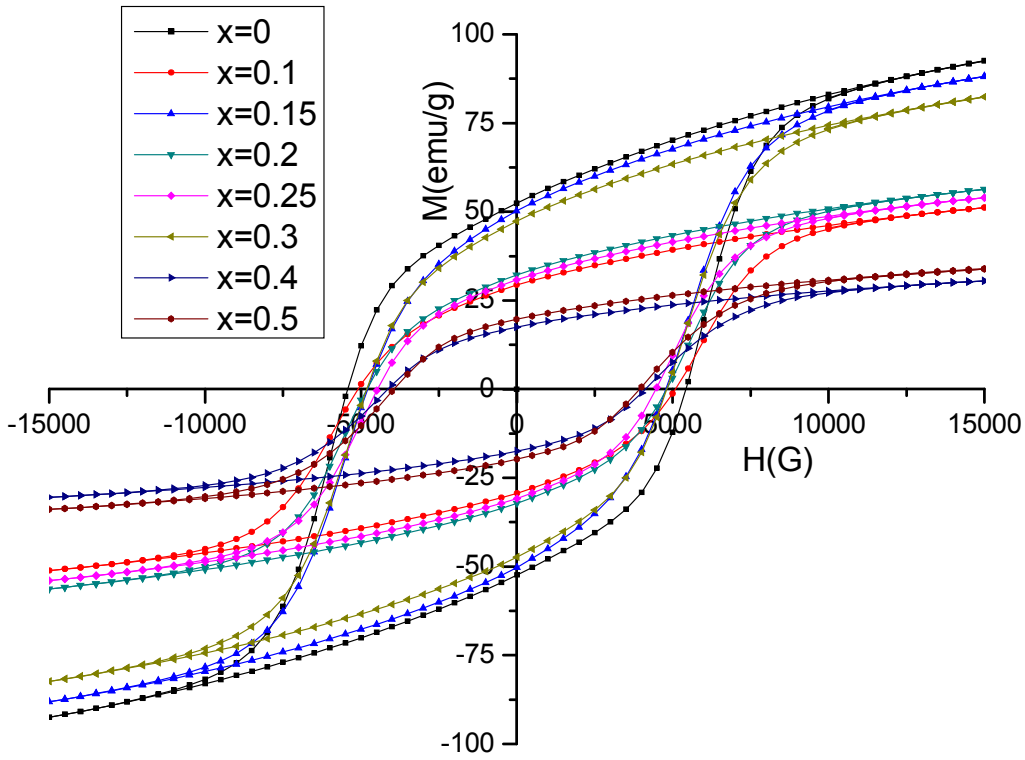

Fig. 7.10: Hysteresis loop for BNCM (x = 0 - 0.5) at 900 ˚C

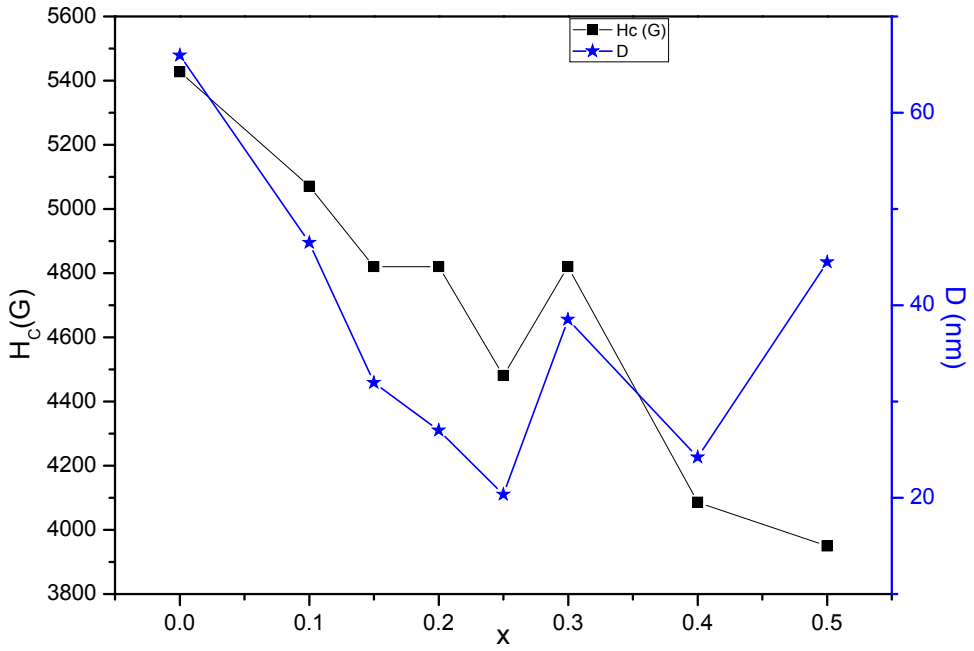

Fig. 7.11: Variation of crystallite size and coercivity with substitution

Table 7.3: Summary of Coercivity (H_C), saturation Magnetization (Ms), Retentivity (M_R), Squareness Ratio (SR) and Anisotropy constant (K) with substitution for BNCM.

x	H_C (G)	Ms (emu/g)	M_R (emu/g)	SR(M_R / Ms)
0.00	5427	92.53	52.42	0.566
0.10	5071	49.45	29.32	0.593
0.15	4820	85	50.22	0.59
0.20	4820	54.22	32.09	0.592
0.25	4481	51.97	30.30	0.583
0.30	4820	79.66	47.71	0.599
0.40	4086	29.57	17.74	0.599
0.50	3949	32.60	19.70	0.604

Saturation magnetization do not follows a regular trend in its value variation with substitution, but a patterned curve can be seen. Such kind of variation may depend on number of causes like density of atoms, ionic radii, completion of reaction, impurities presence. There

is also decrease in the crystallite size of BNCM which increases the number of magnetic domains in BNCM powder samples. Coercivity value has less been affected by substitution. Coercivity also depends on structural properties, defects, crystallite size [53].

Conclusion

The formation of hexagonal structure takes place and the morphology of the surface of the as-prepared samples is a non-homogenous. It has been observed that the hexaferrite phase forms at a temperature of 680 ˚C. Samples show normal ferrite dielectric behaviour. UV –Vis-NIR reveals that the band gap of as-prepared samples increases with substitution. Synthesized material can advantageously utilized in the formation of the thermally stable, perpendicular magnetic recording media having ultra-high areal recording densities in several Gbit/in^2.

CHAPTER-8

MOSSBAUER, DIELECTRIC, OPTICAL, MULTIFERROIC AND STRUCTURAL PROPERTIES OF SUBSTITUTED BARIUM HEXAFERRITE

Abstract

Gd-Co substituted M-type barium hexaferrite, $Ba_{1-x}Gd_xCo_xFe_{12-x}O_{19}$ ($0.0 \leq x \leq 0.6$) have been successfully synthesized by sol-gel method. The formation of crystalline magneto-plumbite structure of M-type hexaferrite and presence of other phases are noticed by X-ray diffraction analysis. An average crystallite size, calculated by Scherer formula is found to be between 26.11 nm to 65.77 nm. The presence of two peaks at 430 cm^{-1} and 580 cm^{-1} in FT-IR spectra is pointing the presence of octahedral and tetrahedral sites in hexaferrites. Vibrational modes in FT-Raman spectra supports the formation of P63/mmc group related with hexaferrite magneto-plumbite structure. Thermal analysis reveals that the hexaferrite phase occurs at approximately 700 °C. For more clarity, morphology analysis is carried out using SEM (Scanning Electron Microscope), AFM (Atomic Force Microscope) and TEM (Transmission Electron Microscope). UV-Vis-NIR spectra shows that the substitution increases the band gap of the material from 3.99 eV to 4.28 eV. The Fe^{3+} ions are responsible for the observed peak to peak line width and occurrence of symmetrical resonance in electron spin resonance (ESR) spectra. The dielectric constant shows high value at low frequency and it becomes constant at high frequency. The retentivity and coercivity of the material decreases with increasing substitution. I-V characteristics of the syntheized materials exhibits a linear plot. Multiferroic nature of hexaferrite is analysed using ferroelectric loops. The decrease in magnetic properties with substitution is explained using Mossbauer spectra.

8.1. Introduction

In the field of electromagnetic compatibility, the microwave absorbing material has been used to decrease the electromagnetic interference and electromagnetic backscattering, as the setup of trends in development of higher Gigahertz frequency devices and inclination towards miniature

circuit devices. Regarding this, the hard magnetic material i.e. barium hexaferrite has been exploited because of its tuneable magnetic properties. Besides many applications, barium hexaferrite is also used in multi-layer chip inductors as the surface mounting devices for miniature circuit devices. This is all because of its mechanical, magnetic and dielectric properties. For Multi-chip layer inductor, the ferrite layer get interweaved with suitable conductor. For such applications, the desired magnetic and dielectric properties holding material like barium hexaferrite is required. The properties of barium hexaferrite strongly depends on crystallite size, ions distribution and synthesis method [83, 84]. Substitution is a versatile tool for enhancement of the properties of the material. So an extensive study, carried out by several authors, can be found out in the literature on the basis of substitution [13-18, 20-23, 25-27, 46, 47, 76, 84, 85, 86]. Due to small ionic radii, rare earth metal and transition metal may replace the barium ions and ferric ions, respectively.

To make BaM suitable for different applications, the properties of BaM are required to tailor which can be accomplished by substituting cations. Many routes are available to synthesize BaM [30-32, 48, 49, 87]. The optimal technique, the sol gel method is advanced and offers low temperature, procedural simplicity, good yield, uniform crystallite size and low operational cost.

The aim of the present research work is to thoroughly investigate the optical, magnetic, dielectric, multiferroic, Mossbauer, electronic and structural properties after substituting Gd-Co on BaM so that the prepared material can be utilized in magnetic recording media, insulators and electromagnetic attenuation material. Cobalt has been taken as a transition metal substituent due to its ability to dissolve the rare earth elements that may enhance the properties like structural, dielectric and magnetic properties etc [88-102].

8.2. Synthesis of substituted nanocrystalline $BaFe_{12}O_{19}$

Modified Pechini sol-gel method [82] has been employed to synthesize M-type barium hexaferrites $Ba_{1-x}Gd_xCo_xFe_{12-x}O_{19}$ (x = 0 - 0.6) powders using AR grade chemicals, used without further purification, such as $Gd(NO_3)_3 \cdot 6H_2O$ (LOBA Chemie., 99% purity), $Fe(NO_3)_3.9H_2O$ (LOBA Chemie., 98% purity), $Ba(NO_3)_2$ (LOBA Chemie., 99% purity), $Co(NO_3)_2 \cdot 6H_2O$ (LOBA Chemie., 99% purity), and citric acid ($C_6H_8O_7$) (LOBA Chemie., 99.5% purity). Iron and metal salts are dissolved in distilled water separately in stoichiometric proportions. All the dissolved metal nitrates are mixed together at ambient temperature with constant magnetic stirring. Citric acid has been added as a fuel with cations to citric acid molar ratio of 1:1.5. For neutralization of the solution

(pH = 6.8), ammonium hydroxide (NH_4OH) solution is added drop wise. After that, solution is heated at 80 ˚C - 85 ˚C for 4-6 hours with continuous stirring using a magnetic stirrer. The nano particles can be crystallized in the optimum condition. The environment of solution (i.e. pH value, metallic ions, fuel ratio) effects the crystallization process. Citric acid acts as a fuel as well as chelating agent by making complex ions. But, for complex ion formation, pH should be in neutral range (6-7.5). So, pH of solution is maintained at 6.8.

With heat treatment, the liquid converts into a homogenous brown coloured gel. The viscous solution (gel) has been dried over a hot plate at 280-300 °C for 3 hours to form the precursor material. Pre-sintering has been done at 500 °C for 2 hours to remove impurities. Finally, precursor material is heated at optimized calcination condition i.e. 900 °C for 5 hours at the rate of 23 °C/min.

8.3. Results and discussions

Non isothermal testing techniques like thermal gravimetric analysis (TGA) and derivative thermogravimetry (DTG) have been employed for thermal analysis, in which, constant heating rate effect has been studied on variable parameter like weight of the sample.

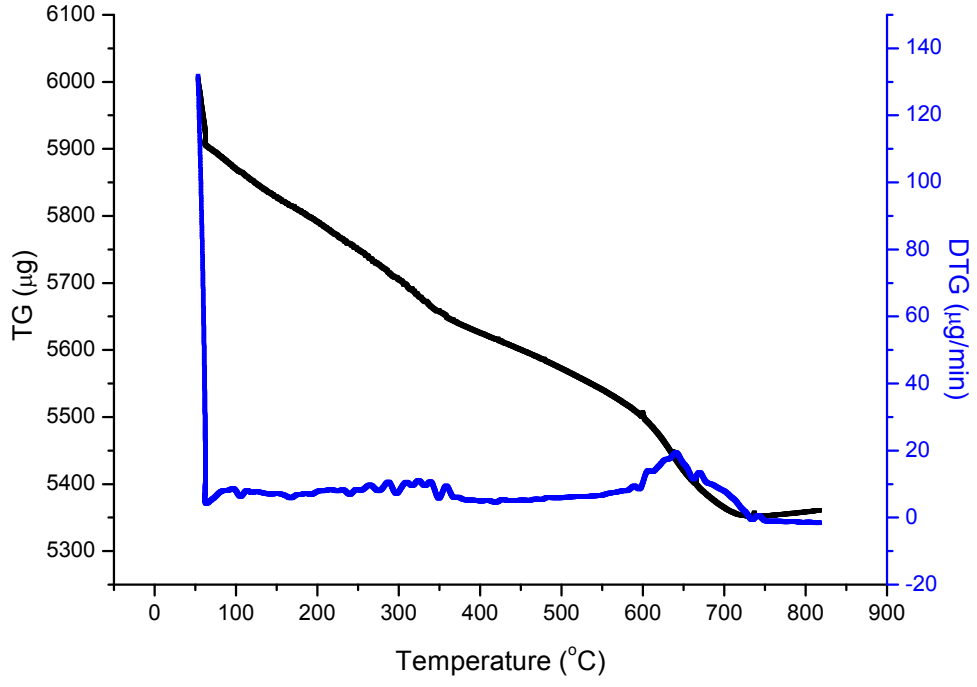

Fig 8.1. Thermal gravimetric analysis/ derivative thermogravimetry (TGA/DTG) diagram for $Ba_{0.7}Gd_{0.3}Fe_{11.7}Co_{0.3}O_{19}$ precursor.

Testing has been carried out under N_2 atmosphere (Perkin Elmer Diamond TG) with a heating rate of 10 °C/min from 0 to 850 °C. A dried precursor has been subjected for TGA/DTG. The resultant patterns of M-type hexaferrite $Ba_{1-x}Gd_xCo_xFe_{12-x}O_{19}$ (x = 0.30) (BGCM) powder has been shown in Fig. 8.1. TGA and DTG plots are consistent with each other.

The two distinct peaks of weight loss can be clearly seen in the pattern of TGA/DTG. The first weight loss occurs from 60 - 600 ˚C. This weight loss may arise due to evaporation of water and the liberation of other gases like CO_2 and N_2. The evolution of gases cause improvement of redox reaction. A small and broad peak near 300 °C in TGA and DTG indicates the slight weight loss which may be due to decomposition of remaining organic matter caused by the reduction reaction between fuel (citric acid) and metal nitrates. The second peak and weight loss in TGA and DTG occur between 600 °C and 700 °C. In this range of temperature, conversion of hematite to hexaferrite phase takes place due to decomposition of precursor [69]. After a 700 °C, weight loss becomes approximately constant which indicates the formation of BGCM. The reaction interval for the BGCM is 650 °C.

X-ray studies is a versatile tool for identification of present phases, crystal structure and to calculate unit lattice dimensions. Structural properties of ground powders of BGCM have been investigated using X-ray diffraction (XRD) powder patterns, obtained from Bruker AXS D8 Advance X-ray diffractometer in the range 20° to 80° using Cu-kα radiation, operating at 40 kV and 35 mA, having step size of 0.02°. The X-ray patterns of BGCM, calcined at 900 °C for 5 hours, have been presented in Fig. 8.2. The presence of sharp peaks in X-ray patterns reveals the formation crystalline phase. Some impurities have been observed in all the samples except the sample having x = 0.1. The presence of apparent peaks having hkl values 110, 008, 107, 114, 203, 205, 217, 2011 and 220, which are identical to peaks in standard pattern (JCPDS-391433), confirms the hexagonal structure of BGCM powders. This comparison shows that the substituted ions have occupied the crystal positions. Peak of α-Fe_2O_3 appears (shown as * between 107 and 114 peak) in all samples except x = 0.1. Other impurities like cobalt nitrate (shown as $) and iron nitride (symbolized as #) are also present in the samples.

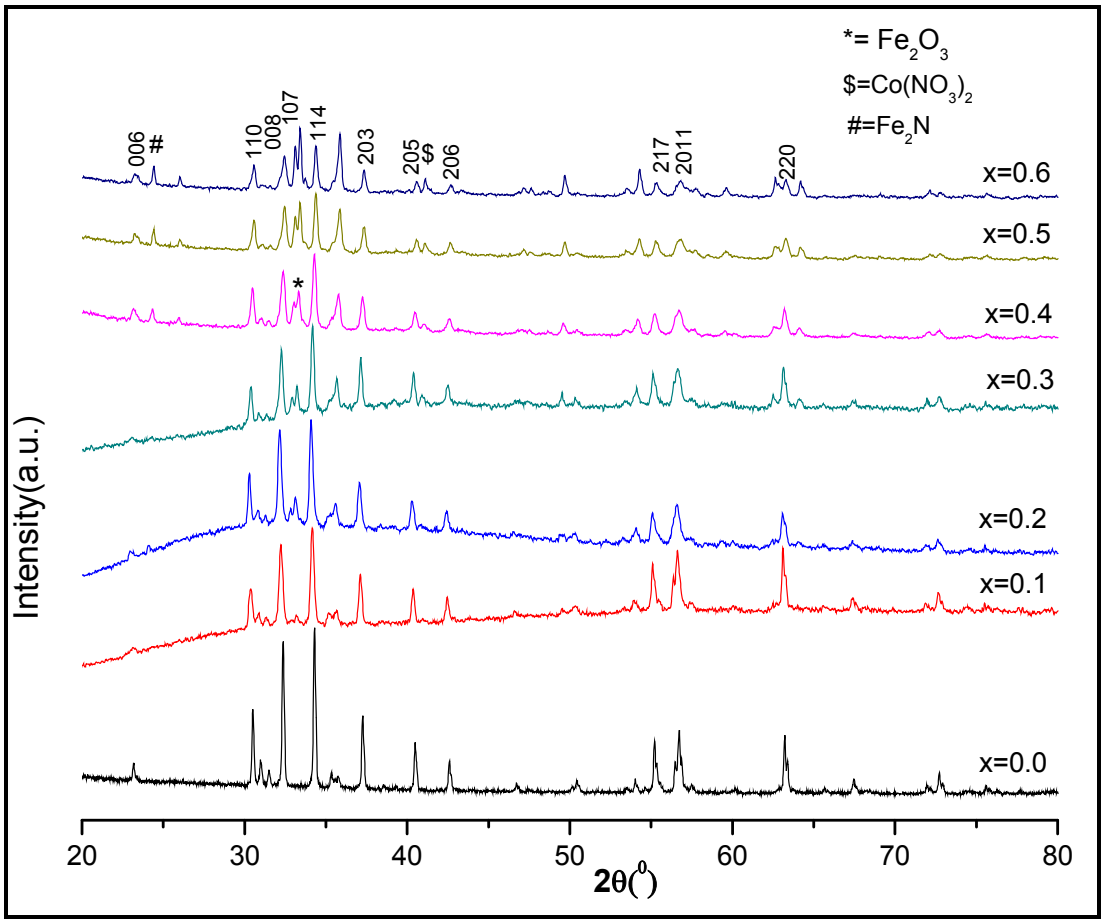

Fig 8.2: X-Ray diffraction powder pattern for $Ba_{1-x}Gd_xCo_xFe_{12-x}O_{19}$ (x = 0-0.6)

The peak intensity of present impurities increases with increase in substituent concentration. This may be due to the less solubility of gadolinium in BaM. The occurrence of impurities is the result of incomplete crystallization reaction and the formation of an inhomogeneous mixture of starting material solutions. Lattice constants (a and c) have been obtained (tabulated in Table 8.1) from X-ray data using equation [63]:

$$\frac{1}{d_{hkl}^2} = \frac{4}{3}\left[\frac{h^2 + hk + k^2}{a^2}\right] + \frac{l^2}{c^2}$$

where d_{hkl} is inter planner spacing, hkl are the Miller indices for peaks in XRD powder patterns. It has been found that the sample having x = 0.2, lattice constants 'a' and 'c' are showing highest value (5.977 Å and 23.545 Å).

Table 8.1. Diffraction angle (2θ), d spacing (d), full width at half maxima (β), lattice constants (a and c), volume of cell (V_{cell}), X-ray density (D_X), crystallite size (D), porosity (%), phase present and surface area (S) with substitution for BGCM.

x	2θ(°)	d(Å)	β (°)	Lattice constants		V_{cell}	D_X	P (%)	D	Phase	$S*10^7$
				a=b (Å)	c (Å)	($Å^3$)	g/cm^3		(nm)		(cm^2/g)
0.0	34.115	2.626	0.140	5.891	23.224	698.46	5.29	74.80	65.77	Hexa	17.26
0.1	33.743	2.654	0.278	5.966	23.489	724.59	5.10	45.01	33.09	Hexa-Fe_2O_3	35.53
0.2	33.634	2.662	0.292	5.977	23.545	728.89	5.08	44.88	31.49	Hexa-Fe_2O_3	37.47
0.3	34.070	2.629	0.261	5.893	23.245	699.54	5.31	62.52	35.28	Hexa-Fe_2O_3	32.04
0.4	34.288	2.613	0.241	5.862	23.046	686.30	5.42	46.51	38.23	Hexa-Fe_2O_3	28.95
0.5	34.451	2.601	0.353	5.842	22.967	679.21	5.49	50.48	26.11	Hexa-Fe_2O_3	41.86
0.6	34.397	2.605	0.200	5.842	23.007	680.37	5.49	46.45	46.07	Hexa-Fe_2O_3	23.71

The lattice constants decrease with increase in substitution from x = 0.3 to x = 0.6. The main reason for contraction may be due to the presence of microstructural defects, interaction between substituted cations and substitution of ions having smaller ionic radii than the host ions. The diffraction patterns are showing peak shifting of substituted towards lower d-spacing (than pure hexaferrites). This may happens with the induction of strain with substitution. Volume of the cell has been calculated from [64]: $V_{cell} = 0.8666\ a^2c$. The highest volume (728.89 $Å^3$) has been attained by sample having x = 0.2. X ray density has been calculated from following expression [64]:

$$D_X = \frac{ZM}{N_A V_{cell}}$$

where Z is the number of molecules per unit cell, M is the molecular weight, N_A is Avogadro's number (6.023×10^{23}), and V_{cell} is the cell volume.

Crystallite size (D) has been estimated from the well-known Scherer formula [64]. Crystallite size ranges between 26.11 nm to 65.77 nm (Table 8.1). This crystallite size is in the favourable range from application point of view. Crystallite size of substituted hexaferrites is smaller than barium hexaferrite. This may attribute to the binding energy of RE^{3+}-O^{2-}, which is higher than Fe^{3+}- O^{2-}. This statement has also been supported by UV-Vis-NIR study. Segregation effect of rare earth metal ion can also be behind the reduction of crystallite size. High binding energy material need high energy for crystallization and hence become more thermally stable. With an increase in concentration of dopants, the crystallite size and c/a ratio vary and no trend has been observed. Surface area has been calculated (shown in Table 8.1) from the expression [1]:

$S = \frac{6000}{DD_X}$, where D is crystallite size and D_X is X-ray density. The specific surface area shows an increase in its value from 17.26×10^7 to 41.86×10^7 cm^2/g. Crystallite size is the dominant factor for variation in surface area. As the crystallite size decreases, the more number of atoms appear at the surface. Consequently, the prepared material can be utilized in perpendicular recording media.

Furthermore, the synthesize material is in nano range causing an enhancement in the number of crystallites per bit area that would increase the signal to noise ratio that is suitable for the purpose.

Porosity for the synthesized sample can be estimated by using relations [1]:

$$P = \left(\frac{D_x - D_b}{D_x} \right) \times 100$$

where $D_b = \frac{m}{\pi r^2 d}$, D_x is X ray density, D_b is bulk density and can be calculated from mass (m) and volume of palette having radius (r) and thickness (d).

Porosity shows a decrement upon substitution. The increase in bulk density causes decrease in porosity. Porosity is high for barium hexaferrite than the substituted hexaferrites. Bulk density is increased due to incorporation of substituents having high density {Gd^{3+} = 7.90 g/cm^3, Ba^{2+}= 3.51

g/cm^3, Fe^{3+}= 7.874 g/cm^3, Co^{2+}= 8.90 g/cm^3}. Heat treatment and substitution can cause shape defects and may be the reason for arise of porosity.

For quantitative and qualitative analysis of attached functional groups and impurities, which are remains of chemicals used in the synthesis process of Gd-Co substituted hexaferrite,studies have been performed using Fourier transform infrared spectra (FT-IR interferometer IR prestige-21 FT-IR (model-8400S)) in the range of 400-4000 cm^{-1}. The pallets for FT-IR spectra have been prepared with sample to KBr in the ratio 1:10.

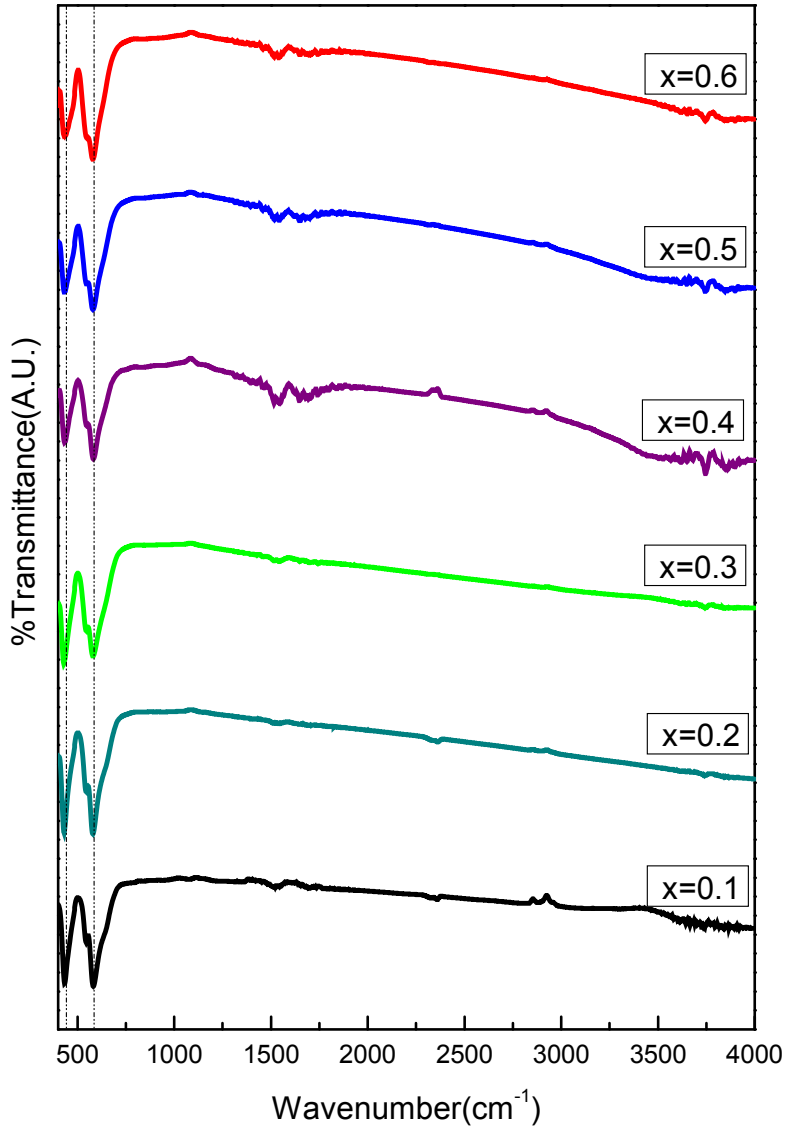

Fig 8.3. Mid infra-red region spectra for $Ba_{1-x}Gd_xCo_xFe_{12-x}O_{19}$ (x = 0-0.6)

The relative intensities of the peaks have slight variation, but peak position remains unchanged with substitution (Fig. 8.3). Hexaferrite formation has been confirmed by the presence of two prominent peaks that arise near 430 cm^{-1} and 580 cm^{-1}. The stretching vibrations of metal-oxygen bond with ν_1 and ν_2 mode are the reason for these peaks. The bands near 420-480 cm^{-1}(ν_1 mode) and 550-590 cm^{-1}(ν_2 mode) attribute to the vibration of the ferric crystallographic site (octahedral and tetrahedral respectively). The FTIR spectra for x = 0.2 show relatively more prominent peaks. This may be due to the substituted cations at the ferric sites accompanying strong interactions than other samples. No nitrate ions appear in the samples (near 1300 cm^{-1}) pointing the redox reaction completion, in which citric acid play a role as redundant and nitrate ions play role as an oxidant [84].

Band near 1500 cm^{-1} appear in sample $x \geq 0.3$ due to N-H band of ammonia. No band near 2900 cm^{-1} except for sample x=0.1 occurs, indicating the absence of moisture absorbed by the sample [85]. The presence of band at ~3650 cm^{-1} in the sample having x=0.4 may be because of O-H of ammonia solution that remain unreacted.

The molecular vibrations of the BGCM have been investigated using Bruker Multiram FT-Raman spectrometer. Every compound possesses a unique Raman spectrum and provide detailed information about the crystal lattice and molecular vibrations for identification of material. This technique is sensitive to the change in chemical environment and composition. FT-Raman has been recorded in the range from 100 cm^{-1} to 750 cm^{-1} for x = 0.0 and x = 0.3 (Fig. 8.4).

Barium hexaferrite is a hetero-structure having metal oxygen bonds. These bonds are responsible for the absorption of certain energy and peaks arise at that energy. The prominent peaks are observed at about 175 cm^{-1}, 290 cm^{-1}, 333 cm^{-1}, 410 cm^{-1}, 525 cm^{-1}, 612 cm^{-1}, 681 cm^{-1} and 725 cm^{-1}. These peaks are favouring the presence of magneto-plumbite structure. Both samples are showing magneto-crystalline structure. Barium hexaferrite can exhibit 42 Raman active sites ($11\ A_{1g} + 14\ E_{1g} + 17\ E_{2g}$). Such number of sites can enhances the overlapping of peaks and hence the increase of broadening. Internal stress origination due to substitution can also contribute to the broadening. So, the large number of small peaks can be observed, but some peaks get overlapped

and get disappeared. The presence of various vibrational modes and their corresponding peaks has been given in Table 8.2. The appearance of peak at 290 cm^{-1} may ascribe to the impurities present in the sample. In hexagonal structure, 2b is a bipyramidal site (FeO_5) and has

higher co-ordination number as compared to the tetrahedral. So, the band associated with this site lies in the low frequency range (681 cm^{-1}) than the tetrahedral representing band frequency (725 cm^{-1}). Same behaviour can be noticed in case of octahedral [89, 103, 104].

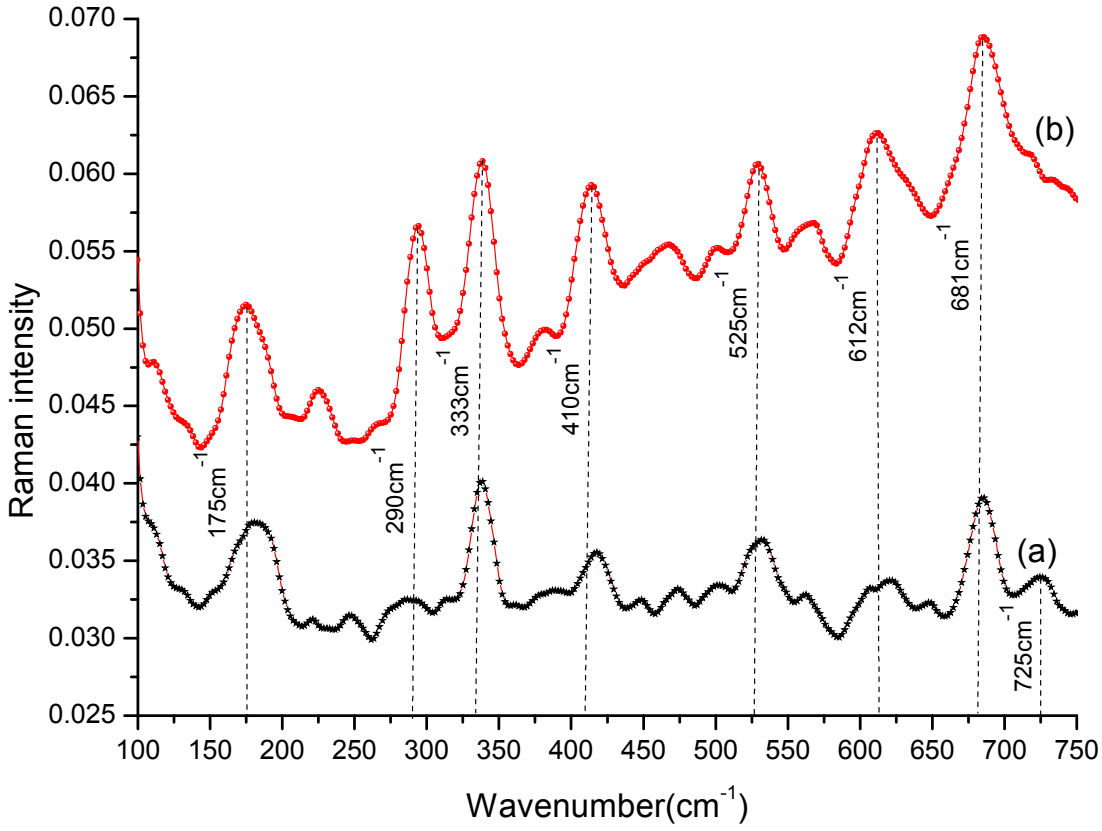

Fig 8.4: FT-Raman spectra for (a) $BaFe_{12}O_{19}$ (b) $Ba_{0.7}Gd_{0.3}Fe_{11.7}Co_{0.3}O_{19}$ taken at room temperature

Table 8.2: Vibrational modes assignment for (a) $BaFe_{12}O_{19}$ (b) $Ba_{0.7}Gd_{0.3}Fe_{11.7}Co_{0.3}O_{19}$ calcined at 900 °C

S. No.	Wavenumber (cm^{-1})	Vibrational mode	Reference (cm^{-1})	Assignments
1	175	E_{1g}	173	S Block
2	290	E_{1g}	285	S Block
3	333	E_{2g}	335	S Block

4	410	A_{1g}	409	Octahedral site12k
5	525	E_{1g}	527	Octahedral 12k and 2a
6	612	A_{1g}	618	Octahedral site $4f_2$
7	681	A_{1g}	684	Bipyramidal site 2b
8	725	A_{1g}	722	Tetrahedral site $4f_1$

The information about surface features, shape, alignment and porosity of nano sized hexaferrite have been investigated using transmission electron microscope (TEM), atomic force microscope (AFM) and scanning electron microscope (SEM) at room temperature. Transmission electron microscope (TEM) images of samples have been recorded using JEOL JEM 2100, Japan instrument (Fig. 8.5 (a to f)). Samples for TEM analysis was dispersed in isopropanol. A flawless, cutting edge micrographs of hexagonal structure can be seen in TEM images. The fringes appear in samples represents the crystalline structure of prepared material.

Surface features have been taken from SEM (Jeol 6390LV) at an operating voltage of 20 kV (Fig. 8.6 (a and b)). SEM micrographs show that the non-uniform hexaferrite grains have uneven distribution. The presence of clusters and porous microstructure in some parts of SEM images can be seen. In SEM, the crystallite size looks bigger than estimated in XRD study, but TEM and AFM micrographs show that crystallite size is in range 20-65 nm. SEM micrographs shows porous material, for which the evolution of gases is responsible entirely. AFM (Bruker Dimension Icon) has been used to analyse the morphology of the sample by dispersing the samples in methanol (Fig. 8.6 c). A hexagonal structure of hexaferrite and a square shape of hematite can be clearly seen in AFM micrograph [90].

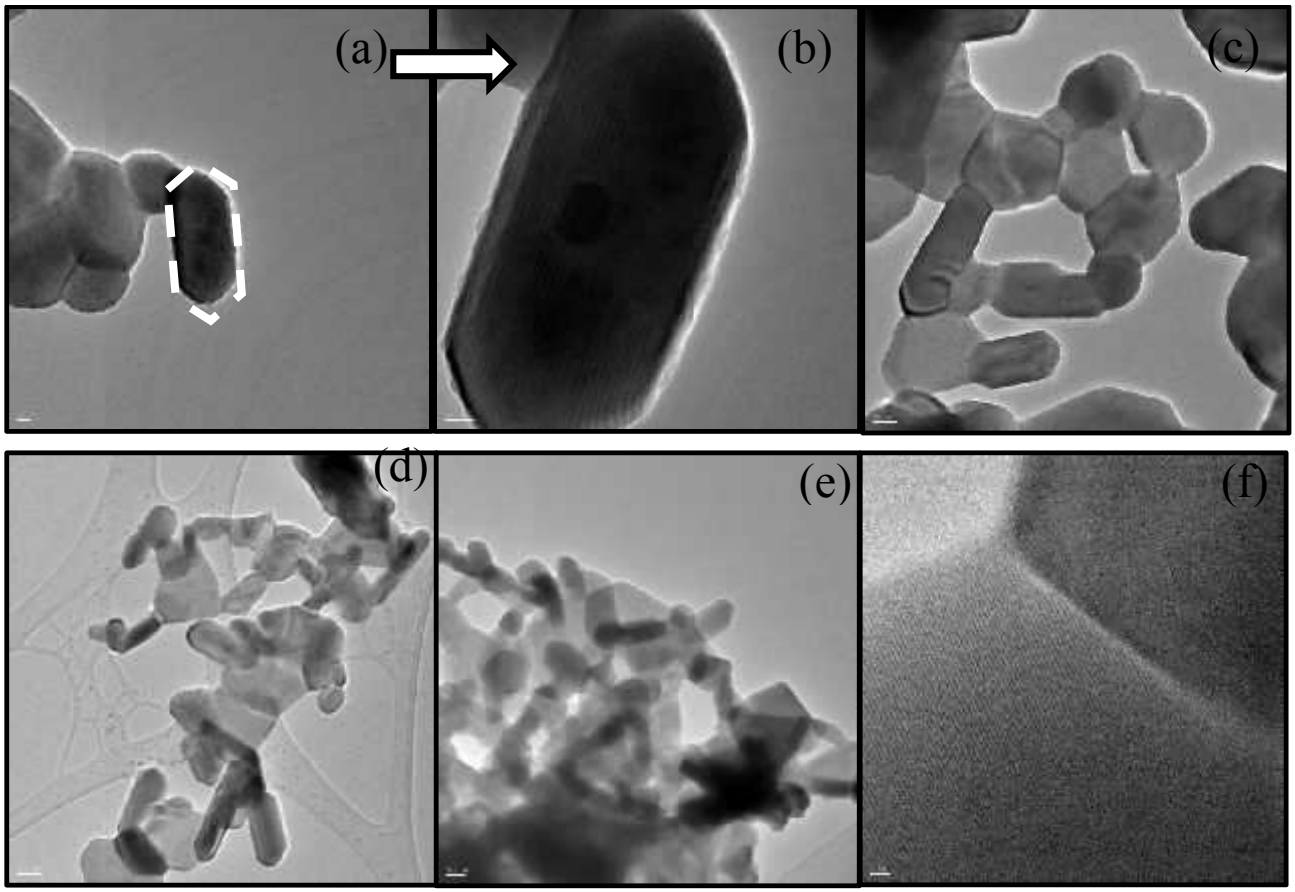

Fig 8.5 Transmission electron microscopy images $Ba_{1-x}Gd_xCo_xFe_{12-x}O_{19}$ (BGCM) powders for (a and b) x=0.4 and (c) x=0.5 (d) and (e) x=0.2 (f) x=0.1

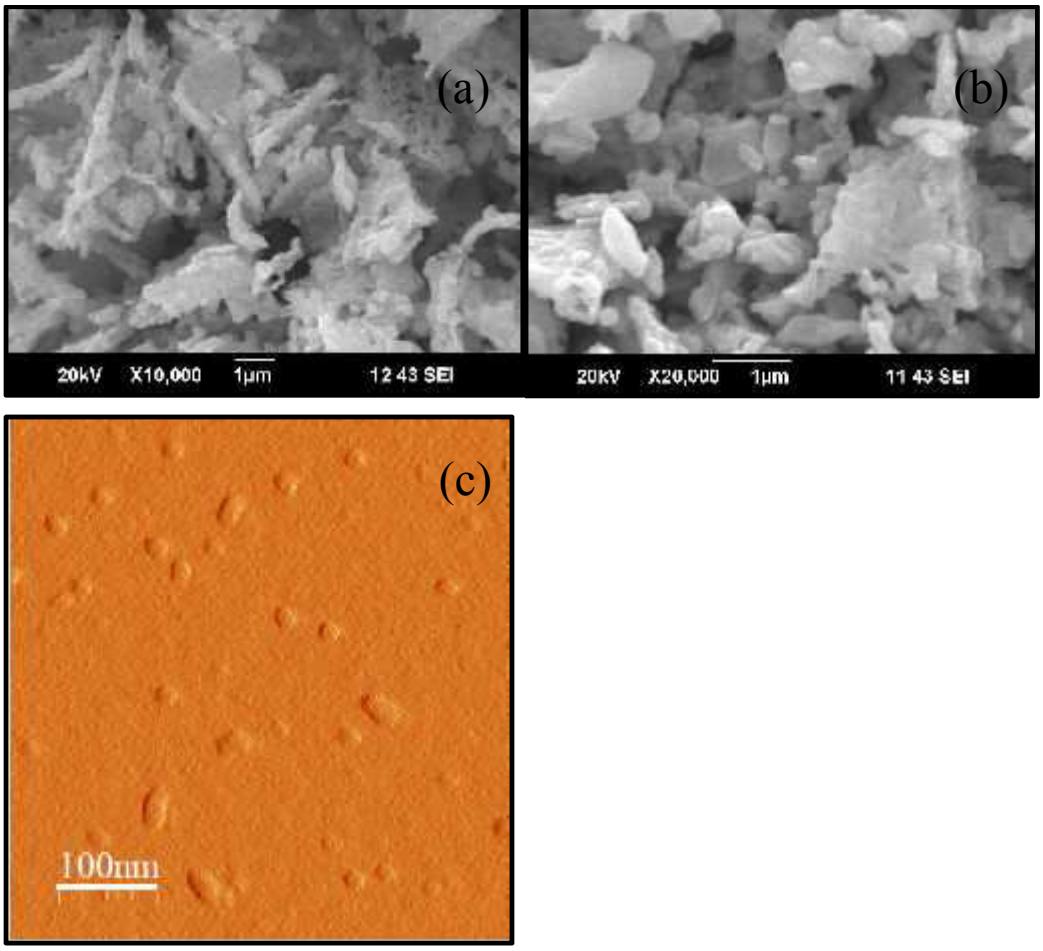

Fig 8.6: SEM and AFM micrographs of $Ba_{1-x}Gd_xCo_xFe_{12-x}O_{19}$ for (a) x = 0.1, (b) x = 0.3 and (c) x = 0.3

ESR measurements were performed at room temperature using an X-band JEOL JES- ME spectrometer under following experimental conditions: magnetic field sweep rate of 50 mT/min, modulation width of 0.35 mT, modulation frequency of 100 kHz, microwave power of ~ 10 mW (9.5 GHz) and magnetic field range from 1000 gauss to 9000 gauss.

Interaction of unpaired electrons with its environment influence the shape of ESR spectral line. The intensity for the substituted sample is high than the pure hexaferrite sample. The unpaired electron not only interact with the external magnetic field but also with magnetic field in their neighbourhood, this can effect the intensity of the ESR signal. The ferrimagnetic resonance exhibited by Fe^{3+} cations at different interstitial sites couple anti-ferromagnetically due to a super-exchange interaction and causes the symmetric resonance absorption and line width ΔH in the

hexaferrite (Fig. 8.7). The samples are not showing any change in line width with the substitution of Gd-Co. There are two resonance parts in the EPR spectra.

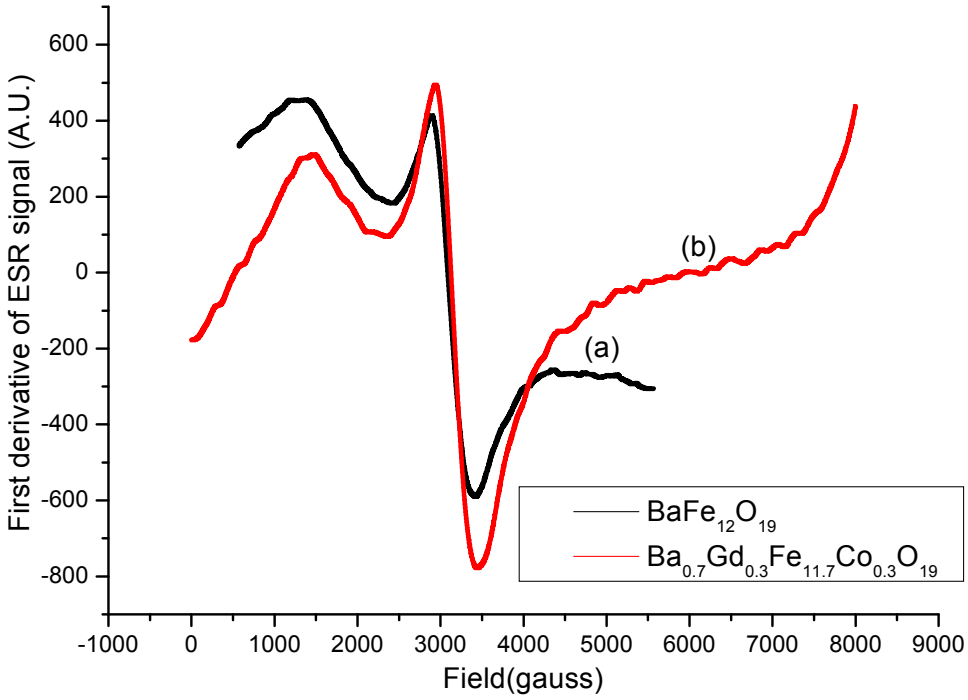

Fig 8.7: ESR spectra for (a) $BaFe_{12}O_{19}$ (b) $Ba_{0.7}Gd_{0.3}Fe_{11.7}Co_{0.3}O_{19}$ taken at room temperature in X band.

Table 8.3: ESR parameters of $BaFe_{12}O_{19}$ and $Ba_{0.7}Gd_{0.3}Fe_{11.7}Co_{0.3}O_{19}$ taken at room temperature in X band.

Sample	ΔH(gauss)	g factor	T_2 (s^{-1})
$BaFe_{12}O_{19}$	528	2.26	5.499×10^{-11}
$Ba_{0.7}Gd_{0.3}Fe_{11.7}Co_{0.3}O_{19}$	510	2.24	5.744×10^{-11}

The first part is called low field resonance near g = 4.49 which is a characteristic of tetragonal Fe^{3+} ions in a low field having magnetically isolated high spins (S = 5/2) and the other part is a much broader resonance at high field near H = 3000 Gauss with g = 2.26 (Table 8.3), mainly contributed by the Fe^{3+} ions present at octahedral sites. The EPR intensity increases with Co^{2+} substitution. The less intensity of undoped sample may be due to a slow down in spin

reorientation transition [106]. The interaction of the spins of electrons with adjacent atoms is related to the relaxation time (T) and can be calculated from the value of (ΔH) by using following relations: $\frac{1}{T} = \frac{g\beta\Delta H_{1/2}}{\hbar}$, $\Delta H_{1/2} = \sqrt{3}\Delta H$

where β is Bohr Magneton (9.274 x 10^{-21} erg G^{-1}), $\Delta H_{1/2}$ is half of peak to peak width, $\hbar$= 1.054 x 10^{-34} J.s.. The relaxation time of the ESR signal was directly related to the interactions of the spins with their environment and to their motion.

The band gap study has been carried out using UV-Vis-NIR (Model: Varian Carry 5000 at room temperature with 0.2 nm resolution). UV–Vis-NIR has been used to investigate the optical properties of BGCM in the optical region (200-800 nm) using absorption spectra. From the spectrum the absorbed band gap energy has been calculated by using following relation [50]:

$$\alpha = \frac{A(h\nu - E_g)^{1/2}}{h\nu}$$

where α is absorption coefficient, A is a characteristic parameter of transition which depends on the value of n that can have values 1/2, 2, 3/2 and 3 for allowed direct, allowed indirect, forbidden direct and forbidden indirect transitions, respectively. E_g denotes the optical band gap energy, h is Planck constant and ν is incident photon's frequency. Figure 8.8 shows the spectra for energy band gap of pure and substituted BGCM.

Table 8.4: Band gap variation with substitution in $Ba_{1-x}Gd_xCo_xFe_{12-x}O_{19}$ (x = 0-0.6)

S. No.	x	Band gap (eV)
1	0.0	3.99
2	0.1	4.07
3	0.2	4.13
4	0.3	4.03
5	0.4	4.13
6	0.5	4.12
7	0.6	4.28

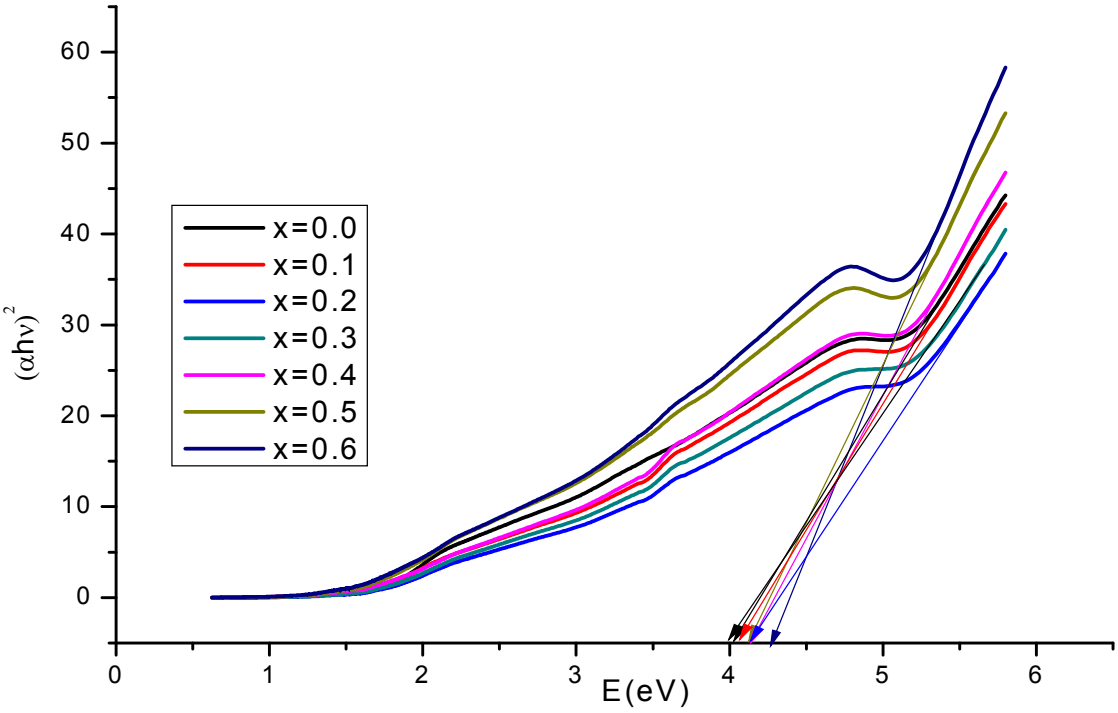

Fig 8.8: Energy band spectra for $Ba_{1-x}Gd_xCo_xFe_{12-x}O_{19}$ (x = 0-0.6) calcined at 900ºC

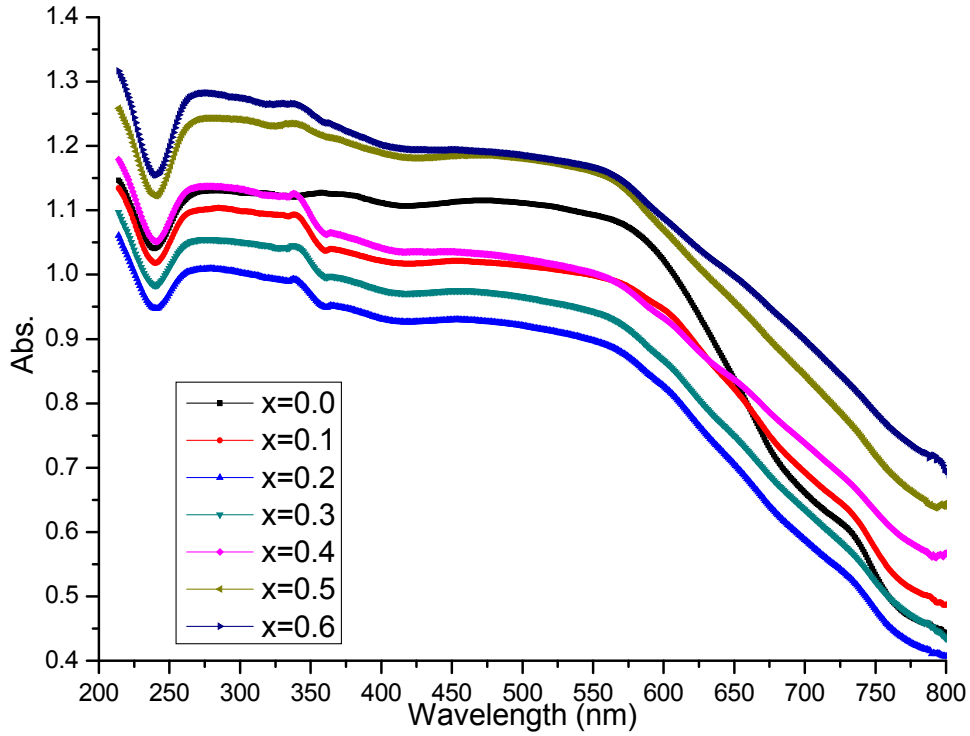

Fig 8.9: Absorption curves for $Ba_{1-x}Gd_xCo_xFe_{12-x}O_{19}$ (x = 0-0.6)

The plotted graphs are showing direct allowed band gap. So the value of n = 1/2 has been used for calculation. The value of direct band gap energy can be determined from extrapolation of a liner portion of the plots. The band gap of pure barium hexaferrite has been obtained 3.99 eV (Table 8.4). It has been concluded that the band gap energy increases with increase in substitution concentration. BaM shows low value of band gap than BGCM. The band gap of BGCM is higher than barium hexaferrite (3.18eV) and barium hexaferrite thin films (2.32eV) as reported elsewhere [73, 74]. The binding energy of RE-O is very high so incorporation of RE^{3+} increases the band gap energy up to some extent. Quantum confinement plays an important role in the increase of the band gap. Crystallite size also affects the band gap energy. The smaller the size the more discrete energy levels are formed leads to increase in band gap energy. From UV-NIR absorption spectra (Fig. 8.9), it can be concluded that the absorption region for hexaferrites is ~ 200-600 nm which is much wide and can be used as an effective absorber.

Dielectric analysis has been performed with an LCR meter (Model: 6440B) at 20 Hz- 3 MHz at temperature 8 ˚C. The capacitance of calcined BGCM has been recorded on LCR meter using silver metal powder coated palettes (with 8 tonne pressure). Dielectric constant has been calculated from parallel plate capacitor equation [70]:

$$K = \frac{Cd}{\varepsilon_0 A}$$

where K is dielectric constant, C is the capacitance of the palette, d is thickness of sample palette and A is cross sectional area and ε_o is the permittivity of free space (8.85×10^{-12} F/m).

A normal behaviour of ferrite has been shown by BGCM (Fig. 8.10) towards frequency that is dielectric constant (K) is high for low frequency, but decreases when frequency tends to increase and then becomes constant. This behaviour can be correspond to the space charge polarization. The two theories are working behind this phenomena that are Koop's phenomenological and Maxwell Wagner theory. According to their theory, there may be a change in valency of cations present because of electron exchange between Fe^{3+} and Fe^{2+} and resulting in displacement of the ionic charges that causes polarization. The oxygen ions having loosely bound electrons and contribute to the polarization by aligning themselves along with applied field. Hetero-structure of hexaferrite consists of the conducting grains and grains are separated by very

thin but highly resistive grain boundaries. The dielectric constant depends on various factors like crystallite size, cations present, calcination conditions, chemical composition etc. [71].

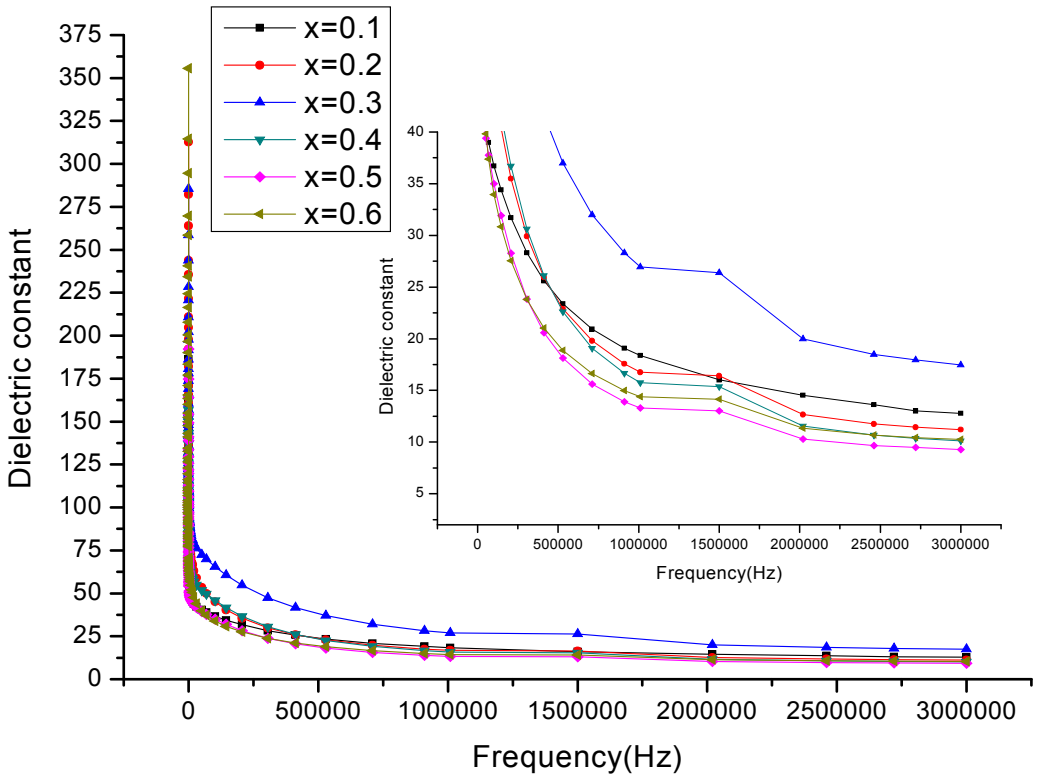

Fig. 8.10: Variation of dielectric constant with frequency

The grain boundaries offers high resistance when the charge carriers align themselves at the interface of grains and causing polarization. The electrons have been displaced by applied field and causes polarization, but when half of alternating field becomes more than hopping time, the displacement does not happen. So the dielectric constant shows a decrease in value at high frequency [86, 107]. Due to of low eddy currents and high dielectric constant, synthesized material can play a significant role in electronics market as a radiation absorbing material, electrical fillers, high frequency component etc. Decrease in dielectric constant with substitution explanation Dielectric loss (Fig. 8.11) can be calculated by using the expression [72]:

$$\varepsilon'' = \varepsilon' \tan \delta$$

where ε' is dielectric constant and ε'' is a dielectric loss factor. Dielectric losses are also high at low frequency.

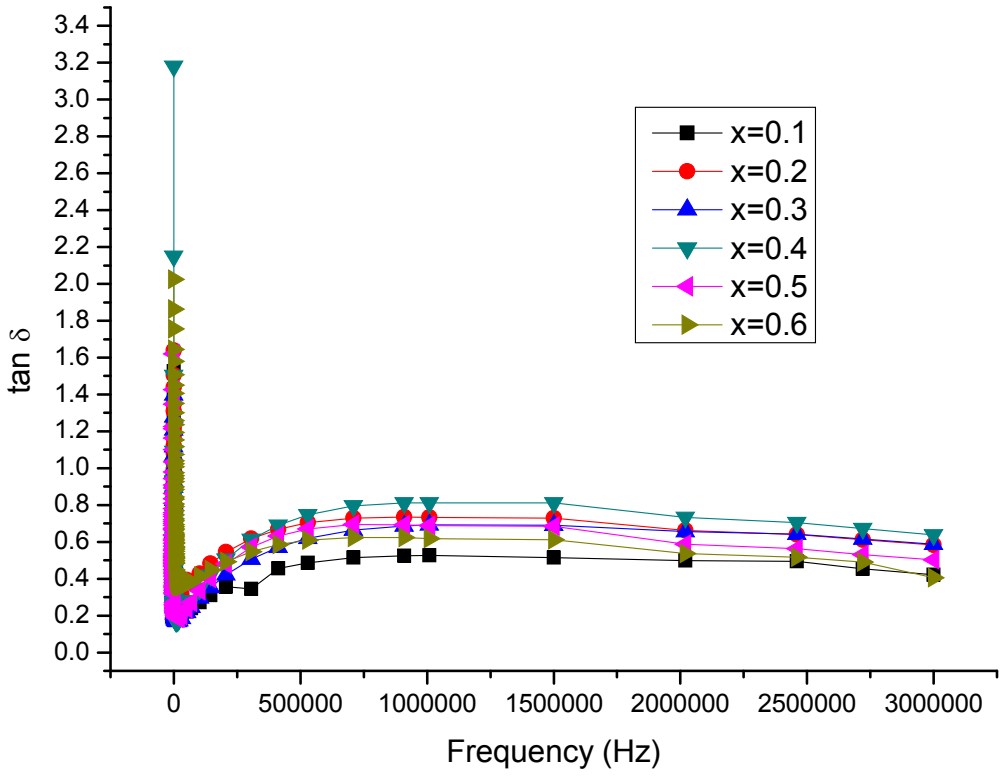

Fig.8.11: Plot of tangent loss with frequency for $Ba_{1-x}Gd_xCo_xFe_{12-x}O_{19}$ (x = 0-0.6)

Hopping is the reason for loss tangent behavior. Dielectric loss tanδ decreases with increase in frequency (Fig. 8.11). Maximum of loss tangent may be observed when the hopping is nearly equal to that of the externally applied electric field. After the maxima, hopping time becomes more than the applied signal so cause a decrease in loss tangent.

I-V characteristic have been plotted using Keithley - 2612 A system source meter for Gd-Co substituted barium hexaferrite in -10 to 10 Volts (Fig. 8.12). Almost linear behavior can be seen from characteristics. It has been observed that resistance is not depending on substitution of Gd-Co. The resistance of the samples is in the 10^9 Ohm range. The small current established in the material is solely because of conduction of single electron between $Fe^{2+} \rightarrow Fe^{3+} + e^-$. Hexaferrite are highly resistive material. Furthermore the Co^{2+} ions create a hindrance for more conduction by decreasing ferric ions. Owing to high resistance and low eddy currents, prepared material can be utilized in high frequency application, resistors, radiation absorbance material.

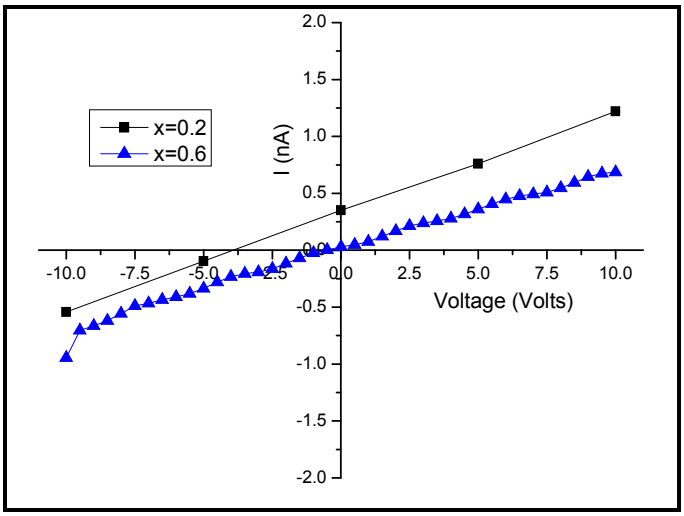

Fig 8.12. Current and voltage characteristics of $Ba_{1-x}Gd_xCo_xFe_{12-x}O_{19}$ (x = 0.2 and 0.6)

Polarization loops has been illustrated in Fig 8.13 (a) to (d) for $Ba_{1-x}Gd_xCo_xFe_{12-x}O_{19}$. The samples were palletized in circular form having thickness 2 mm. For compensation, the 4.7 μF capacitor has been used. The shape of the hysteresis loop depicts the ferroelectric nature of the specimen under study. In our case soft hysteresis behavior with unsaturated polarization loops with lower coercivity values were obtained for the synthesized samples. Normally a single crystal or a specimen with 100% c-oriented grains exhibits nearly a square loop with high remanent polarization. Lower remanent polarization arise on account of random orientation of crystallites that influences the reversal of domains. Coercive field occurs due to the growth of ferroelectric domains causes reversal of polarization. But owing to low growth domains, coercivity attains low value. The lower resistance offers by the off-centering of Fe ions impedes the saturation polarization to raise its level [108].

Lacking in convex and concave portion, obtained loops are not consistent with the standard ferroelectric loops due to low resistance but the samples shows polarization behavior [109]

A saturation is missing in the hysteresis loops because the presence of electron hopping between Fe^{3+} and Fe^{2+} ions offers low resistance to saturate the sample. The model of the hexaferrite structure is shown in Fig. 8.14 having space group P63/mmc with nine atomic layers. The arrows indicating the spin orientation of Fe ions. Structure of hexaferrite possesses distorted FeO_6 octahedron in a unit cell.

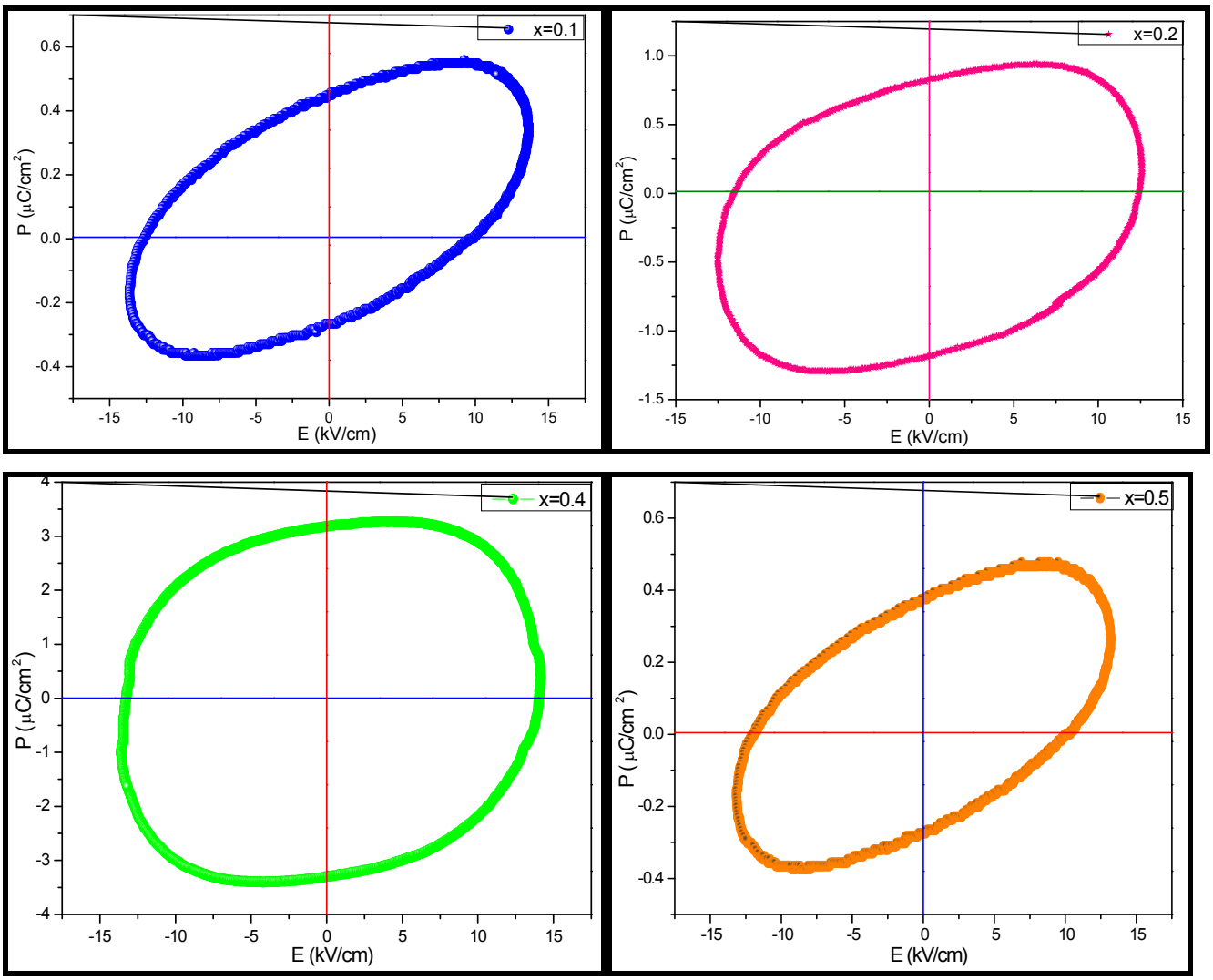

Fig 8.13: Ferroelectric loops for gadolinium and cobalt substituted barium hexaferrite $Ba_{1-x}Gd_xCo_xFe_{12-x}O_{19}$ (a) x=0.1, (b) x=0.2, (c) x= 0.4 and (d) x=0.5

The similar octahedron can be found in perovskite structure compounds which are ferroelectric in nature; ABO_3, where A signifies the cations at the corner, B cations placed at the center surrounds by 6 oxygen ions (BO_6) making octahedron (ex. $BaTiO_3$, $LiNbO_3$ or $PbTiO_3$). Normal octahedron composed of ferric ions at center of oxygen octahedron, but below Curie temperature (as the measurement of hysteresis behavior taken at room temperature), a distortion occurs in lower symmetry phase forcing Fe ions to shift off center along b axis and causing shift off 2 oxygen ions lead to the deformation of O-Fe-O bond. This deformation in octahedron is responsible for the origin of a dipole moment that creates polarization. There are enough octahedron present in the

structure to induce the electric polarization. The presence of tetrahedral and bi-pyramidal have no share in ferroelectric response of hexaferrite [110].

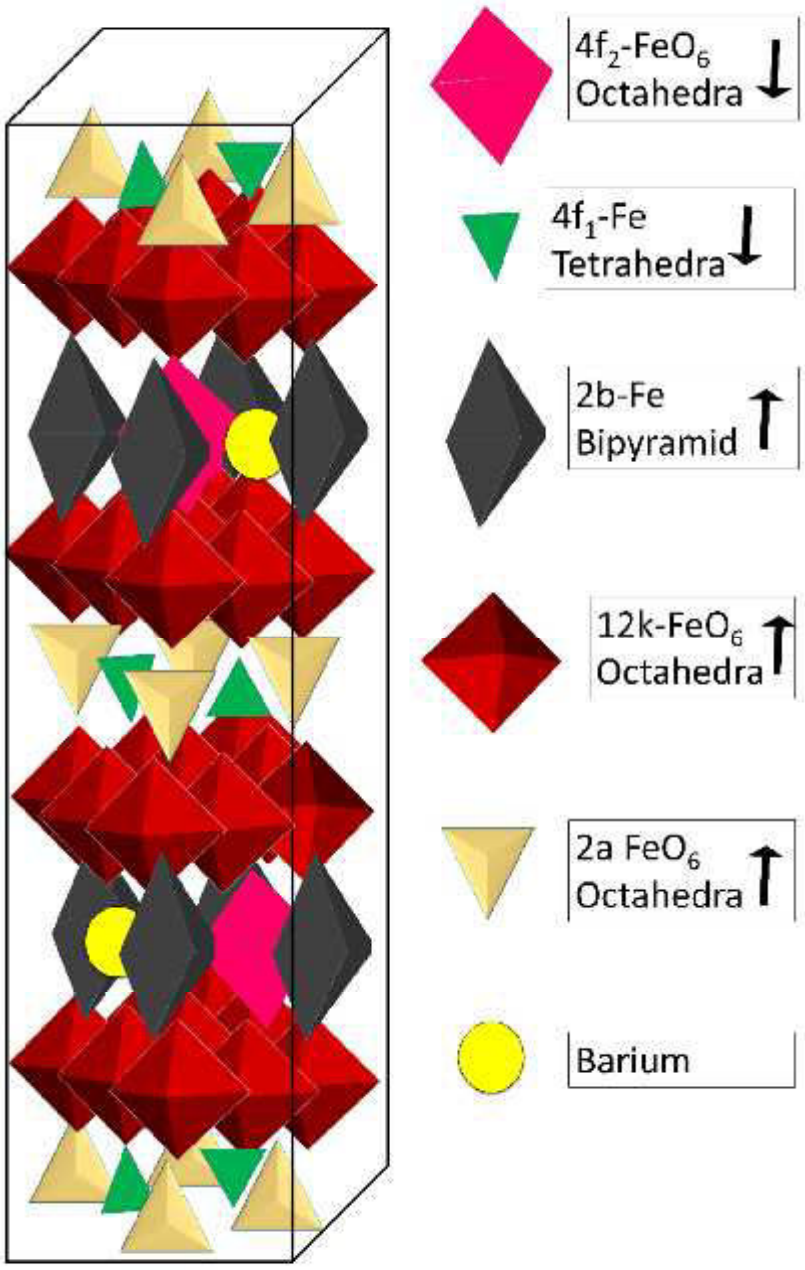

Fig 8.14. A block diagram of hexaferrite crystal structure with illustration of octahedron, tetrahedron and bipyramidal structures.

Table 8.5: Summary of Coercivity (H_C), saturation Magnetization (M_S), Retentivity (M_R), Squareness Ratio (SR) and Anisotropy constant (K) and energy barrier with substitution for $Ba_{1-x}Gd_xCo_xFe_{12-x}O_{19}$ (x = 0-0.6)

x	H_C (G)	M_S (emu/g)	M_R (emu/g)	SR(M_R /M_S)	K(HA^2/kg)	E_A*10^3
0.0	5427	92.53	52.42	0.57	25.23	17.62
0.1	3875	35.57	21.37	0.60	6.92	5.01
0.2	4283	47.31	27.26	0.58	10.18	7.42
0.3	4053	41.42	24.79	0.60	8.43	5.90
0.4	3875	38.50	22.38	0.58	7.49	5.14
0.5	3191	22.37	12.66	0.57	3.59	2.44
0.6	2825	29.68	16.70	0.56	4.21	2.86

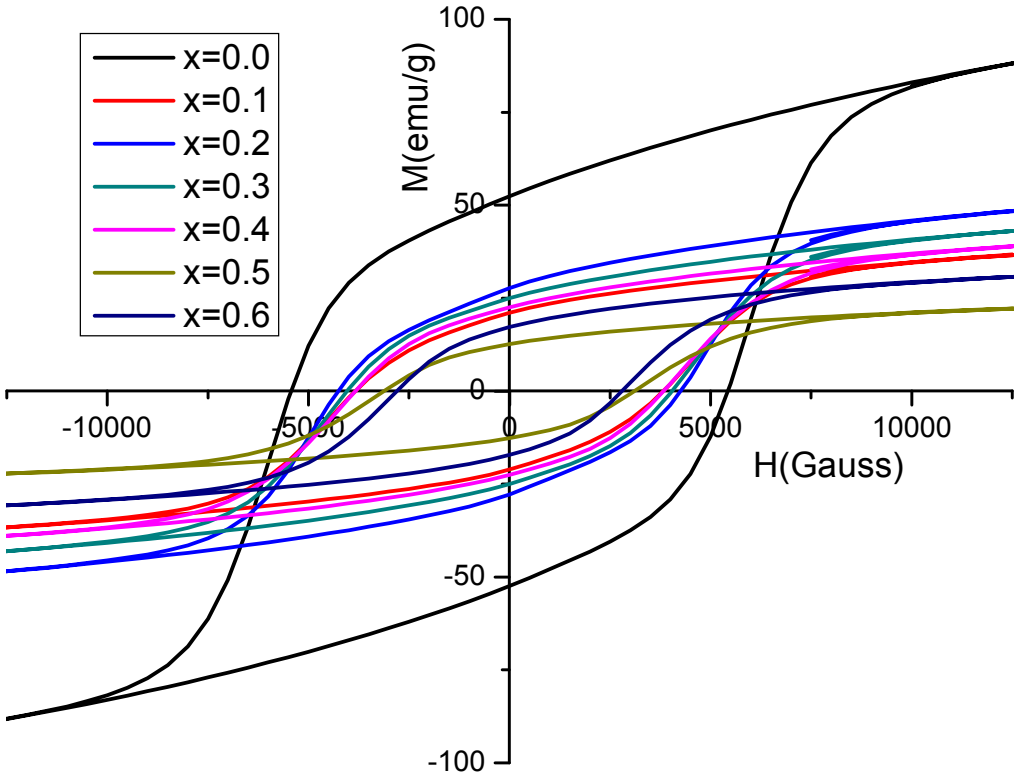

Fig. 8.15: Hysteresis loop for $Ba_{1-x}Gd_xCo_xFe_{12-x}O_{19}$ (x = 0-0.6) calcined at 900 ˚C.

Magnetic properties have been investigated using vibrating sample magnetometer (VSM) (Lakeshore 7410) at room temperature. The magnetic properties like coercivity, saturation magnetization and retentivity has been evaluated from the hysteresis curve (Fig. 8.15) and summarize in Table 8.5. The magnetic properties of hexaferrite strongly depend on the routes of synthesis, site occupation, ionic radii, substituted cations and density.

Effect of substitution of Gd^{3+} and Co^{2+} has been seen on saturation magnetization and coercivity. Saturation magnetization (M_S) value for pure barium hexaferrite is 92.53 emu/g and M_S value for pure is more than substituted samples. M_S depends on the magnetic moment of particles. The lowest value for M_S is 22.37 emu/g for x = 0.5. Saturation magnetization continuously decreases with increase in Gd-Co substitution. It may be because of substitution of Co^{2+} (3 μ_B), having a smaller magnetic moment than Fe^{3+} (5 μ_B) that leads to the decrease in net exchange interaction strength, which causes a reduction in magnetization. Magnetization has also gotten effected because of the presence of impurities in samples as discussed in XRD analysis. Hematite is a non-magnetic impurity that affects the magnetic parameters of the samples. The substituted samples show less M_S value than that of BaM. The presence of rare earth metal having canted spins which promotes the non-collinear magnetic order and hence reduces the net magnetization. The squareness ratio is in range 0.56- 0.60. So, a single magnetic domains has been produced.

Coercivity values have been continuously decreased with substitution. The plausible reason for decrease in coercivity may be the energy barrier for spin reversal, porosity, sample degradation and anisotropy constant. The coercivity and anisotropy constant are related with each other by relation, $H_C = \frac{2\mu_0 K}{M_S}$, where μ_o is the universal constant of permeability in free space and is equal to $4\pi \times 10^{-7}$ H/m and K is anisotropy constant. Direct dependence of coercivity on energy barrier affects its value. An energy is required for reversal of spins that is called energy barrier and can be expressed as $E_A = KV \sin^2\theta$. Among substituted samples, x = 0.0 has highest energy barrier and hence highest coercivity. It has been observed that porosity also effects the coercivity. Pure sample (barium hexaferrite) has highest coercivity because of high porosity value (74.80%).

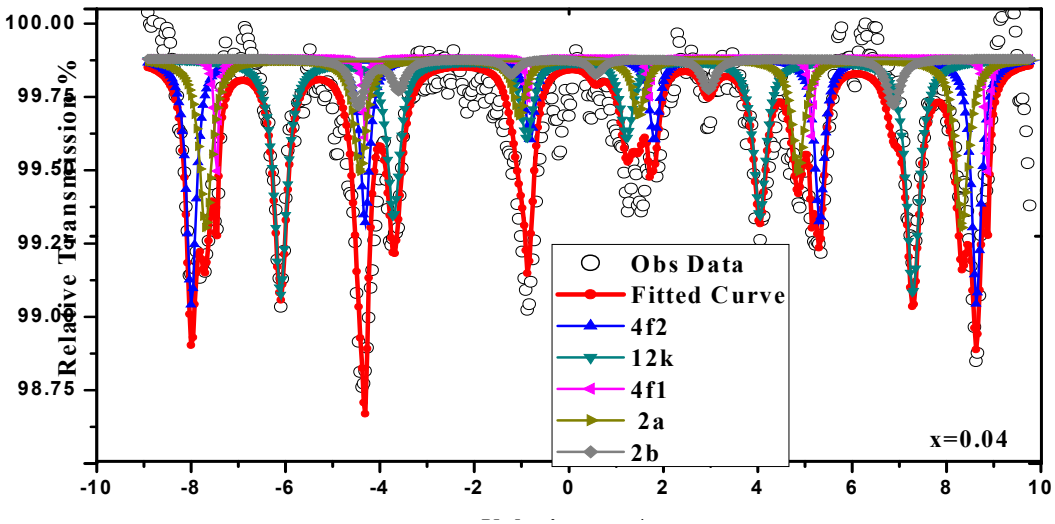

Fig 8.16: ^{57}Fe relative transmission Mossbauer spectra for $Ba_{1-x}Gd_xCo_xFe_{12-x}O_{19}$ (x = 0.4) recorded at room temperature. Sextet corresponding to presence of Ferric ions at different sites and experimental data (in symbol) along with fitted data (red continuous line)

With substitution of Gd^{3+}, the valency state of Fe^{3+} changes to Fe^{2+}. For charge neutrality, the high spin Fe^{3+} ($3d^5$) changed in low spin Fe^{2+} ($3d^4$) causes the occurrence of spin canting and abundance of Fe^{2+} ions causes distortion of atomic arrangement and decrease in coercivity. Also the substitution of RE^{3+} causes perturbation in the lattice and dilution of the strength of the Fe-O bond and resulting in reduction of the magnetic parameters.

Mossbauer Spectroscopy analysis has been carried out at room temperature (Fig. 8.16) for study of ions distribution in sample structure with conventional ^{57}Fe γ-ray source at a constant acceleration mode on Fatcom Mossbauer instrument model.

The obtained experimental data has been mathematically processed and fitted with MossWin 4.0 version software. A resolved and defined Mossbauer spectrum after fitting exhibits the magnetically splitted Zeeman sextet relative to different five crystallographic position of ferric cations namely 12k, $4f_2$, $4f_1$, 2a and 2b, this splitted spectrum confirms the presence of hexagonal structure. The calculated parameters are showing variation from reported parameters [24, 111]. The low value of H_{ef} for 2b is due to lattice expansion and substitution effects and grain growth. Hyperfine field (H_{ef}) gives information about interaction between nucleus and surrounding

Table 8.6: The Isomer Shift, Quadruple splitting, Hyperfine field, Area and Line width obtained by fitting curve for $Ba_{1-x}Gd_xCo_xFe_{12-x}O_{19}$ (x = 0.4)

Sub-spectrum / Hyperfine Parameter	12k	$4f_2$	$4f_1$	2a	2b
Isomer shift (mm/s) [I.S.]	0.37	0.40	0.25	0.55	0.43
Isomer shift (mm/s)*	0.37	0.39	0.27	0.38	0.29
Hyperfine field (T) [H_{ef}]	41.61	51.66	49.78	50.73	35.21
Hyperfine field (T)*	41.9	52.5	49.7	51.3	40.7
Q splitting (mm/s) [Q.S.]	0.42	-0.17	0.10	0.28	1.52
Q splitting (mm/s)*	0.42	0.16	0.23	0.09	2.17
Area (%)	35.12	27.38	24.66	5.59	7.25
Theoretical Occupation (%)	50	16.66	16.66	8.33	8.33
Line width (mm/s)	0.32	0.24	0.31	0.10	0.33
Line width (mm/s)*	0.34	0.28	0.37	0.24	0.28

*Data has been taken from [24]. Reference data that has been taken is of pure hexaferrite. magnetic field [112]. The drop in H_{ef} for 2b can be attribute to the coupling of $4f_2$ with 2b and 12k because substitution occurs mainly at $4f_1$ and $4f_2$ (at spin down site) causes fall in H_{ef} of 2b. With substitution, the exchange interaction between lattices has been decreased. The decrease in value of H_{ef} and increase in Q. splitting (Q.S.) value at 2a indicates that the substitution of Gd^{3+} at place of Ba^{2+} has induced a perturbation of symmetry and increase the electron vicinity of the site causes variation in these parameters. [81]. As impurity presence is confirmed in XRD data, the impurity peaks does not appear in fitted data, it may get overlapped with peaks of 2b and cause low resolution of impurity peak [113]. Isomeric shift (I.S.) depends on s-electron density and the shielding effect of p, d and f electrons. Isomer shift for Fe^{3+} (S=1/2) varies in range 0.04 - 0.55. All I.S value are in this range [114]. Expression for Isomer shift is given by:

$$I.S. = C\left\{\left|\psi(0)\right|_A^2\right\}\left(R_e^2 - R_g^2\right)$$

The nuclear factor (Re^2-Rg^2, effective nuclear charge radius of excited and ground state) is always negative, but the $|\varphi(0)|_A^2$ factor (electron density difference on nucleus) depends on shielding of electron [76]. Quadruple splitting gives knowledge about symmetry, spin state and oxidation state. The substitution at 2a has also been supported by quadruple splitting. The quadruple splitting value is higher than reported by Belous et.al (Table 8.6) [24]. The substitution causes distortion of the crystal structure. The negative quadruple value refers to the oblate charge distribution of Fe [115]. Ratio of sextet areas in theoretical means is 12k : $4f_1$: $4f_2$: 2a : 2b = 50 : 17 : 17 : 8 : 8, but the experimental data shows the ratio as 35.12 : 27.38 : 24.66: 5.59 : 7.25. From analysis, it can be concluded that the substitution of cations occur at $4f_1$ and $4f_2$ (spin down). The substitution of Co^{2+} forced Fe cations to shift towards octahedral and tetrahedral site. Line broadening is due to structural disorder. Intensities of peaks reflects the relative amount of Fe ions in each sub lattice but intensity also depends on phase and orientation of crystal in direction of γ rays [116]. Substitution of non-magnetic or ion that is less magnetic than host cations produces variation in local magnetic field. This variation effects value of line broadening [13]

Conclusion

Gd-Co substituted barium hexaferrite has been successfully synthesized using a typical modified Pechini sol-gel method. For mass production, the employed method is convenient for use and feasible on economic basis. Microstructural analysis (XRD, SEM, TEM and AFM) confirms the formation of hexaferrite phase with non-homogenous surface. TGA study shows the formation temperature of 680 °C for hexaferrite phase of BGCM. Samples are showing normal ferrite dielectric behaviour. UV – Vis - NIR reveals that the band gap of as prepared samples increases with substitution. VSM analysis shows that coercivity and saturation magnetization depend on substitution. The prepared material can be used as a recording media because of high surface area, high coercivity and saturation magnetization (>2500 Oe). I-V characteristics are showing linear behaviour. Ferroelectric behaviour is not consistent with the standard ferroelectric hysteresis loops, but the polarization is getting induced in the samples. Mossbauer study indicates that the substitution occurs at spin down sites.

CHAPTER-10

RADIATION LOSSES IN MICROWAVE REGION (K_U AND K BAND = 12.4 – 26.5 GHZ) BY MAGNETOELECTRIC POLYPYRROLE NANO-COMPOSITE

Abstract

A nanocomposite of barium hexaferrite and barium titanate embedded in a polymer has been synthesized via emulsion polymerization for the study of radiation absorbance. It has been found that maximum radiation loss occur at 24.40 GHz (-14.66 dB) frequency owing to the combined effect of composition of conducting polymer and suitable dielectric and magnetic material. Prepared material is suitable for radiation losses. Micro structural study reveals that prepared composite comprises of all the phases of present compound. Benzene ring absorption band (at 1183 cm^{-1}) in FT-IR spectra illustrate the presence of polymer. Surface morphology reveals that the array of particles encapsulated by the polymer.

10. 1. Introduction

The intensive use of wireless systems in microwave region with advancement of communication systems has originate the electromagnetic interference and environmental pollution and become hazardous for biological tissues. The radiation absorbing material can help in reducing the unwanted electromagnetic signals. Earlier, magnetic material, metal flakes, carbon nanostructures are used as absorbent and extensively studied for the same property, but the bulk size could not meet the technical requirement like easy synthesis, broad bandwidth, impedance matching. With advancement in nano science, the material varies its properties with size at nano level. The magnetic material tends to decrease their permeability at Gigahertz range frequency, so a conjugated polymer can be used to damp the eddy currents. Absorption in ferrites depends on the magnetic resonance phenomena because of the anisotropy field. Conducting polymer nano-composites have been a used in so many applications since its discovery like Wi-Fi systems, microwave devices, radar absorbing material [103] and other communication systems [104].

Polymer has good stability in air and have good conductivity to promote the charge carrier drift. The magnetic relaxation oscillation of hexaferrite can be effected with the structural disorder like pores, defects etc. The embedding of magnetic material in polymer can induced disorder in structure because of polymer and material matrix. It makes the system more complex resulting in changes of internal magnetic fields. This cause shifting of the resonance frequency. The permeability ($\mu = \mu' + j\mu''$) and permittivity ($\varepsilon = \varepsilon' + j\varepsilon''$) contributes effectively to absorb or dissipate the radiation.

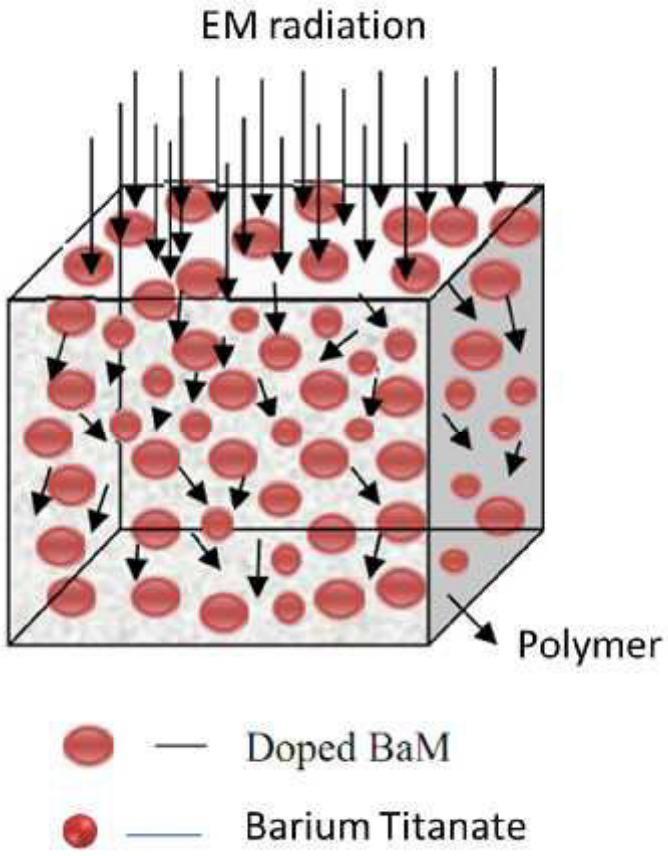

Fig 10. 1: Mechanism for radiation absorbance

Real parts of both parameters contributes to the energy storage and imaginary parts contributes to the losses in a material. From theoretical study for radiation losses, the magnetic loss and dielectric losses combine can absorb the wide frequency range at effective level. So, a composite with magnetic material, dielectric material and a π- conjugated system possessing conducting polymer can absorb the radiation (Fig 10. 1). The pyrrole, a conducting polymer has

catch a much attention because of its high electrical conductivity. [39, 40, 41]. So, the researchers [105, 106-117] has turned their attention towards polymers embedded dielectric and magnetic particles.

So many method are available to develop such composite, but emulsion polymerization that is easy and reliable method has been used in this work and the prepared composite has been studied for structural, magnetic and radiation absorbance properties.

10.2. Experimental procedure

The synthesis of Gd-Co and Nd-Co substituted barium hexaferrite has been carried out via sol gel method using AR grade chemicals. For synthesis of barium titanate, the starting materials used are barium nitrate, TiO_2 and oxalic acid. An aqueous solution of barium nitrate (0.12M) was prepared using distilled water. Required amount (Ba/Ti = 1:1) of TiO_2 powder was poured to the aqueous solution of barium nitrate with constant stirring. To avoid the agglomeration of titanium oxide article, the mixture is ultrasonicated (10 minutes). Oxalic acid (0.4 M) was added to the mixture drop wise with vigorous stirring. Ammonia solution is added to maintain the pH at 6.8. The precipitates are formed and the resultant product was washed repeatedly with distilled water followed by drying at 40 °C for 2 days. The precursor was calcined at 900 ˚C.

The surfactant dodecyl benzene sulfonic acid (DBSA) is used as surfactant. 0.3 M solution of DBSA is added in barium hexaferrite and barium titanate to form an emulsion. The pyrrole is added in solution. For uniform dispersion, the solution was ultrasonicated before and after the addition of pyrrole monomer. Further, an initiator ammonium persulphate has been used that will initiate the polymerization at 2 ˚C. Obtained solution was kept on stirring for 24 hours. So obtained product is filtered with suction pump and demulsify with isopropyl alcohol then washed with distilled water. The samples are placed in an oven and dried at 80 ˚C for 24 h [39].

10. 3. Characterization techniques

Various testing techniques has been employed to study the composite. All those testing techniques are mentioned in Chapter 9.

10. 4. Results and Discussions

10. 4. 1. Phase Identification

The phase identification of the nanocomposites having hexaferrite, barium titanate and polypyrrole has been investigated by well-known non-destructive X-ray powder diffractometer technique in range 20-80^0 and presented in Fig. 10.2.

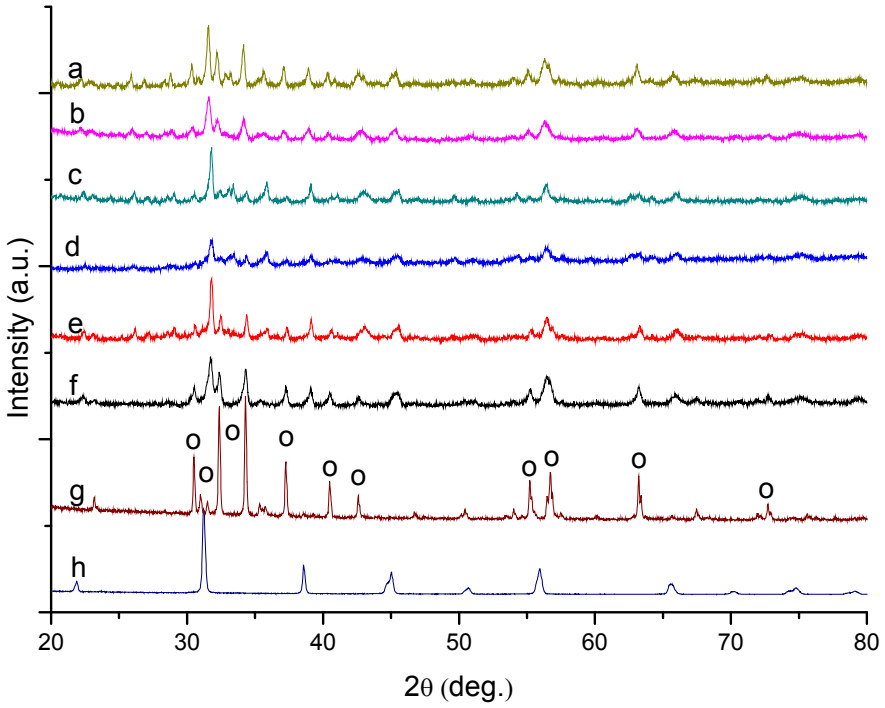

Fig 10. 2: X-ray diffraction pattern for $Ba_{1-x}Gd_xCo_xFe_{12-x}O_{19}$ (or $Ba_{1-y}Nd_yCo_yFe_{12-y}O_{19}$)/$BaTiO_3$/Polypyrrole composite at (a) y = 0.4, (b) y = 0.25, (c) y=0.1, (d) x = 0.5, (e) x=0.2, (f) x=0.0 whereas (g) Pure barium hexaferrite and (h) Pure Barium titanate

All the synthesized samples show crystalline phase. The presence of apparent peaks present (Fig 10.2) at angle 23.006º (006), 30.318º (110), 32.236º (107), 34.214º (114), 56.512º (2011) are for hexaferrite and peaks at 31.730º (110), 45.462º (200), 65.896º (220) representing presence of barium titanate. Slight amorphous peak near between 20 and 23º is for pyrrole. Hence, the structural study proposed the presence of all phases of composite. Sample code that has been used in the present study is presented in table 10.1.

Table 10. 1: Sample code for composite

S. No.	Code
$Ba_{1-y}Nd_yCo_yFe_{12-y}O_{19}/BaTiO_3$/Polypyrrole at y = 0.4	BNPY4
$Ba_{1-y}Nd_yCo_yFe_{12-y}O_{19}/BaTiO_3$/Polypyrrole at y = 0.25	BNPY25
$Ba_{1-y}Nd_yCo_yFe_{12-y}O_{19}/BaTiO_3$/Polypyrrole at y = 0.1	BNPY1
$Ba_{1-x}Gd_xCo_xFe_{12-x}O_{19}/BaTiO_3$/Polypyrrole at x = 0.5	BGPY5
$Ba_{1-x}Gd_xCo_xFe_{12-x}O_{19}/BaTiO_3$/Polypyrrole at x = 0.2	BGPY2
$BaFe_{12}O_{19}/BaTiO_3$/Polypyrrole	BBPY
$BaFe_{12}O_{19}$ /Polyaniline	COP

10. 4. 2. Mid infrared spectra analysis

FT-IR spectra have been examined to identify the remains of chemicals taken at initial level for synthesis process (Fig. 10. 3). Hexaferrite formation are indicated by two prominent peaks that arise near 428 cm^{-1} and 582 cm^{-1}, attributed to the vibration of ferric crystallographic site (octahedral and tetrahedral respectively) The stretching vibrations of metal-oxygen bond with ν_1 and ν_2 mode are the reason for these peaks [59].

The peaks in the range 1128-1183 cm^{-1} and at 1079 cm^{-1} are attributed to in-plane deformation vibration of C-H bond and in plane C-H bending vibration mode in N=Q=N, where Q represents quinoid ring system. The band at 1142 cm^{-1} is expected due to polarization of pyrrole monomer. The broad absorption band near 3497 cm^{-1} is the characteristics peak of polypyrrole [118-120]. The peak near 525 cm^{-1} pointing the presence of barium titanate. This peak attributes to the TiO_6 octahedral stretching.

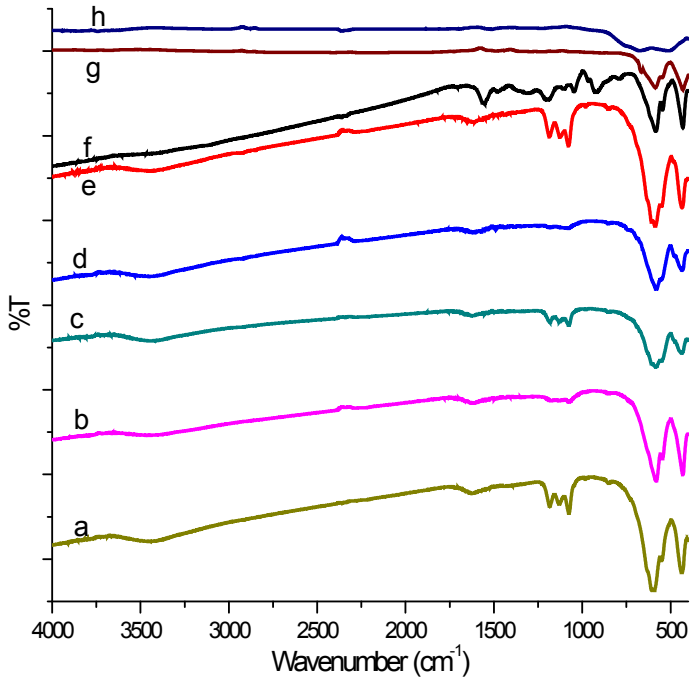

Fig 10. 3: Mid infrared region spectra $Ba_{1-x}Gd_xCo_xFe_{12-x}O_{19}$ (or $Ba_{1-y}Nd_yCo_yFe_{12-y}O_{19}$)/$BaTiO_3$/Polypyrrole composite at (a) y = 0.4, (b) y = 0.25, (c) y = 0.1, (d) x = 0.5, (e) x = 0.2, (f) x = 0.0 whereas (g) Pure barium hexaferrite and (h) Pure Barium titanate

10. 4.3. Electron spin resonance spectroscopy

ESR spectra of barium hexaferrite and composite having barium hexaferrite, barium titanate and polypyrrole has been taken at room temperature in X band. The first derivative signal vs applied magnetic field has been studied. The addition of polymer has enhanced the signal intensity (Fig. 10. 4). The ESR spectra parameters (g and ΔH) has been evaluated and reported in Table 10.2. The two ferromagnetic resonance signal curves are present in the spectra that may ascribe to the coupling of ferric ions at interstitial sites due to octahedral and tetrahedral sites. The peak intensity has been increased due to contribution of electrons of polymer [91].

Table 10. 2: ESR parameters of for (a) Barium hexaferrite and (b) BGPY2 taken at room temperature in X band.

Sample	ΔH(gauss)	g factor
Barium hexaferrite	531	1.99
BGPY2	60	2.13

The increase in intensity is directly linked to the number of spins taking part in interaction. Pyrrole addition does not increase the signal intensity for g= 4 but increases for g= 2 (appx.), which is the g value for free electron. So the intensity get increased. The interaction of the spins with their environment also effects the absorption peak [41, 42].

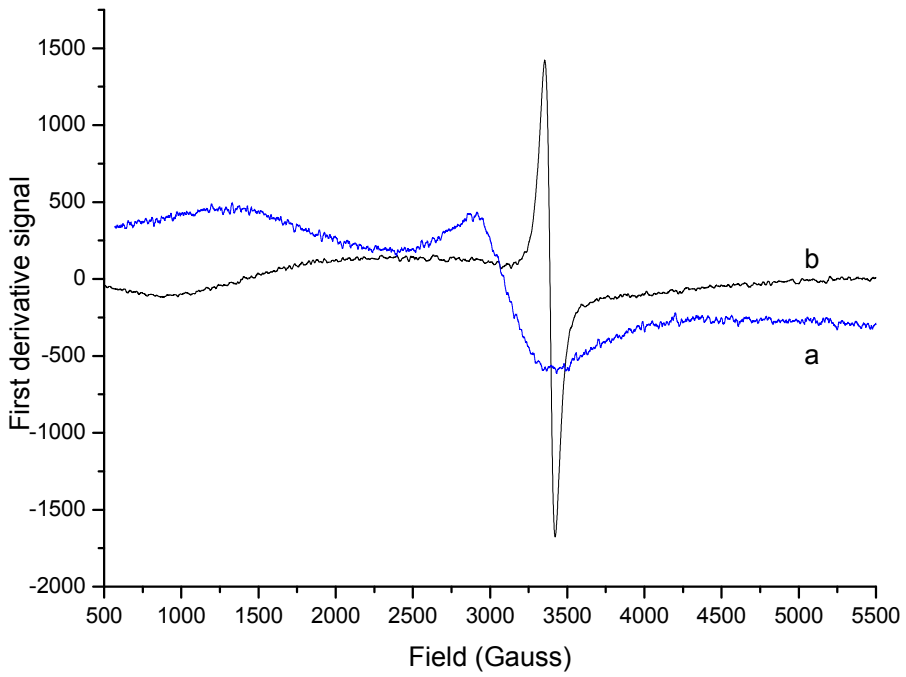

Fig 10. 4: ESR spectra for (a) Barium hexaferrite and (b) Composite having barium hexaferrite, Barium Titanate and polypyrrole (BBPY) at room temperature in X band.

10.4.4. Magnetic properties

Hysteresis loop for barium ferrite/$BaTiO_3$/Polypyrrole composites recorded at room temperature has been shown in Fig. 10. 5. The magnetic parameters has been evaluated from M-H curve and reported in the Table 10. 3.

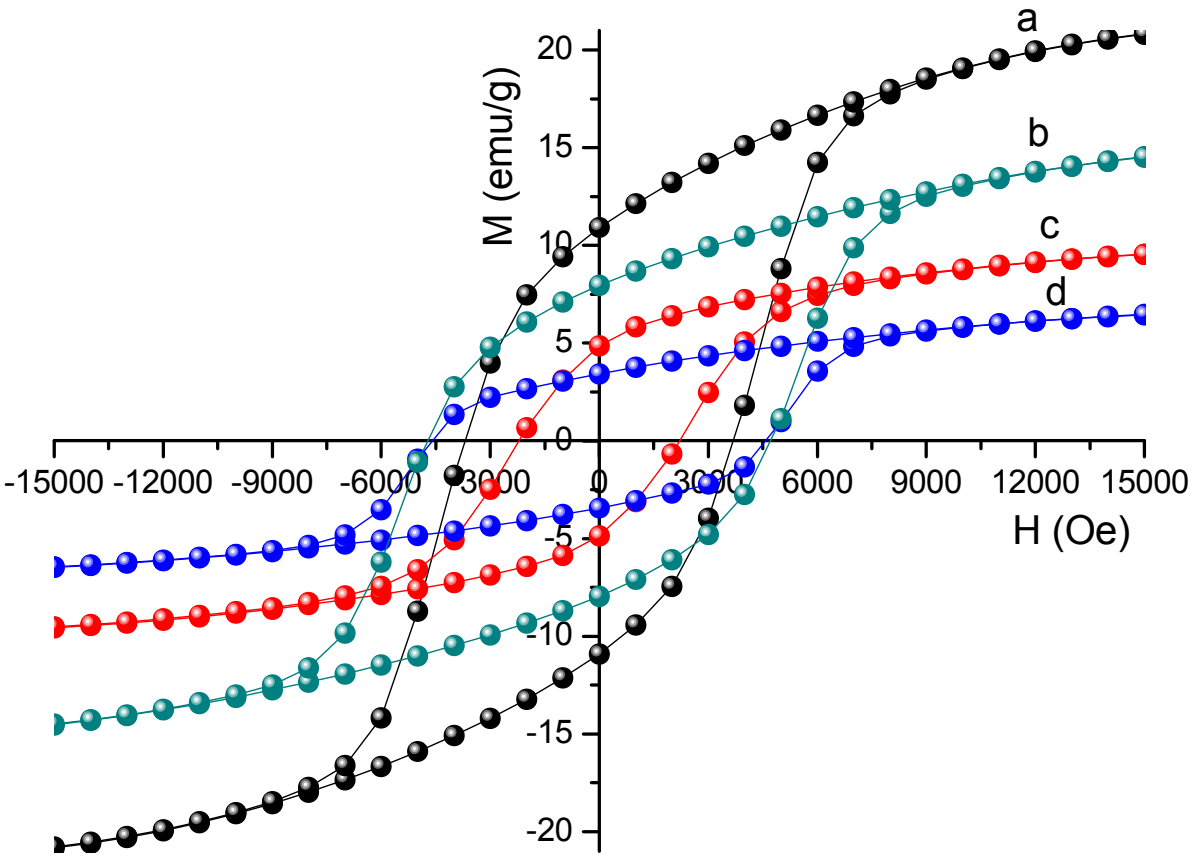

Fig 10. 5: Hysteresis loop for composites $Ba_{1-x}Gd_xCo_xFe_{12-x}O_{19}$ (or $Ba_{1-y}Nd_yCo_yFe_{12-y}O_{19}$)/$BaTiO_3$/Polypyrrole (a) x = 0.0, (b) y = 0.25, (c) x = 0.5 and (d) y = 0.4

The highest value for saturation magnetization is 20 emu/g at an external applied field of 15 kOe. Composites are showing less saturation magnetization than the pure barium hexaferrite as reported elsewhere [121]. Magnetic parameters have been reduced because of the presence of barium titanate and polymer. Barium titanate and barium hexaferrite both are of nano size. At the time of synthesis of composite, both compounds were homogenised, that leads to the amalgamation of particles and reduced the superexchange interaction of magnetic ions causing reduction of

magnetic properties [39]. Grain size affects the properties like initial permeability, linewidth, domain wall displacement and coercive force. The new absorption mechanism arise due to decrease of particle size to nano range. The natural resonance frequency of barium hexaferrite lies in the range 50-60 GHz because of large magneto-crystalline anisotropy and high saturation magnetization (72 emu/g) [39]. But the weakening of magnetic anisotropy can shifts the resonance frequency to lower frequency. If coercivity is taken into account of anisotropy field, then resonance frequency directly depends on saturation magnetization and coercivity [1]. The surface effects become prominent when particle size decreases in nano range and makes the micro wave and magnetic properties different than those of bulk material [41, 122].

Table 10. 3: Coercivity, saturation magnetization and retentivity of barium hexaferrite/ $BaTiO_3$/Polypyrrole and Hexaferrite/Polyaniline (COP).

Composite	H_C (Oe)	M_S (emu/g)	M_r(emu/g)
BBPY	3657	20	10.98
BGPY	2168	8.91	4.90
BNPY4	4520	5.54	3.38
BNPY25	4636	13.46	7.93
COP	5560	23.61	13.30

10.4. 5. Surface features

Transmission electron microscopy (TEM) has been used to determine surface morphology of composite. The grains entrapped in polymer can be visualized. Due to different shape of hexaferrite and barium titanate grains and amorphous nature of polymer, it is hard to see the shape of grains (Fig 10. 6). Grains form some clusters owing to the inter particle interaction of magneto-dipole [41].

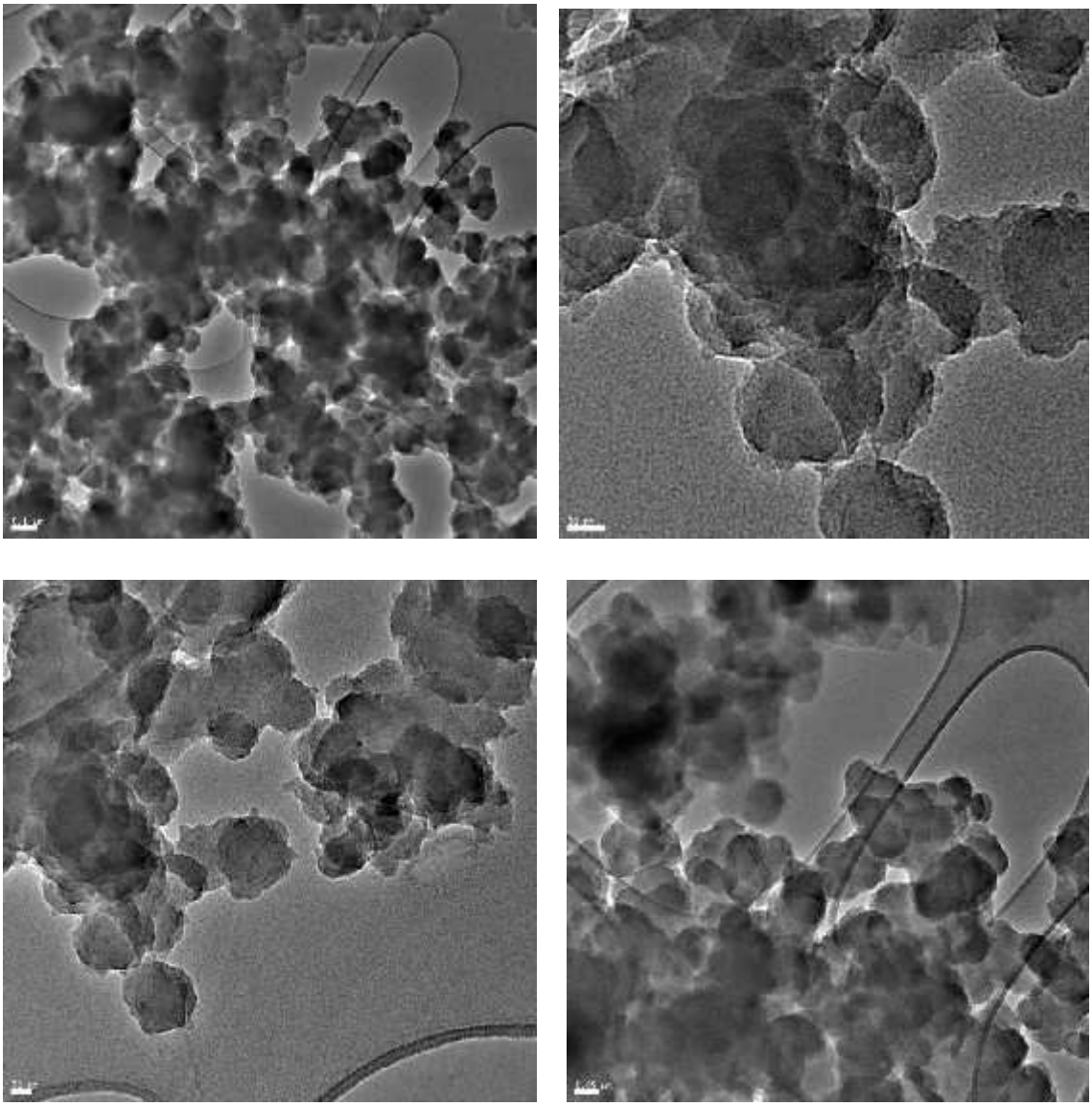

Fig 10. 6: Transmission electron micrographs of magneto-electric composite of hexaferrite ferrites and barium titanate enclosed by polypyrrole (BBPY).

10. 4.6. Radiation loss study

The K_u and K band (12.4-26.5 GHz) has been used for the radiation absorbance properties. Frequency region 12.4-18 GHz: From the Fig. 10. 7, it is clear that distinct patterns are present at almost same frequency but with different intensity value. They possess almost equal width of the

loss band for all composite samples at a particular frequency. Three consecutive peaks are present in 12.4- 18 GHz (table 10. 4). Sample BBPY have shown the better absorbance than other samples

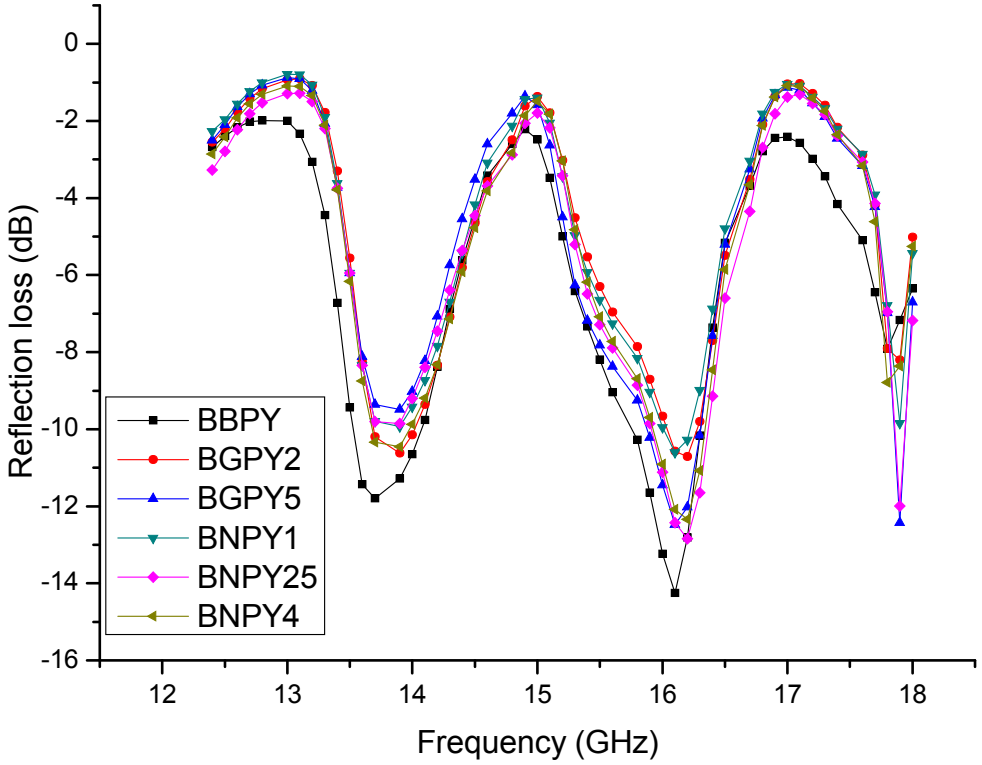

Fig 10. 7: Reflection loss for Gd-Co (or Nd-Co) substituted Barium hexaferrite/ Barium titanate/ Pyrrole composite

because of the high saturation magnetization of this sample as compared to others. Electrical properties of polypyrrole support the absorption. The dielectric material get polarized and uses the incident energy for polarization, the multiple reflections of hexaferrite and barium titanate and electrical conductivity owes to the increase of reflection loss. Fig 10.8 and 10.9 illustrates the real (ε′) and imaginary part (ε′′) of complex permittivity for the composite sample and fig. 10.10 and 10.11 is showing real (μ′) and imaginary part (μ′′) of permeability.

Table 10. 4. Reflection loss values for different composite at different frequency

	Peak 1		Peak 2		Peak 3	
	Max reflection loss at Frequency	Reflection loss at highest loss frequency	Max reflection loss at Frequency	Reflection loss at highest loss frequency	Max reflection loss at Frequency	Reflection loss at highest loss frequency
BBPY	13.7	-11.76	16.09	-14.23	17.80	-7.86
BGPY2	13.9	-10.60	16.20	-10.67	17.89	-8.15
BGPY5	13.89	-9.49	16.09	-12.41	17.90	-12.39
BNPY1	13.89	-9.92	16.10	-10.55	17.90	-9.81
BNPY25	13.84	-9.83	16.20	-12.82	17.90	-11.94
BNPY4	13.87	-10.42	16.188	-12.30	17.80	-8.76

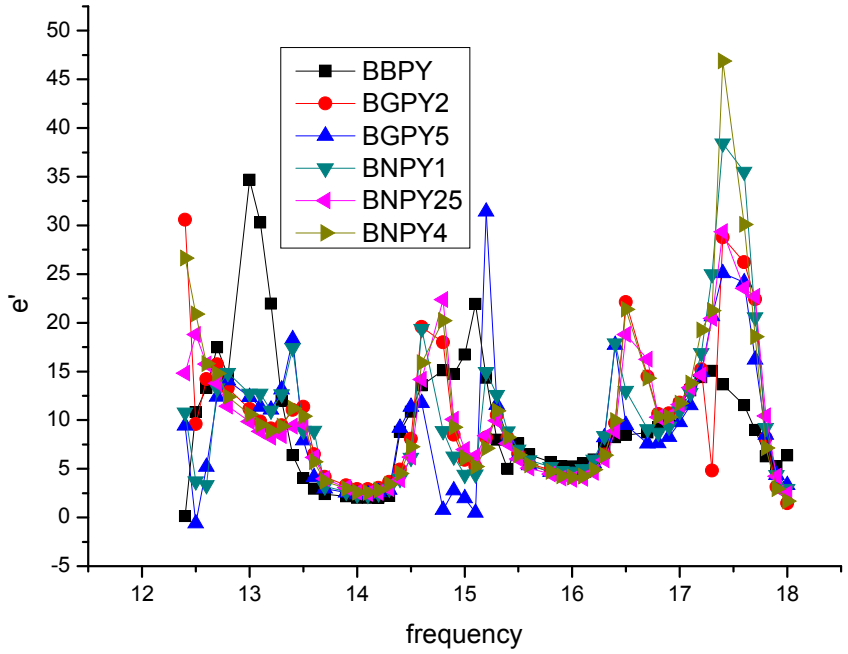

Fig 10. 8: Real part of complex permittivity of prepared composite in range 12.4-18 GHz

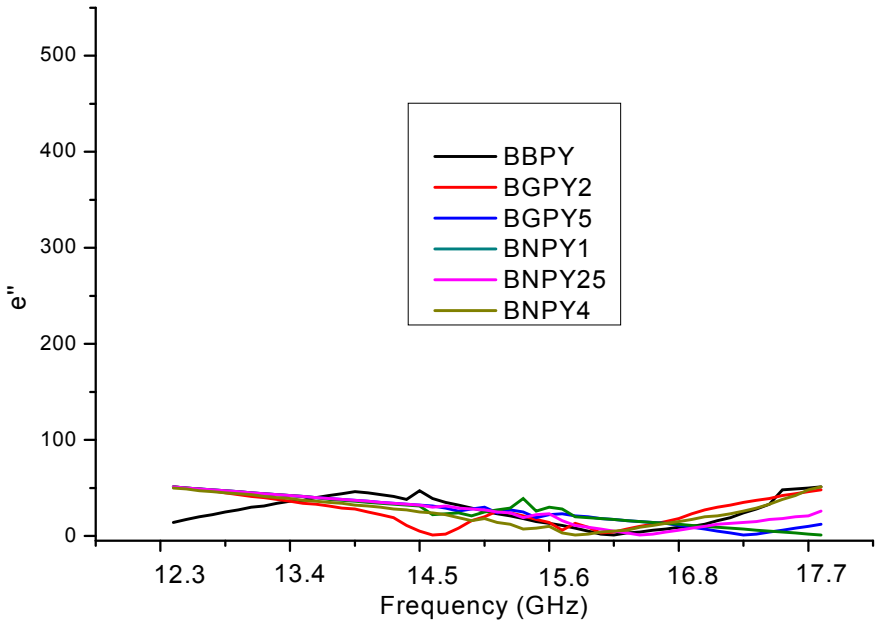

Fig 10. 9: Imaginary part of complex permittivity for composite in range 12.4-18 GHz

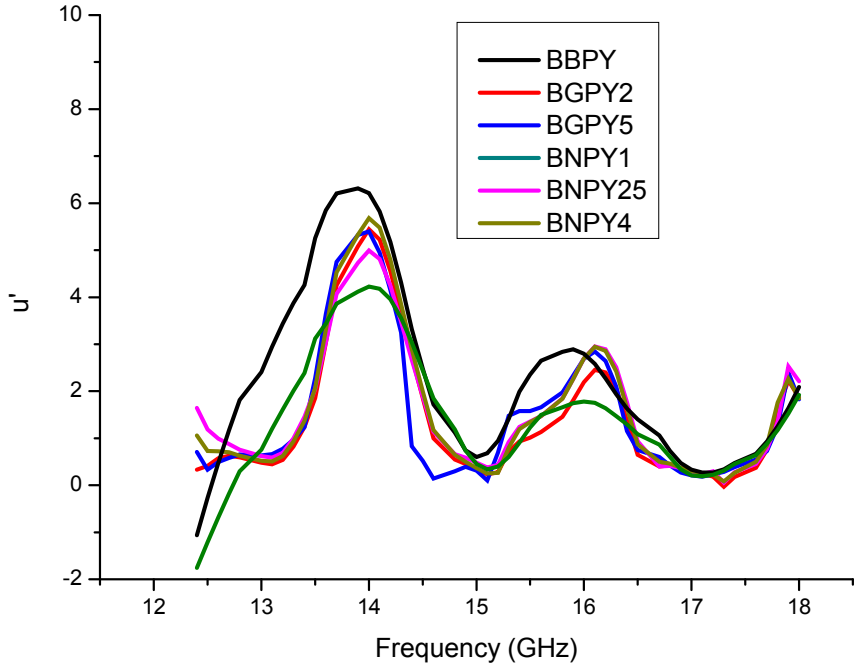

Fig 10. 10: Real part of complex permeability for composite in range 12.4-18 GHz

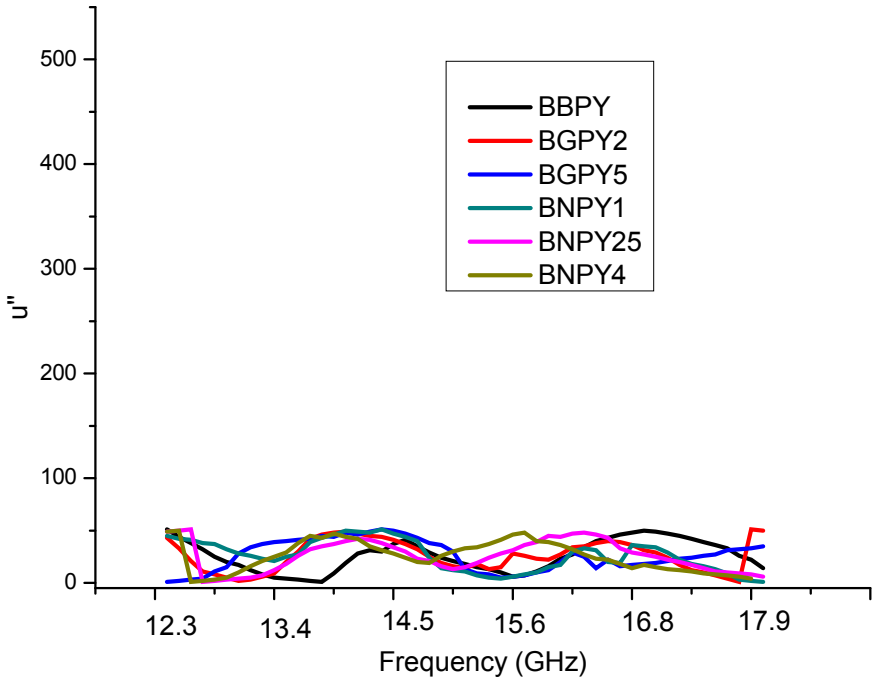

Fig 10. 11: Imaginary part of Complex permeability for composite in range 12.4-18 GHz

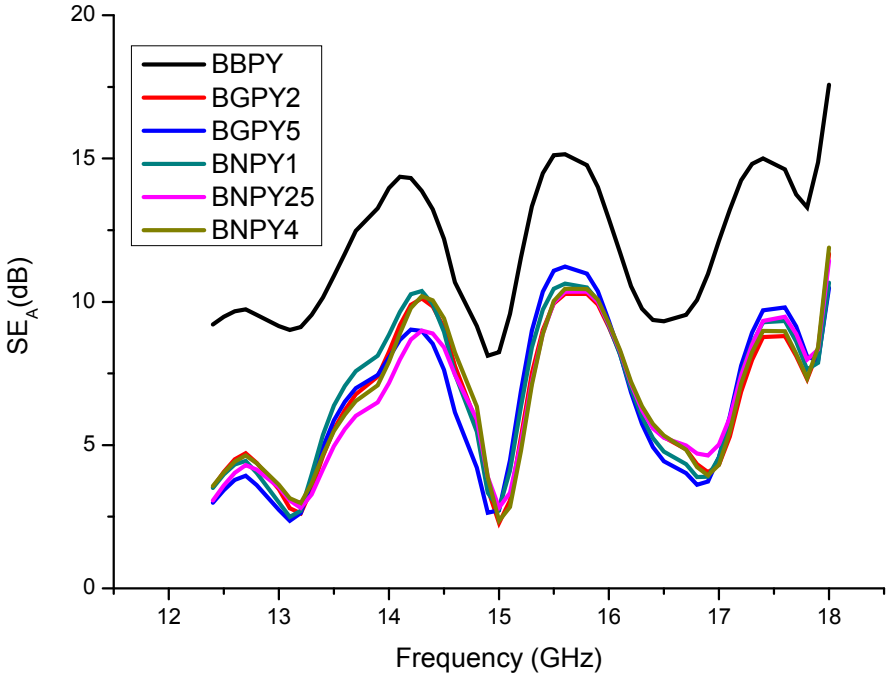

Fig 10. 12. The Shielding effectiveness for absorption (SE_A) for prepared composite in range 12.4-18 GHz

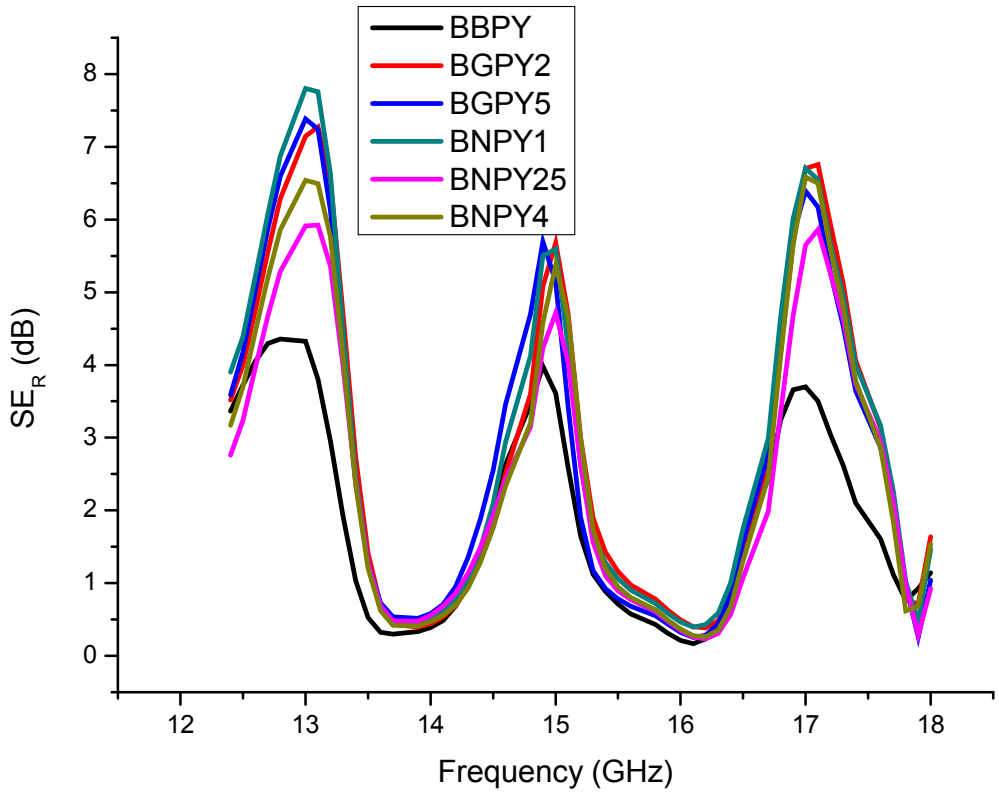

Fig 10. 13. The Shielding effectiveness for reflection (SE_R) for prepared composite in range 12.4-18 GHz

Frequency Band (18-26.5 GHz): The real and imaginary parts of permittivity and permeability are shown in fig. 10.14, 10.15, 10.16 and 10.17. The radiation losses in 18-26.5 GHz are shown in fig. 10.18. The shielding effectiveness in absorption and reflection is shown in fig. 10.19 and 10.20. The permeability and permittivity shows too much variation in their values with zigzag plots. In sample BBPY, The SE_A increases constantly, showing no maximum value for radiation loss. In sample BGPY2, maximum reflection loss (occur at 20 GHz), whereas imaginary part of permittivity also shows maximum value near 20 GHz range. The electric losses contributes more to the radiation loss. The maximum loss occur near 24 GHz, SE_R, SE_A, μ', ε' and ε'' also increases near 24 GHz for sample BGPY5. Shielding effectiveness of Reflection is highest for sample BNPY1, the ε' is high for this sample too, the incident radiations has been lost by sample in form of storage, whereas μ' and μ'' is almost equals to zero. Reflection loss for sample BNPY25 is maximum at frequency 22.50 (-14.12 dB) GHz, the real part of permittivity varies with reflection loss for BNPY25. It has been depicted that, if the ε' or ε'' is maximum then the shielding

effectiveness for reflection will be maximum. COP sample shows reflection loss in low frequency range, For COP sample, ε′ and ε′′ are high along with reflection loss near 20.5 GHz.

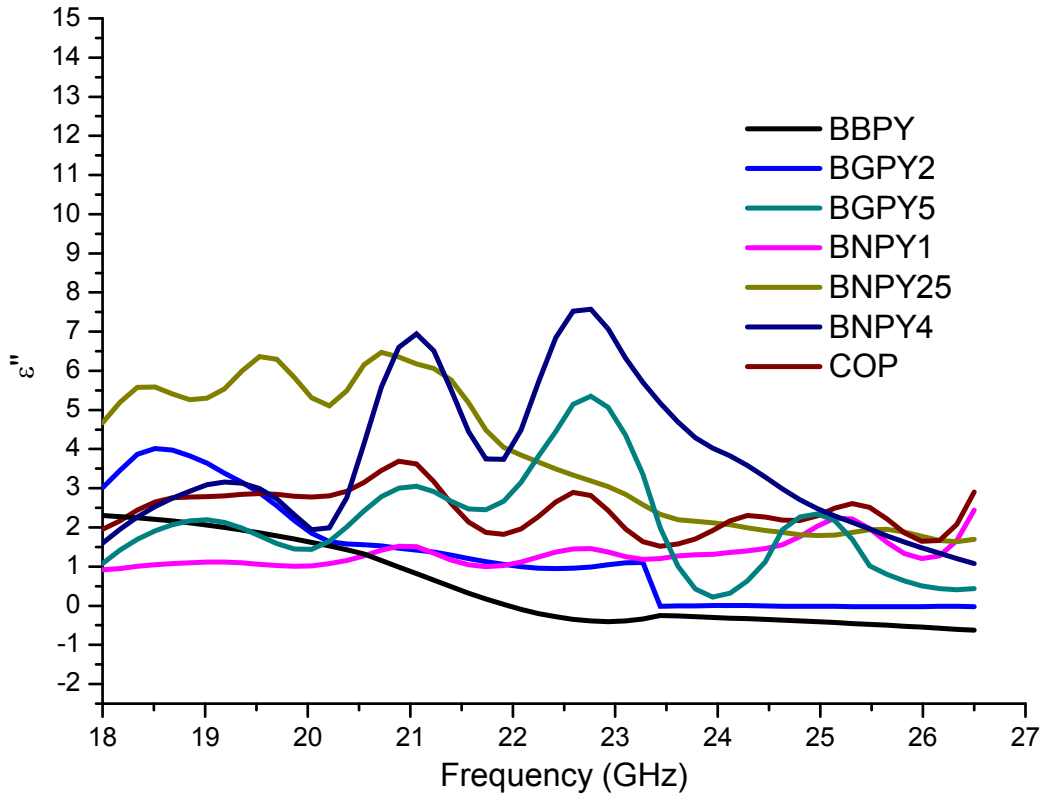

Fig 10.14: Imaginary part of complex permittivity of prepared composite in range 18-26.5 GHz

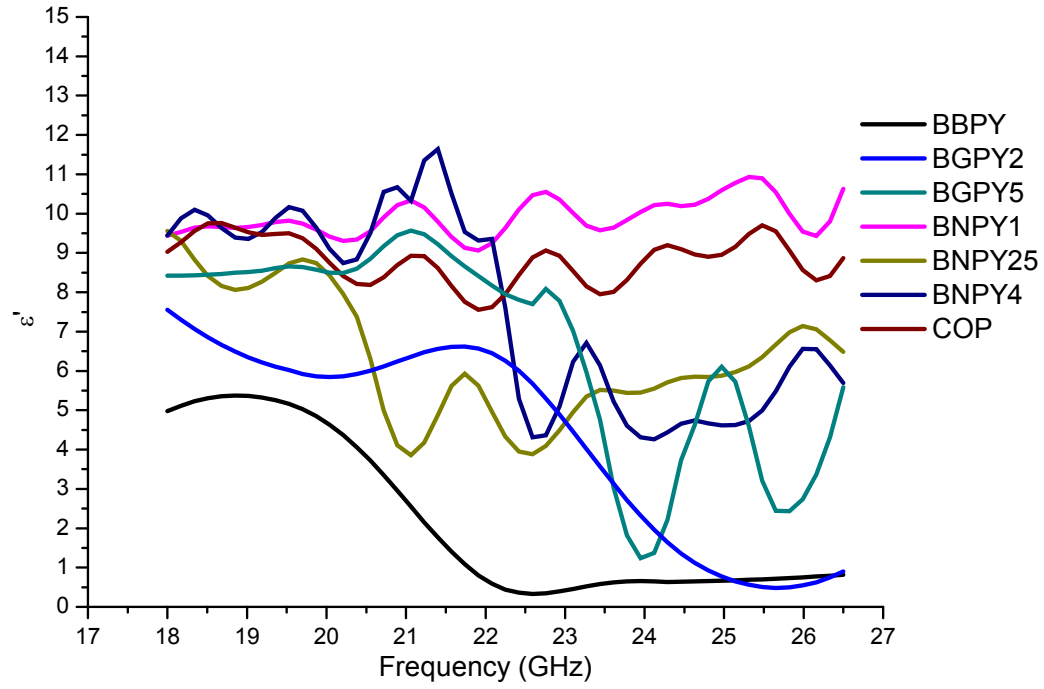

Fig 10.15: Real part of complex permittivity of prepared composite in range 18-26.5 GHz

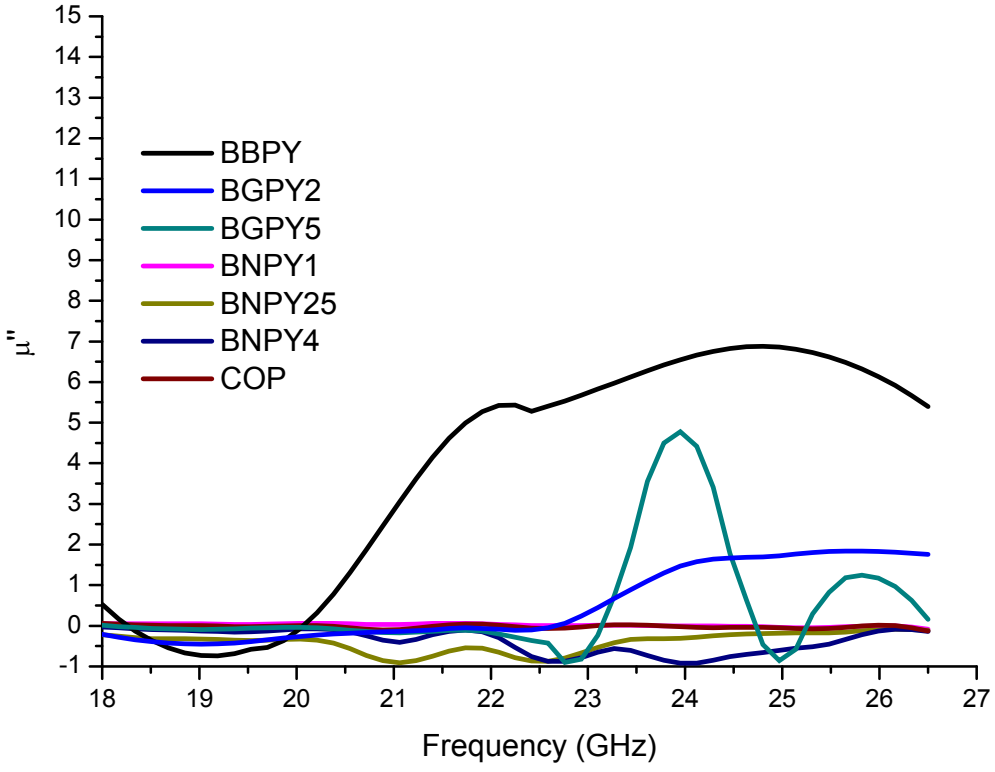

Fig 10.16: Imaginary part of complex permeability of prepared composite in range 18-26.5 GHz

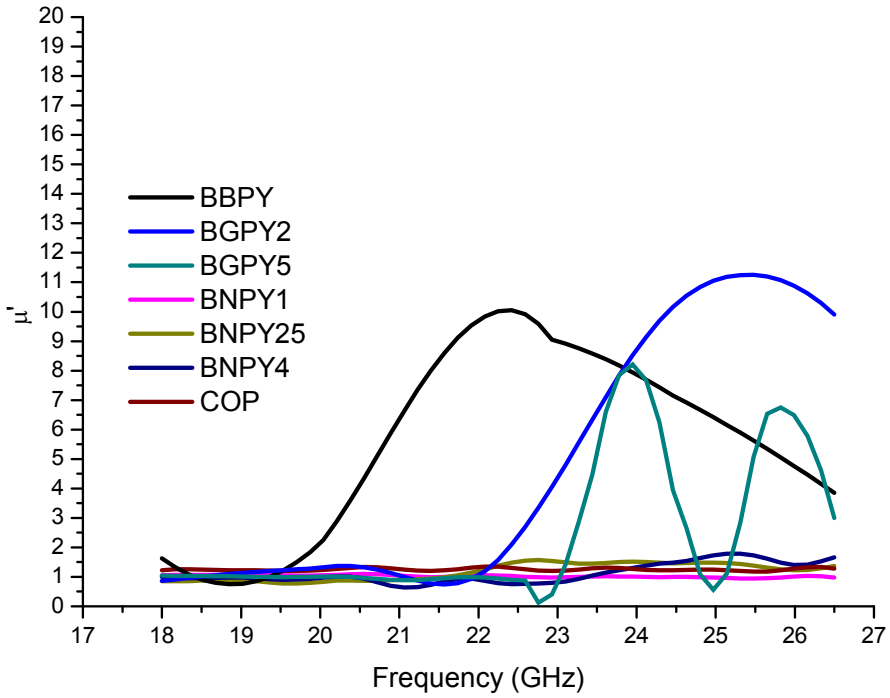

Fig 10.17: Real part of complex permeability of prepared composite in range 18-26.5 GHz

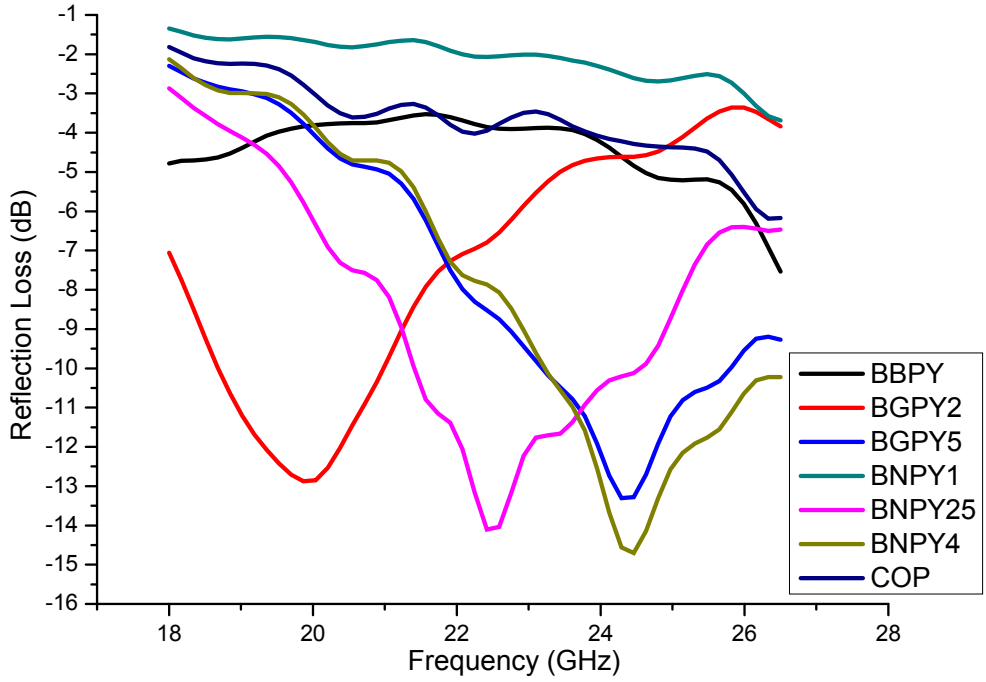

Fig 10.18: Reflection loss for Gd-Co (or Nd-Co) substituted Barium hexaferrite/ Barium titanate/ Pyrrole composite in range of 18-26.5 GHz.

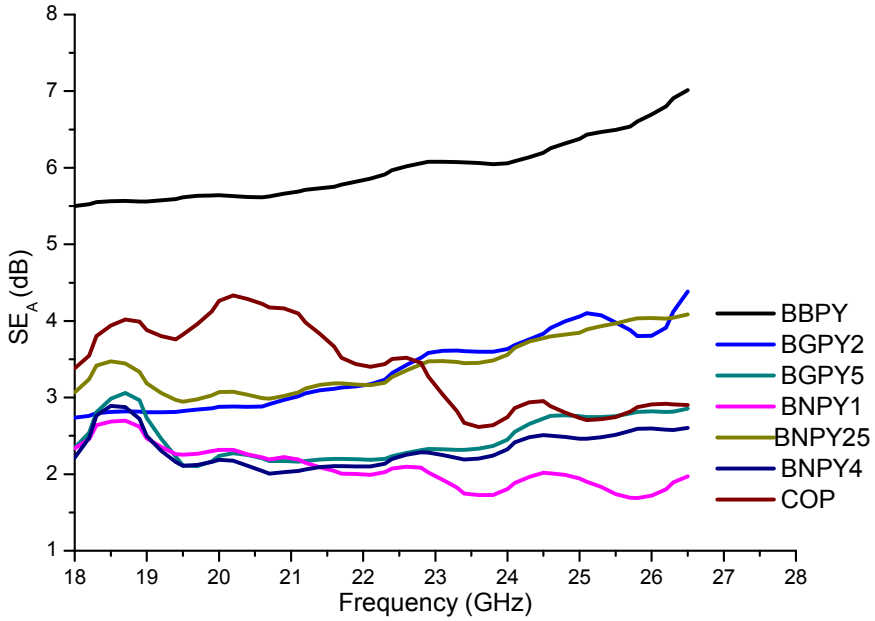

Fig 10.19: The Shielding effectiveness for absorption (SE_A) for prepared composite in range 18-26.5 GHz

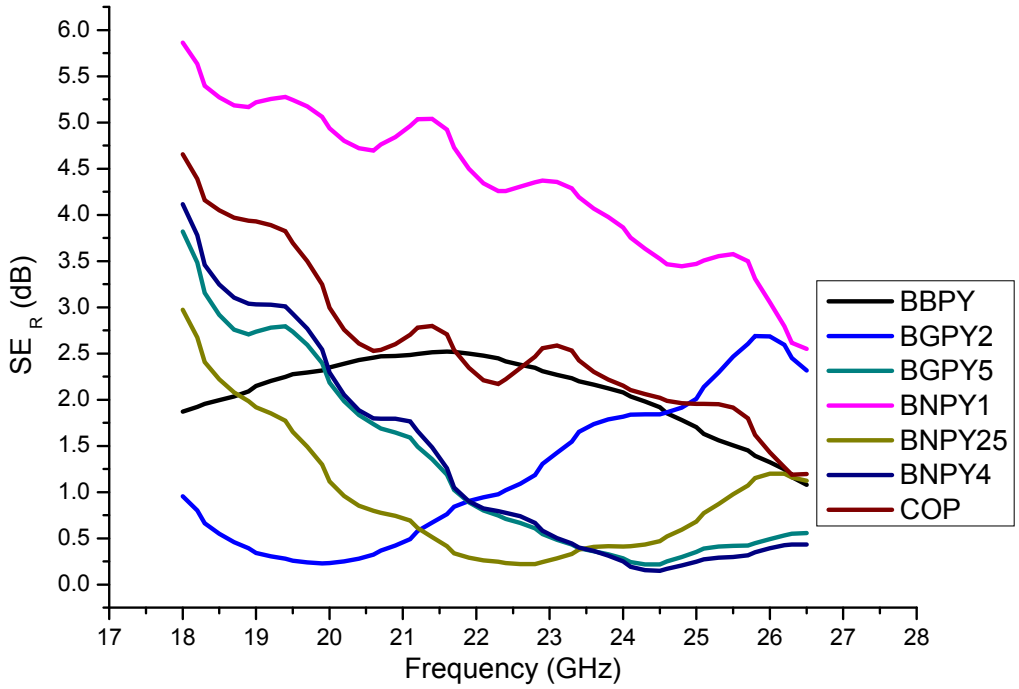

Fig 10.20: The Shielding effectiveness for reflection (SE_R) for prepared composite in range 18-26.5 GHz

The synthesized material can be utilized as a radar absorbing material. Following relation has been used to calculate the reflection loss in accordance with theory of absorbing wall [43]:-

$$RL\,(dB) = 20\log\left|Z - 1/Z + 1\right|$$

where Z is the normalized input impedance. It has been observed that at lower frequency, the band width of loss is more as compared to bandwidth occur at high frequency. Moreover, the losses increase, indicated by sharp peaks when approaches high frequency. The permittivity and permeability shows the variation in their values. A resonance in K_u and K band frequency exist because of electron hopping ($Fe^{3+} \leftrightarrow Fe^{2+}$) frequency matching. The real part of permeability and permittivity contributes more to the losses because of arise of ferromagnetic resonance. The frequency of real part of permeability peaks matches exactly with the frequency of radiation loss peaks. The higher permeability value cause decrease of ferromagnetic resonance frequency [123, 124]. The interfacial polarization caused by low resistive grains separated by a highly resistive grain boundaries, increases the real part of permittivity. The matrix of conducting polypyrrole, barium titanate and hexaferrite contribute to the dielectric losses (ε′′) and dielectric constant (ε′). The unsaturated coordination on the surface, hexaferrite of nano-size, the dangling bond atoms, the surface area are enhanced and leads to the multiple scattering cause loss of radiation.

The shielding effectiveness has been calculated from the S parameters obtained from Vector network analyser. The shielding effectiveness for absorption (SE_A) and reflection (SE_R) has been plotted in fig 10. 12 and fig 10. 13. According to the classical electromagnetic theory, the shielding effectiveness for thick shield material having thickness (d), conductivity (σ_{AC}), skin depth (δ) and permeability (μ) can be represent as:

$$SE_A(dB) = 20\frac{d}{\delta}\log e \quad or \quad 20d\left(\sqrt{\frac{\omega\mu\sigma_{AC}}{2}}\right)\log e$$

Reflectivity, absorptivity and transmittance can be calculated from S parameters (S_{11} and S_{21}). Shielding effectiveness is the ratio of transmitted to incident power and can be expressed as:

$$\mathrm{SE\,(dB)} = -10\log\left(\frac{P_t}{P_o}\right)$$

where P_t is transmitted and P_0 is incident power. Transmission and Reflection coefficients can be calculated from $T = |S_{21}|^2 = |S_{12}|^2, R = |S_{11}|^2 = |S_{22}|^2$. Effective absorption can be obtained from following expression: $A_{eff} = \left(\frac{1-R-T}{1-R}\right)$. The shielding effectiveness for reflection and absorption have been evaluated from

$$SE_R = -10\log(1-R)$$

$$SE_R = -10\log(1-A_{eff})$$

It has been concluded that the real part of permittivity contributes to the SE_R whereas the real part of permeability peaks matches with SE_A peaks. SE_A is slightly high that means the storage of energy that is absorption is more than the losses [39].

Conclusion

The composite material of gadolinium, neodymium and cobalt doped barium hexaferrite, nano size barium titanate and polypyrrole has been successfully synthesized with emulsion polymerization. The XRD shows the crystalline structure and formation of nanocomposite. The FT-IR spectra provide the evidence of the presence of ferrite particles, barium titanate and polypyrrole. The magnetic properties has effected the radiation losses. The peaks having reflection loss in -10 to -15 dB range are present in the plots. ESR spectra show that the polypyrrole has increased the intensity of the signal. The prepared material shows good reflection loss value, consequently, it can be used as a promising material for radiation absorption.

CHAPTER-11

SUMMARY AND CONCLUSION

In this work, composites of polymer, substituted hexaferrite and dielectric material has been successfully synthesized for radiation absorbance. Rare earth substituted barium hexaferrite has been synthesized via Modified Pechini Sol Gel method. Dielectric material has been synthesized via oxalate process and physical embedment of these particles in polymer is done by emulsion polymerization.

The magneto plumbite structure of hexaferrite has been confirmed by XRD. Microstructural analysis confirms the formation of hexaferrite phase along with some percentage of impurities in some samples. The formation of hexaferrite phase indicates that the rare earth metals have occupied the preferential sites in the lattice.In some samples, the high concentration of rare earth does not undergoes completion of reaction. Hence, more time and high temperature were needed for completion of reaction. The formation of hexagonal structure takes place and the morphology of the surface of the as-prepared samples are non-homogenous. Average crystallite size which is estimated by Scherer formula is found to be in nano range (<100 nm). This range of size is useful in various applications. The presence of two peaks at 430 cm^{-1} and 580 cm^{-1} in FT-IR spectra supports the presence of octahedral and tetrahedral sites in hexaferrites. Vibrational modes in FT-Raman spectra favours the affirmation of magneto-plumbite structure. The impurities have degraded the properties but from an application point of view, the properties are still much better for utilization in industry.

It has been observed that the hexaferrite phase forms at a temperature of 400-700^{o}C and the formation temperature depends on the substituent's concentration. The steps occur in reaction are clearly visible with the increase in temperature. It has been found that neodymium substitution has decreased the formation temperature, but in case of gadolinium and lanthanum, the formation temperature is almost same.

Samples show normal ferrite dielectric behaviour. A normal ferrite behaviour of dielectric constant which may be due to conducting grains and hopping of electrons between Fe^{3+} and Fe^{2+}

are analysed with Koop's phenomenological theory and Maxwell Wagner. The dielectric constant value reaches maximum at low frequency but as frequency increases, dielectric constant decreases. Optical study analysis indicates the indirect band gap of samples where band gaps are ranging from 3.7 eV to 4.50 eV. UV–Vis-NIR reveals that the band gap of as prepared samples increases with substitution. The nano size of particles also effects the band gap. The band gap increases with decrease in size of crystallites.

From analysis, it is observed that coercivity and saturation magnetization shows decrement in their values with increase in substitution in case of neodymium and gadolinium. Lanthanum substitution has enhanced the magnetic properties, whereas the neodymium and gadolinium have deteriorated the properties. Despite the deterioration of properties, prepared materials can be used as a recording media because of high surface area and high coercivity and saturation magnetization (>2500 Oe). The effect of saturation magnetization and coercivity have been observed on the radiation absorbance properties. Mossbauer study reveals that the substituents have replaced the ferric ions and the hyperfine parameters somewhat vary than pure hexaferrite. The samples are showing high resistivity and can be used as resistors to reduce eddy currents.

Surface morphology revealed by SEM, FESEM, TEM and AFM shows the hexagonal crystal structure. The particles are in nano range. The composites, enwrapped by the polymer, can be observed in TEM images. The cubic cell structure impurities can be seen in AFM images.

Fe^{3+} ions are responsible for the observed peak to peak line width examined in ESR spectra, but the signal intensity increases with addition of polymer. A dielectric material, barium titanate has been synthesized for electrical losses via oxalate process. Barium titanate exhibiting cubic structure as affirms by XRD analysis. The prepared barium titanate is in nano size (32 nm).

The magnetic properties have affected the radiation absorbance properties. Higher is the saturation magnetization, higher is the reflection loss. It has also been observed that the intensity of reflection loss increases with increase in frequency and the area of peak decreases with increase in frequency. Characteristic peaks of polymer shows their presence in FT-IR spectra in composite samples. The radiation absorbance of the composite is less than 30 dB. X-Ray diffraction patterns shows the presence of all phases present in composite and has been confirm by the distinctive peaks of composite material.

CHAPTER-12

BIBLIOGRAPHY

[1] U. Ozgur, Y. Alivov, H. Morkoc, *Journal of Material Science: Material in Electronics*, 20, 789 (2009).

[2] A. Thakur, R.R. Singh, P. B. Barman, *Materials Chemistry and Physics*, 141, 562 (2013).

[3] F. M. M. Pereira, C. A. R. Junior, M. R. P. Santos, R. S. T. M. Sohn, F. N. A. Freire, J. M. Sasaki, J. A. C. de Paiva, A. S. B. Sombra, *Journal of Material Science: Material in Electronics*. 19, 627 (2008).

[4] M. Radwan, M. M. Rashad, M. M. Hessien. *Journal of Materials Processing*, 181, 106 (2007).

[5] T. Gonzalez-Carreno, M. P. Morales, C. J. Serna, *Materials Letters*, 43, 97 (2000).

[6] M. Cernea, S. G. Sandu, C. Galassi, R. Radu, V. Kuncser, *Journal of Alloys and Compounds*, 561, 121 (2013).

[7] P. Bhattacharya, S. Dhibar, G. Hatui, A. Mandal, T. Das and C. K. Das, *RSC Advances*, 4, 17039 (2014).

[8] C. Navau, J. Prat-Camps, O. Romero-Isart, J. I. Cirac and A. Sanchez, *Physical. Review Letters*. 112, 253901 (2014).

[9] M. N. Ashiq, M. J. Iqbal, P. H. Najam-ul-Haq, M.Gomez, A.M. Qureshi, *Journal of Magnetism and Magnetic Material*, 324, 15 (2012).

[10] H. A. Patel, J. Byun, C. T. Yavuz, *Journal of Nanoparticle Research,* 14, 881 (2012).

[11] V. Anbarasu, P. M. Md Gazzali, T. Karthik, A. Manigandan, K. Sivakumar, *Journal of Material Science: Material in electronics*, 24, 916 (2013).

[12] G. Litsardakis, I. Manolakis, K. Efthimiadis, *Journal of Alloys and Compounds* 427, 194 (2007).

[13] F. Khademi, A. Poorbafrani, P. Kameli, H. Salamati, *Journal of Superconductivity and Novel Magnetism*, 25, 525(2012).

[14] P. Winotai, S. Thongmee, I. M. Tang, *Materials Research Bulletin*, 35, 1747(2000).

[15] V. N. Dhage, M. L. Mane, A. P. Keche, C. T. Birajdar, K. M .Jadhav, *Physica B*. 406, 789 (2011).

[16] I. Bsoul, S. H. Mahmood, *Journal of Alloys and Compounds* 489, 110 (2010).

[17] S. Ounnunkad, *Solid State Communication*, 138, 472(2006).

[18] H. Xiaogu, Z. Jing, W. Hongzhou, Y. Shaoteng, W. Lixi, Z. Qitu, *Journal of Rare Earths*, 28, 940 (2010).

[19] H. Feng, L. Fernandez- Garcia., X. S. Liu, D-R Zhu, M. Suárez, J. L. Menendez*, Journal of Applied Physics*. 109, 113906 (2011).

[20] H. Sozeri, I. Kuucuk, H. Ozkan, *Journal of Magnetism and Magnetic Material*. 323, 1799 (2011).

[21] I. Ali, M. U. Islam, M. S. Awan, M. Ahmad, M. A. Iqbal, *Journal of Superconductivity and Novel Magnetism*. 26, 3277 (2013).

[22] M. K. Tehrani, A. Ghasemi, M. Moradi, R. S. Alam, *Journal of Alloys and Compounds*, 509, 8398 (2011).

[23] M. L. Gregori, M. S. Pinho, R. C. Lima, J. C. S. Leandro, T. Ogasawara, *Key Engineering Material*. 264-268, 1229 (2004).

[24] X. Liu, P. Hernández-Gómez, K. Huang, S. Zhou, Y. Wang, X. Cai, H. Sun, B. Ma, *Journal of Magnetism and Magnetic Material*, 305, 524 (2006).

[25] A. G. Belous, O. I. V'yunov, E. V. Pashkova, V. P. Ivanitskii and O. N. Gavrilenko, *Journal of Physical Chemistry B*. 110, 26477(2006).

[26] Y. Liu, M. G. B. Drew, Y. Liu, J. Wang, M. Zhang, *Journal of Magnetism and Magnetic Material*, 322, 814 (2010).

[27] J. C. Corral-Huacuz, G. Mendoza-Suárez, *Journal of Magnetism and Magnetic Material*

242, 430 (2002).

[28] V. V. Soman, V. M. Nanoti, D. K. Kulkarni, *Ceramics International*, 39, 5713 (2013).

[29] A. Ataie, A. Mali, *Journal of Electroceramics*. 21, 357 (2008).

[30] A. P. Safronov, O. M. Samatov, A. I. Medvedev, I. V. Beketov, A. M. Murzakaev *Nanotechnologies in Russia*. 7, 486 (2012).

[31] X. Liu, J. Wang, L.M. Gan, S. C. Ng, J. Ding, *Journal of Magnetism and Magnetic Material*, 184, 344 (1998).

[32] H. Li, J. Huang, Q. Li, X. Su. *Journal of Sol-Gel Science and Technology*, 52, 309 (2009).

[33] B. Wessling, *Polymers*, *2*, 786-798 (2010).

[34] J. Huang, S. Virji, B. H. Weiller, and R. B. Kaner, Journal of American Chemical Society, 125, 314 (2003).

[35] H. S. Nalwa, Handbook of Organic conductive molecules and polymers Vol 2 (Chichester: Wiley) (1997)

[36] T. A. Skotheim, J. Reynolds, Handbook of Conjugated Polymers; Theory, Synthesis, Properties, and Characterization, 3rd Ed., CRC press (2007).

[37] X. Zhang and S. K. Manohar, Bulk, Journal of American Chemical Society, 126, 12714-12715 (2004).

[38] K Fehse, G Schwartz, K Walzer, K Leo, *Journal of Applied Physics* **101,** 124509 (2007).

[39] A. Ohlan, K. Singh, A. Chandra and S.K. Dhawan, *Applied Physics Letters*, 93, 053114 (2008).

[40] A. Ohlan, K. Singh, A. Chandra, V. N. Singh, and S. K. Dhawan, *Applied Physics Letters*, 106, 044305 (2009).

[41] C.C. Yang, Y.J. Gung, W.C. Hung, T.H. Ting, K.H. Wu, *Composite Science Technology* 70, 466 (2010).

[42] C.C. Yang, Y.J. Gung, C.C. Shih, W.C. Hung, K.H. Wu, *Journal of Magnetism and Magnetic Materials*, 323, 933 (2011).

[43] S. Ozah and N.S. Bhattacharyya, *Journal of Magnetism and Magnetic Materials*, 342, 92 (2013).

[44] S. M. Abbas, R. Chatterjee, A. K. Dixit, A. V. Kumar, and T. C. Goel, *Applied Physics Letters* 101, 074105 (2007).

[45] L. Qin, H. Verweij, *Materials Letters*, 68, 143 (2012).

[46] F. Leccabue, R. Panizzieri, S. Garcia, N. Suarez, J. L. Sanchez, O. Ares, X. R. Hua, *Journal of Material Science*. 25, 2765 (1990).

[47] A. Ghasemi, *Journal of Magnetism and Magnetic Material*, 323, 3133 (2011).

[48] M. C. Dimri, S. C. Kashyap, D. C. Dube, *Ceramics International*, 30, 1623 (2004).

[49] A. Gonzalez-Angeles, G. Mendoza-Suárez, A. Grusková, I. Tóth, V. Jančárik, M. Papánová, J. I. Escalante-Garcı, *Journal of Magnetism and Magnetic Material*, 270, 77 (2004).

[50] W. Y. Zhao, P. Wei, H. B. Cheng, X. F. Tang, and Q. J. Zhang, *Journal of American Ceramic Society*, 90, 2095 (2007).

[51] M. J. Iqbal, M. N. Ashiq, *Chemical Engineering Journal*. 136, 383 (2008).

[52] I. Ali, M. U. Islam, M. S. Awan, M. Ahmad, M. A. Iqbal, *Journal of Superconductivity and Novel Magnetism*. 26, 3315 (2013).

[53] A. Thakur, R. R. Singh, P. B. Barman, *Journal of Magnetism and Magnetic Material*. 326, 35 (2013).

[54] S. Ilican, M. Caglar, Y. Caglar, *Material Science-Poland*, 25, 709 (2007).

[55] F. Song, X. Shen, J. Xiang, H. Song, *Materials Chemistry and Physics*, 120, 213 (2010).

[56] F. S. Tehrani, V. Daadmehr, A. T. Rezakhani, R. H. Akbarnejad, S. Gholipour, *Journal of Superconductivity and Novel Magnetism*, 25, 2443 (2012).

[57] X. Tang, B. Y. Zhao, K. A. Hu, *Journal of Material Science*, 41, 3867 (2006).

[58] J. P. Singh, G. Dixit, R. C. Srivastava, H. M. Agrawal, K. Asokan, *Journal of Physics D-Applied Physics*, 44, 435306 (2011).

[59] A. Poorbafrani, P. Kameli, H. Salamati: *Journal of Material Science*. 48,186 (2013).

[60] A. Singh, S. B. Narang, K. Singh, O. P. Pandey and R. K. Kotnala, *Journal of Ceramic Processing research*, 11, 241 (2010).

[61] I. Ali, M. U. Islam, M. S. Awan and M. Ahmad, *Journal of Electronics Material*, 43, 512 (2014).

[62] S. B. Narang and I. S. Hudiara, *Journal of Ceramic Processing Research*, 7, 113 (2006).

[63] I. Ali, M. U. Islam, M. S. Awan, and M. Ahmad, *Journal of Materials Engineering and Performance*, 22, 2104 (2013).

[64] M. Karmakar, B. Mondal, M. Pal, K. Mukherjee, *Sensors and Actuators B: Chemical*. 190, 627 (2014).

[65] S. Anjum, M. S. Rafique, M. Khaleeq-ur-Rahman, K. Siraj, A. Usman, S. I. Hussain, S. Naseem, *Journal of Magnetism and Magnetic Material*, 324, 711 (2012).

[66] M. Rawat, K.L. Yadav, *Journal of Alloys and Compounds*, 597, 188 (2014).

[67] A. A. Nourbakhsh et al. *Ceramics International*, 40, 5675 (2014).

[68] S. M. Masoudpanah, S. A. Seyyed Ebrahimi, C.K. Ong, *Journal of Magnetism and Magnetic Material*, 342, 134 (2013).

[69] H. Nishio, Y. Minachi and H. Yamamoto, *IEEE Transactions on Magnetics*.45, 5281 (2009).

[70] H. Nishio and H. Yamamoto, *IEEE Transactions on Magnetics*, 47, 3641 (2011).

[71] M. I. Oliva, P. G. Bercoff, H. R. Bertorello, *Journal of Magnetism and Magnetic Material*. 320, e100 (2008).

[72] F. Kools, A. Morel, R. Grossinger, J. M. Le Breton, P. Tenaud, , *Journal of Magnetism and Magnetic Material*, 242–245, 1270 (2002).

[73] L. Lechevallier, J. M. Le Breton, J. Teillet, A. Morel, F. Kools, P Tenaud, *Physica B* 327, 135 (2003).

[74] R.M. Atlas 1993, Handbook of Microbiological Media, Ed. by Parks L., CRC Press, Inc Taylor and Francis (2004).

[75] M.R. Meshram, Nawal K. Agrawal, B. Sinha, P.S. Misra, *Journal of Magnetism and Magnetic Materials*, 271, 207–214. (2004)

[76] M. J. Iqbal, S. Farooq, *Materials Research Bulletin* 46, 662–667. (2011)

[77] A. Haq, M. Anis-ur-Rehman, *Physica B* 407, 822–826. (2012)

[78] P.B. Braun *Philosophical Research Reports* 12:491 (1957)

[79] Ankush Thakur, P.B. Barman, R.R. Singh, Materials Chemistry and Physics, 156, 1-9 (2015).

[80] D.A. Vinnik, D.A. Zherebtsov, L.S. Mashkovtseva, S. Nemrava, A.S. Semisalova, D.M. Galimov, S.A. Gudkova, I.V. Chumanov, L.I. Isaenko, R. Niewa, *Journal of Alloys and Compounds*, 628, 480 (2015)

[81] Y. Tokunaga, Y. Kaneko, D. Okuyama, S. Ishitawa, T. Arima, S. Wakimoto, K. Kakurai, Y. Taguchi, and Y. Tokura, *Physical Review Letters*, 105, 257201 (2010).

[82] H.C. Fang, Z. Yang, C.K. Ong, Y. Li, C.S. Wang, Journal of Magnetism and Magnetic Materials, 187, 129 (1998).

[83] J. Qiu, Q. Zhang, M. Gu, and H. Shen, *Applied Physics Letters*, 98, 103905 (2005).

[84] S. Ounnunkad, S. Phanichphant, P. Winotai, and I. M. Tang, *Physica Status Solidi (b)*, 244, 2190. 2007

[85] E. D. Solovyova, E. V. Pashkova, V. P. Ivanitski, O. I. Vyunov, A.G. Belous, *Journal of Magnetism and Magnetic Materials*, 330, 72 (2013).

[86] S. Kanagesan, S. Jesurani, R. Velmurugan, S. Prabu, T. Kalaivani, *Materials Research Bulletin*, 47, 188 (2012).

[87] M. H. Kim, D. S. Jung, Y. C. Kang, J. H. Choi, *Ceramics International*, 35, 1933 (2009).

[88] J. M. Calderon Moreno, M. Yoshimura, *Solid State Ionics*, 154–155, 125 (2002).

[89] G. Xue, C. Gong, J. Liang, G. Liang, *Journal of Dispersion Science and Technology*, 30, 231 (2009).

[90] I. Horcas et al., *Review of Scientific Instruments*, 78, 013705 (2007).

[91] D. Bahadur, S. Rajakumar, and A. Kumar, *Journal of Chemical Sciences*, 118, 15 (2006,).

[92] T-H Ting, K-H Wu, *Journal of Magnetism and Magnetic Materials*, 322 2160–2166 (2010)

[93] B. Want, B. H. Bhat, B. Z. Ahmad, *Journal of Alloys and Compounds*, 627, 78 (2014).

[94] A. Srinivasa, T. Karthik, R. Gopalana, V. Chandrasekaran, *Materials Science and Engineering: B*, 172, 289 (2010).

[95] G. Tan, X. Chen, *Journal of Magnetism and Magnetic Material*, 327, 87 (2013).

[96] G. Tan and X. Chen, *Journal of Electronic Materials*, 42, 906 (2013).

[97] S. H. Mahmood, G. H. Dushaq, I. Bsoul, M. Awawdeh, H. K. Juwhari, B. I. Lahlouh, M. A. AlDamen, Z. Angew. *Journal of Mathematical Physics*, 2, 77. (2014)

[98] V. M. Gaikwad and S. A. Acharya, *RSC Advances*, 5, 14366 (2015)

[99] K. A. Mozul, L. P. Olkhovik, E. V. Shurinova, S. V. Blazhevich, T. G. Kuzmicheva, S. V. Chernikov, and A. S. Kamzin, *Physics of the Solid State*, 53, 2284 (2011)

[100] R. Schafer, P. C. Schmidt, *Methods in Physical Chemistry*, 2, 361 (2012)

[101] S. J. Iyengar, M. Joy, C. K. Ghosh, S. Dey, R. K. Kotnala and S. Ghosh, *RSC Advances*, 4, 64919 (2014)

[102] G. K. Thompson and B.J. Evans, *Journal of Magnetism and Magnetic Material*, 95, L142-L144 (1991)

[103] R. Sharma, R.C. Agarwala, Vijaya Agarwala, *Materials Letters*, 62, 2233 (2008)

[104] R. Sharma, R.C. Agarwala, V. Agarwala, *Journal of Alloys and Compounds* 467 357–365. (2009)

[105] A. Ghasemi, A. Hossienpourb, A. Morisakod, A. Saatchia, M. Salehia, *Journal of Magnetism and Magnetic Materials*, 302, 429 (2006).

[106] V. M. Petrov, V. V. Gagulin, *Inorganic Materials*, *37,* 93–98 (2001)

[107] M. S. Pinhoa, M. L. Gregoria, R. C. R. Nunes, B. G. Soares, *Polymer Degradation and Stability*, *73,* 1–5. (2001)

[108] E. F. Knott, Radar Cross Section Measurements: Springer US (2012).

[109] A. Carvalho, M. L. Gregori, B. Chambers; *Microwave and Optical Technology Letters*, *16,* 393–397. (1997)

[110] D.D.L. Chung, *Carbon*, *39*, 279–285. (2001)

[111] B. Zhang; Y. Feng,; J. Xiong,; Y. Yang,; Lu, H., *IEEE Transactions on Magnetics*, *42*, 1778–1781. (2006)

[112] H. M. Xiao; X. M Liua; S. Y. Fu, *Composite Science and Technology*. *66*, 2003–2008. (2006)

[113] A. Verma, A. K. Saxena, D. C. Dube, *Journal of Magnetism and Magnetic Material*, *263*, 228–234. (2003)

[114] C. H. Peng et al., *Journal of Magnetism and Magnetic Material*. *284,* 113–119. (2004)

[115] R. H. Kodama, *Journal of Magnetism and Magnetic Material*, *200,*359–372. (1999)

[116] X. Chen, G. Wang, Y. Duan, S. Liu, *Journal of Physics D-Applied Physics*., *40*, 1827–1830. (2007)

[117] V. G. Harris, *Journal of Magnetism and Magnetic Material*, *321*, 2035–2047. (2009)

[118] R. Khan, P. Khare, B.P. Baruah, A. K. Hazarika, N. C. Dey, *Advances in Chemical Engineering and Science*, *1*, 37-44. (2011)

[119] P. Saini, V. Chaudhary, S. K. Dhawan, *Indian Journal of Engineering and Materials Sciences*, *14*, 436-442. (2007)

[120] T. Mathavan, S. Umapathy, M. A. Jothirajan A. M. F. Benial, *Spectroscopy Letters*, *45*, 588–593 (2012)

[121] J. Huang, H. Zhuang, W. Li, *Material Research Bulletin*, *38*, 149–159. (2003)

[122] Kiani E.; Rozatian A. S. H.; Yousefi M. H.; J. Magn. Magn. Mater., *361*, 25–29 (2014).

[123] Meena, R. S.; Bhattachrya, S.; Chatterjee, R.; Mat. Sci. Eng. B-Solid, *171*,133–138 (2010)

[124] Goldman, A; Modern ferrite technology, Pittsburgh, USA, *second. ed.,* Springer**,** 39-42 (2006)**.**